INAUGURAL-DISSERTATION
zur
Erlangung der Doktorwürde
der
Naturwissenschaftlich-Mathematischen
Gesamtfakultät
der
Ruprecht-Karls-Universität
Heidelberg

vorgelegt von
Diplom-Physiker Florian Keil
aus Hamburg

Tag der mündlichen Prüfung: 16. Februar 2001

Dijet Production in Charged and Neutral Current e^+p Interactions at High Q^2 at HERA

Gutachter: Prof. Dr. Karlheinz Meier
Prof. Dr. Otto Nachtmann

Dissertation
submitted to the
Combined Faculties for the Natural Sciences and for Mathematics
of the Rupertus Carola University of
Heidelberg, Germany
for the degree of
Doctor of Natural Sciences

Dijet Production in Charged and Neutral Current e^+p Interactions at High Q^2 at HERA

presented by

Diplom-Physicist:	Florian Keil
born in:	Hamburg

Heidelberg, February 16, 2001

Referees:	Prof. Dr. Karlheinz Meier
	Prof. Dr. Otto Nachtmann

Abstract

Dijet production in charged and neutral current deep-inelastic positron-proton scattering at HERA is analysed in the kinematic range of boson virtualities Q^2 from 640 to 35 000 GeV^2. Dijet distributions of jet polar angle, jet transverse energy, invariant dijet mass and other dijet variables are presented and compared with QCD models and perturbative QCD calculations in next-to-leading order. Using parton densities derived from inclusive DIS cross section measurements, perturbative QCD is found to give a consistent description of both the charged and neutral current dijet distributions. Neutral current jet production at $Q^2 > 10\ 000$ GeV^2 is analysed in detail. No deviations from the standard model expectation are observed. A direct, model independent comparison of the charged and neutral current dijet distributions confirms the expectation that QCD processes proceed largely independently of the underlying electroweak interaction.

Kurzfassung

Die vorliegende Arbeit untersucht die Entstehung von 2-Jet-Strukturen in tiefunelastischen Streuereignissen des geladenen und neutralen Stromes bei HERA im kinematischen Bereich von Boson-Virtualitaten Q^2 zwischen 640 und 35 000 GeV^2. Die Verteilungen des Polarwinkels und der transversalen Energie der Jets sowie der invarianten 2-Jet-Masse und anderer 2-Jet-Variablen werden gemessen und mit den Vorhersagen von QCD-Modellen und störungstheoretischen QCD-Rechnungen in nächstführender Ordnung verglichen. Die Vorhersagen der störungstheoretischen QCD geben eine konsistente Beschreibung der 2-Jet-Verteilungen sowohl in Ereignissen des geladenen als auch des neutralen Stromes. Im Detail werden auch Jet-Verteilungen in Ereignissen des neutralen Stromes für Werte von $Q^2 > 10\ 000$ GeV^2 untersucht. Abweichungen von der Standard-Modell-Vorhersage werden nicht beobachtet. Ein direkter, modellunabhängiger Vergleich der 2-Jet-Verteilungen des geladenen und neutralen Stromes stützt die Erwartung, daß QCD-Prozesse weitgehend unabhängig vom zugrunde liegenden elektroschwachen Streuprozeß ablaufen.

Contents

Introduction

The study of jets of hadrons in deep-inelastic scattering (DIS) processes makes possible crucial tests of fundamental aspects of Quantum-Chromodynamics (QCD) - the theory of the strong interaction. Jets are considered to be the footprints of the final state quarks and gluons which are, owing to colour confinement, not directly measurable. In the Quark-Parton-Model DIS gives rise to events with one jet, originating from the hadronization of a quark struck out of the proton. Events with two or more jets are predicted by QCD via gluon radiation off quarks or the splitting of gluons into quark-antiquark pairs. Events with pronounced multi-jet structures were first observed with the advent of the electron-proton collider HERA [1]. At HERA proton and electron beams of 920 GeV and 27.6 GeV, respectively, provide a centre-of-mass energy of approximately 320 GeV. HERA thus extends the kinematic constraints of previous fixed-target experiments by several orders of magnitude in both the virtuality, Q^2, of the exchanged boson and the Bjørken scaling variable, x.

The total cross section at HERA is dominated by pure photon exchange via the neutral current (NC) process $ep \rightarrow eX$. At sufficiently high Q^2, however, the influences of Z^0 exchange, γ/Z^0 interference *and* $W^\pm$ exchange via the charged current (CC) process $ep \rightarrow \nu X$ contribute significantly. The inclusive NC and CC DIS cross sections have recently been measured and used to extract the proton structure functions for values of Q^2 up to 35 000 GeV^2 [2, 3]. Studies on the characteristics of the hadronic final state have so far concentrated mainly on NC interactions. In recent analyses the gluon density of the proton and the running strong coupling parameter α_s were determined from the measurement of multi-jet cross sections [4, 5]. Due to the strongly suppressed CC cross section, much less is yet known about the hadronic final state of CC events. At HERA 10 CC events with multi-jet structures were identified [6]. The shape of CC jets was studied in [7] on the basis of a very limited data sample, which is dominated by one-jet events. Due to the significantly lower centre-of-mass energies, pronounced multi-jet structures can not be observed in deep-inelastic neutrino-nucleon scattering. Here, only studies on e.g. hadron production mechanisms and charged hadron multiplicities have been performed [8].

In this thesis the results cited above are complemented by the first detailed investigation of multi-jet production in CC interactions. Emphasis is put on the analysis of dijet events. They are studied in terms of jet observables as a function of characteristic jet quantities like e.g. dijet mass, jet polar angle and jet transverse energy. The measured distributions are compared to QCD models and perturbative QCD calculations in next-to-leading order. Unlike in previous jet studies the present analysis is extended up to the highest Q^2 so far observed at HERA. Charged current *and* NC dijet production are explicitly studied for $Q^2 > 5\ 000\ \mathrm{GeV}^2$. In addition NC jet production is investigated for $Q^2 > 10\ 000\ \mathrm{GeV}^2$, exploiting the larger number of NC events available. Finally, dijet production in CC and NC events is compared directly with essentially no dependence on any model assumptions. This allows to study the expectation that QCD processes proceed largely independently from the underlying electroweak interaction. The main part of the results presented in this thesis is published in [9].

Remark: Throughout this thesis a system of units in which $h = c = 1$ is used.

Chapter 1

The H1 Experiment at HERA

1.1 HERA

The HERA[1] storage ring system at DESY[2] in Hamburg is the only facility worldwide for the simultaneous acceleration of electrons and protons. It consists of two independent storage rings of 6.3 km circumference. In the data taking period 1994 to 1997 HERA was operated with 27.6 GeV positrons and 820 GeV protons, resulting in a centre-of-mass energy of $\sqrt{s} \approx 300$ GeV. Since 1998 the proton energy has been increased to 920 GeV.

The particle beams consist of typically 180 colliding bunches with a longitudinal extension of approximately 1 cm for positrons and 20 cm for protons. Two consecutive bunches are separated by time intervals of 96 ns. In the 1997 HERA running period the average positron current was 36 mA, the average proton current 77 mA and the average luminosity 5×10^{30} cm^{-2}s^{-1}. The annual integrated luminosity increased from 4 pb^{-1} in 1994 to 35 pb^{-1} in 1997. In 2000 HERA delivered 67 pb^{-1} of data.

Four experiments are located around the HERA ring: In the northern and southern interaction zones the positron and proton beams collide inside the H1 and ZEUS detectors, respectively. To study the spin structure of the nucleons the HERMES experiment inserts polarized probes of ^{1}H, ^{2}H or ^{3}He into the longitudinally polarized positron beam. For the investigation of CP violation in the $B^0\bar{B}^0$-system the most recent experiment HERA-B introduces wire targets into the halo of the proton beam.

[1] Hadron-Elektron-Ring-Anlage
[2] Deutsches Elektronen-Synchrotron

1.2 The H1 Detector

The most striking features of the H1 detector [10] are its asymmetric geometry with a more massive instrumentation in the proton beam direction to account for the different beam energies and its almost full solid angle coverage. Figure 1.1 shows a longitudinal and a radial projection through its main components. These are the central tracking chambers, the electromagnetic calorimeter, the hadronic calorimeter, the SpaCal, the H1 solenoid with the instrumented iron return yoke and the forward muon system.

Also indicated is the H1 laboratory reference frame. Its positive z-axis is defined as the direction of the incoming proton beam. The x-axis points to the center of the HERA ring and the y-direction upwards. Its origin is placed in the nominal interaction point. In the following sections the components of the H1 detector most important for the present analysis are discussed in more detail.

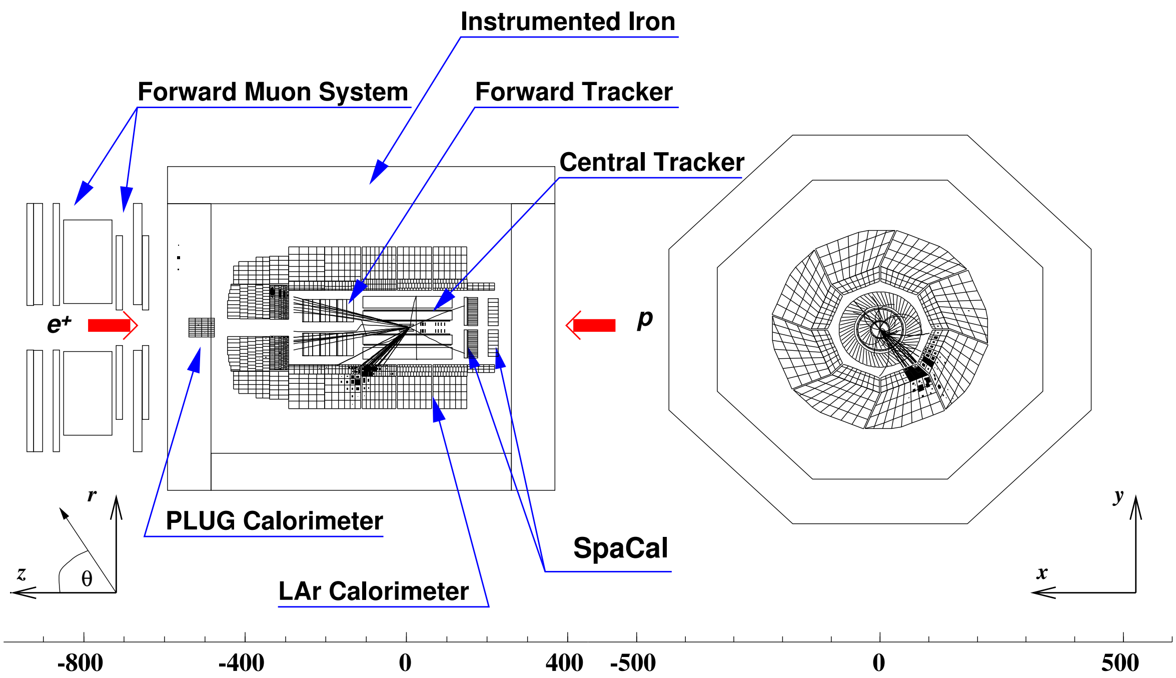

Figure 1.1: *A schematic of the H1 detector. The scale is given in centimeters. The lines and the filled rectangles are the traces of an ep-scattering event.*

1.2.1 Calorimeters

The **Liquid-Argon calorimeter** (LArC) covers the polar angle range $4° < \theta < 153°$. It is divided into an inner and outer part for the measurement of both electromagnetic and hadronic showers, respectively. The LArC is a sampling calorimeter with liquid argon as the active material. The passive material is lead in the electromagnetic and stainless steel in the hadronic part. In the z-direction it is composed of eight *wheels*, each of which is again subdivided into eight identical stacks or octants in the $r\phi$-plane (cf. figure 1.1). Except for the forward and backward wheels, each wheel consists of an electromagnetic and a hadronic section. The forward wheel has only a hadronic section, the backward wheel only an electromagnetic section. The LArC is highly segmented and consists of approximately 45 000 cells. The electromagnetic part has a finer granularity than the hadronic part to resolve the more compact structure of electromagnetic showers. Depending on the polar angle, the LArC has in total a depth of between 20–30 radiation lengths and between 4.5–8 hadronic interaction lengths.

The relative energy resolution of the LArC was determined in test beam measurements [11, 12] to be $12\%/\sqrt{E(\mathrm{GeV})} \oplus 1\%$ for electrons and $50\%/\sqrt{E(\mathrm{GeV})} \oplus 2\%$ for hadrons. The systematic uncertainty on the electromagnetic energy scale was determined in situ in [2, 13] to be in the range 0.7% – 3%, depending on the calorimeter wheel in which the energy was deposited. For the analysis of multi-jet hadronic final states the systematic uncertainty on the relative hadronic energy scale is 4% [14]. The LArC is non-compensating, i.e. an electron produces on average a larger signal than a hadron of the same energy. Offline software algorithms based on a cluster weighting technique have to be applied to correct for this effect. More detailed information on the LArC can be found in [15]. In the present analysis the LArC is used to measure the energy flow of the hadronic final state and to identify the scattered positron in deep-inelastic scattering events.

The **Spaghetti-Calorimeter** (SpaCal) enhances the detector acceptance in the backward region. Its main purpose is the identification of positrons at small scattering angles. The SpaCal covers the polar angle range ($153° < \theta < 177.8°$) and consists of a separate electromagnetic and a hadronic section. The SpaCal is a lead scintillating fibre calorimeter with in total 1348 photomultipliers amplifying the scintillator light. It has an energy resolution of $7.5\%/\sqrt{E(\mathrm{GeV})} \oplus 2\%$ for electrons and $30\%/\sqrt{E(\mathrm{GeV})} \oplus 2\%$ for hadrons [16, 17]. In the present thesis it is only used to measure hadronic energy flow not contained in the LArC.

The **Instrumented Iron** return yoke of the H1 solenoid is equipped with streamer tubes for the identification of minimal ionizing particles and to catch hadronic showers leaking out of the LArC. In this analysis it is mainly used for the identification of background events from cosmic muons or beam halo muons.

1.2.2 Tracking System

Tracks of charged particles are reconstructed with a system of drift and proportional chambers. The momentum and the charge is determined from the curvature of the tracks in the magnetic field of 1.2 T of the H1 solenoid. The solenoid surrounds the LArC.

The **Central Tracking Device** (CTD) consists of two concentric drift chambers with their signal wires stretched parallel to the beam pipe (CJC1, CJC2) and two drift chambers with their signal wires stretched perpendicular (CIZ,COZ) to it. The CTD covers the polar angle range $25° < \theta < 155°$. The xy-resolution of the CTD is 170 μm and the z-resolution 300 μm. The relative momentum resolution σ_p/p^2 is better than 0.01 GeV^{-1}. The CTD is complemented by the two multi-wire proportional chambers (MWPC) CIP and COP. Due to much shorter drift ways of MWPC's they provide accurate timing information and are thus used to deliver fast trigger signals.

In the forward region tracks are reconstructed with the **Forward Tracking Device** (FTD). It is composed of three identical *supermodules*. Each supermodule is made up of a planar drift chamber, a MWPC, a transition radiator and a radial drift chamber. The FTD extends the angular coverage of the tracking system down to 7°. The xy-resolution of the FTD is 210 μm and the polar angle resolution is better than 1 mrad.

In this analysis the CTD is used to determine the event vertex, the scattering angle of the scattered positron and the momenta of charged particles from the hadronic final state. Tracks reconstructed in the FTD are only used to determine the event vertex in the case where no tracks are measured in the CTD.

1.3 H1 Trigger System and Event Reconstruction

The main sources of background in the H1 detector are interactions of the proton beam with remnant gas atoms in the beam pipe or the wall of the beam pipe and synchrotron radiation from the positron beam. The background rate is of order 10 kHz. Since the rate of interesting physics events is typically as few Hz an effective filtering scheme is needed. In H1 this is achieved by four successive trigger levels L1, L2, L4 and L5[3].

The first trigger level L1 provides within 2.4 μs on average a decision of whether an event is to be rejected or kept and passed on to the next trigger level. As input L1 uses information from all available subdetectors, given in the form of *trigger elements*. The trigger elements are logically combined into 128 different subtriggers, which are optimized for the identification of different physics processes. Subtriggers with high rates are artificially suppressed ('prescaled') in order to reduce the fraction of less interesting physics events. To avoid deadtime all signals from the approximately 25 bunch crossings occurring within the 2.4 μs needed by L1 are pipelined. The pipeline is only stopped and the event passed on to the next trigger level if at least one subtrigger condition is fulfilled. At this moment the detector readout is stopped and the deadtime begins.

On the second trigger level L2 more sophisticated filtering mechanisms based on topological requirements and neural network outputs are applied within 20 μs. If an event is rejected by L2 the deadtime ends and the data taking starts anew. If L2 delivers the signal to keep the event, then the full detector information is read out in approximately 1 ms during which time the detector is not ready for data taking.

[3]The trigger level L3 is currently not used.

Finally, the events accepted by L2 are transferred with a rate of 40 Hz online to the trigger level L4. Here the full event record is available and the events are partially reconstructed. Software algorithms based on characteristic details of the physics processes of interest are applied to the reconstructed events for further filtering. The events accepted by L4 are written to tape with a rate of 10–20 Hz. A small fraction of events rejected by L4 are stored to monitor the L4 efficiency.

The full event reconstruction including the application of calibration factors and the distribution of the events among different physics classes is performed on the last trigger level L5. If an event cannot be assigned to a certain class it is rejected. Finally the events are written in compressed format to so called *data summary tapes* which are the basis for all physics analyses. In 1998 L4 took over the event classification leaving L5 as a pure event reconstruction unit.

Chapter 2

Perturbative QCD and DIS

In this chapter the basic theoretical and phenomenological concepts related to the present analysis are briefly reviewed. Fundamental principles of Quantum Chromodynamics (QCD) needed to define and calculate cross sections in perturbation theory are summarized in the first section. The concept of parton density functions and the factorization of perturbative and non-perturbative effects is introduced thereafter. The phenomenology of deep-inelastic *ep*-scattering is introduced in the third section. In the fourth section the structure of di-parton cross sections is addressed. Finally, the definition of meaningful jet observables and the calculation of jet cross sections in perturbative QCD (pQCD) are discussed.

2.1 Perturbative QCD

One of the most striking features of QCD, the theory of the strong interaction between quarks and gluons, is asymptotic freedom. Asymptotic freedom explains why perturbative methods can be applied to calculate cross sections at high energies. It introduces the concept of a running coupling parameter α_s which becomes smaller as the energy scale of the process increases. The key to this phenomenon is the fact that gluons as well as quarks carry colour charge and thus are subject to self-interaction. Besides the quark-gluon interaction two more fundamental interactions thus exist in QCD: the three gluon and the four gluon interactions.

The radiative corrections to these three fundamental vertices thus contain not only quark loops but also gluon loops, which have to be considered in the perturbative expansion of any physical observable S. The simplest loop diagrams are shown in figure 2.1. The loops correspond to the creation of virtual particles with infinite momenta. The dedicated integrals given by the Feynman rules are divergent. The presence of these *ultraviolet* divergences require *renormalization* of the perturbation series. The integrals are made finite by introducing a dimensionful parameter μ_R, corresponding to the momentum at which the subtractions to remove the ultraviolet divergences are performed. The divergences are absorbed into a redefined coupling parameter

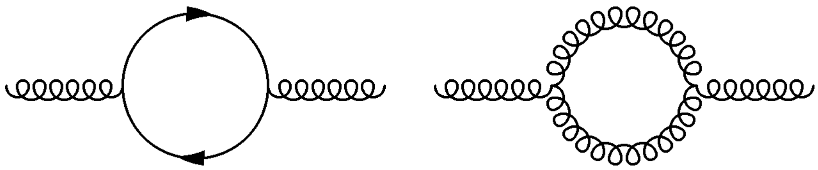

Figure 2.1: *Feynman diagrams related to the running of α_s in the one loop approximation. Quarks are represented by solid lines, gluons by curly lines.*

$\alpha_s(\mu_R)$ according to a specific but in principle arbitrary prescription, referred to as a *renormalization scheme*. The scale μ_R is however not intrinsic to the theory, i.e. it does not appear in the QCD Lagrangian. Therefore the physical observable S must depend neither on μ_R nor on the chosen renormalization scheme. Mathematically this is expressed in the *renormalization group equation* [18]:

$$\mu_R^2 \frac{dS}{d\mu_R^2} \stackrel{!}{=} 0 \tag{2.1}$$

It can be shown that the μ_R dependence in S enters entirely through the scale dependence of α_s [19]. The latter is expressed by the β-function of QCD which describes how α_S changes in the transition from μ_R to any larger energy scale Q:

$$\frac{\partial \alpha_s(Q^2)}{\partial t} = \beta(\alpha_s(Q^2)), \quad t = \ln \frac{Q^2}{\mu_R^2}. \tag{2.2}$$

The β-function has the perturbative expansion

$$\beta(\alpha_s) = -\beta_0 \alpha_s^2 (1 + \beta_1 \alpha_s + \beta_2 \alpha_s^2 + \mathcal{O}(\alpha_s^3)). \tag{2.3}$$

The coefficients β_0 and β_1 are universal, whereas the higher order coefficients depend on the renormalization scheme chosen. They are extracted from the higher order loop corrections to the fundamental vertices of the theory. The coefficient β_0 receives contributions from the diagrams shown in figure 2.1. It is given by

$$\beta_0 = \frac{33 - 2n_f}{12\pi}, \tag{2.4}$$

where n_f is the number of quark flavours to be considered at a given energy scale. If both $\alpha_s(\mu_R^2)$ and $\alpha_s(Q^2)$ are in the perturbative region ($\alpha_s \ll 1$), β_1 and the higher order coefficients can be neglected to first approximation. Equation 2.2 can then be integrated to give

$$\alpha_s(Q^2) = \frac{\alpha_s(\mu_R^2)}{\alpha_s(\mu_R^2) + \beta_0 \ln \frac{Q^2}{\mu_R^2}}. \tag{2.5}$$

It follows that for very large Q^2 the *running coupling* approaches zero. The theory is said to be *asymptotically free.*

Perturbative QCD predicts the energy dependence of the strong coupling but not its absolute value. The latter has to be determined from experiment. Conventionally all determinations of α_s are interpreted in terms of a common reference scale, taken to be the mass of the Z^0 boson. The current world average value is $\alpha_s(M_Z^2) = 0.119 \pm 0.002$ [20]. Note that α_s at higher orders does not only depend on the renormalization scale but also on the renormalization scheme used. The most common scheme is the $\overline{\mathrm{MS}}$ modified minimal subtraction scheme [21]. Here, the ultraviolet divergences are regularized by reducing the four-dimensional integrals to those of dimension $4 - 2\epsilon$, where ϵ is a small number.

The perturbative expansion of the physical observable S, e.g. a cross section for a given scattering process, can now be written as

$$S = S_0 + S_1\alpha_s(\mu_R^2) + S_2\alpha_s^2(\mu_R^2) + \cdots . \tag{2.6}$$

The coefficients S_i generally depend on μ_R. The required independence of S from the renormalization scale is only guaranteed when calculated to all orders in α_s. Then the μ_R dependences of the coefficients S_i and α_s completely cancel. In any *fixed order* perturbative calculation S will always depend on the renormalization scale. The size of this scale dependence is related to the size of the (omitted) higher order corrections. In leading order (LO), i.e. the first order in α_s contributing to a given process, the coefficient is independent of μ_R. Thus at LO the μ_R dependence of S is only due to $\alpha_s(\mu_R^2)$ and no cancellation takes place. Only when calculated at next-to-leading order (NLO) can the scale dependence of S be reduced due to cancellations between the coefficients and α_s.

2.2 Parton Densities and Factorization

Perturbative calculations are possible in the region of high energies or, equivalently, short distances, i.e. for $\alpha_s \ll 1$. The perturbative calculation of cross sections is, however, complicated in the presence of an initial state hadron, such as the proton in deep-inelastic scattering. The interactions between quarks and gluons inside a hadron take place at low energies and are thus not calculable by perturbative means. Therefore the concept of *parton density functions* has been introduced. They describe the momentum distribution of the individual quarks and the gluon inside hadrons. More precisely, the function $q_{p,h}(\xi)$ defines the probability to find a parton p (quark or gluon) inside the hadron h with the fraction ξ of the hadron's momentum. The parton density functions are not predicted by QCD but must be determined from experiment. Most importantly, they can be defined completely process independently, i.e. they specify a universal property of the given hadron.

The scattering of a virtual boson off a quark receives $\mathcal{O}(\alpha_s)$ corrections from *initial* state gluon emissions. The perturbative calculation of these corrections are subject to collinear divergences, i.e. for gluons emitted with vanishing transverse momentum. These divergences are not cured by renormalization. They can, however, be factorized into redefined parton density functions in a similar way as the ultraviolet divergences are absorbed into the renormalized strong coupling. This requires the introduction of a *factorization scheme* and a *factorization scale* μ_F. The latter can be interpreted as the transverse momentum below which gluon emissions are absorbed into the redefined parton densities. The μ_F dependence of the parton density functions is described by the DGLAP equations [22]. In analogy to the renormalization group equation (2.1) they express the requirement, that any physical observable must not depend on the choice made for μ_F.

The factorization of the non-perturbative and the perturbative parts of the strong interaction is proven to hold to all orders in perturbation theory. Simplifying, the general structure of a cross section involving partons in the initial state may be expressed as [23]

$$\sigma_h = \sum_p \int d\xi \; q_{p,h}(\xi, \mu_F^2) \cdot \hat{\sigma}_p(\xi, \mu_F^2), \tag{2.7}$$

where the sum runs over all contributing partons p, and $\hat{\sigma}_p$ denotes the perturbatively calculable partonic cross section from which the initial state singularities are factorized out at the scale μ_F.

2.3 Deep-Inelastic Scattering

Two processes contribute to deep-inelastic positron-proton scattering (DIS): the neutral current (NC) process $e^+p \to e^+X$, where the interaction between the positron and the proton is mediated by a photon or a Z^0 boson, and the charged current (CC) process $e^+p \to \bar{\nu}_e X$, where a charged W^+ boson is exchanged. Both processes are directly observable at HERA. In the Quark-Parton-Model (QPM) DIS is described as the elastic interaction of a virtual boson with a free, point-like constituent of the proton, known as a *parton*. The partons are assumed to carry no transverse momentum. The cross section is then given as the incoherent sum over all contributing partons. Identifying the partons with the three valence quarks the QPM corresponds to the zeroth order approximation of QCD. DIS in the QPM is illustrated by the diagram in figure 2.2.

Labelling the four-momenta of the incoming and outgoing lepton as k and k', the momentum of the incoming proton as P and the momentum transfer carried by the exchanged boson as $q = k - k'$, the standard DIS variables are defined by

$$Q^2 \equiv -q^2, \qquad x \equiv \frac{Q^2}{2qP}, \qquad y \equiv \frac{qP}{kP}. \tag{2.8}$$

The Bjoerken scaling variable x is interpreted in the QPM as the fraction of the proton's momentum carried by the struck quark. The inelasticity y corresponds to the relative energy transfer from the positron to the proton in the proton rest frame. The DIS variables (2.8) are related to the centre-of-mass energy squared $s \approx 4E_eE_p$ by

$$Q^2 = xys. \tag{2.9}$$

Given the energies E_e and E_p of the incoming positron and proton the kinematics of DIS events are thus completely determined by the knowledge of two independent variables.

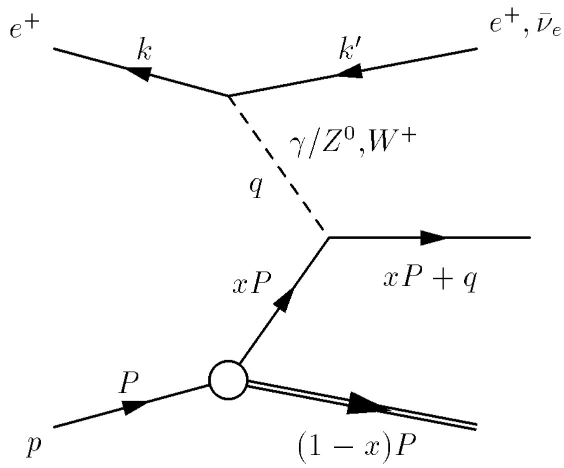

Figure 2.2: *Deep-inelastic scattering in the Quark-Parton-Model.*

The general structure of a DIS cross section is the product of a propagator term and a structure functions term, the latter parameterizing the structure of the proton. For NC $e^+p \rightarrow e^+X$ scattering the Born double differential cross section can be expressed as

$$\frac{d^2\sigma_{NC}^{e^+p}}{dxdQ^2} = \frac{2\pi\alpha^2}{xQ^4}\phi_{NC}^{e^+p}(x,Q^2) \tag{2.10}$$

where α is the fine structure constant and

$$\phi_{NC}^{e^+p}(x,Q^2) = Y_+\tilde{F}_2(x,Q^2) - Y_- x\tilde{F}_3(x,Q^2) - y^2\tilde{F}_L(x,Q^2). \tag{2.11}$$

The functions $Y_\pm \equiv 1 \pm (1-y^2)$ represent the helicity dependences of the electroweak interaction. The longitudinal structure function $\tilde{F}_L$ influences the cross section significantly only at large values of y. For unpolarized particles the generalized structure function $\tilde{F}_2$ can be decomposed into the structure functions F_2, F_2^Z and $F_2^{\gamma Z}$, representing the contribution of pure photon exchange, pure Z^0 exchange and γZ^0 interference, respectively. In a similar way $x\tilde{F}_3$ is composed of the parity violating structure function xF_3^Z and $xF_3^{\gamma Z}$.

By neglecting the $\tilde{F}_L$ contribution and the vector coupling of the positron to the Z^0 boson relative to its axial vector coupling, the NC cross section equation 2.10 can be approximated as[1]:

$$\frac{d^2\sigma_{NC}^{e^+p}}{dxdQ^2} \approx \frac{2\pi\alpha^2}{x}\left[\frac{1}{Q^4}Y_+F_2 + \frac{1}{4}\frac{\kappa_w^2}{(Q^2+M_Z^2)^2}Y_+F_2^Z - \frac{1}{2}\frac{\kappa_W}{Q^2(Q^2+M_Z^2)}xF_3^{\gamma Z}\right], \tag{2.12}$$

where M_Z is the mass of the Z^0 boson and $\kappa_W = 1/(4\sin^2\theta_W\cos^2\theta_W)$ a function of the weak mixing angle θ_W. From the above expression it can be seen that for $Q^2 \ll M_Z^2$ the NC cross section is dominated by pure photon exchange. The Z^0 effects only become

[1]The vector coupling of the positron to the Z^0 boson is $v_e = \frac{1}{2} - 2\sin\theta_W \approx 0.04$, where θ_W is the weak mixing angle. The axial vector coupling $a_e = \frac{1}{2}$.

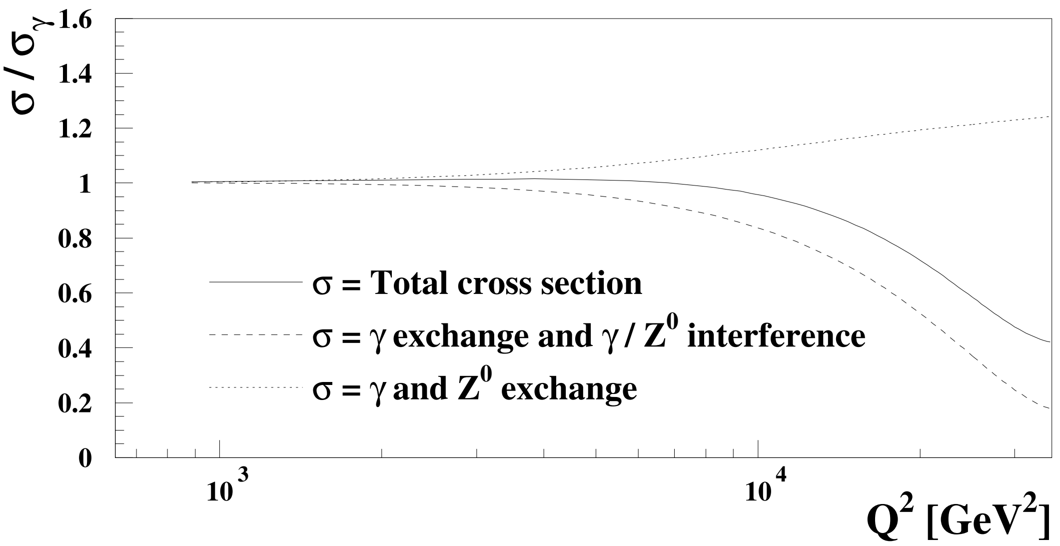

Figure 2.3: *Effect of Z^0 exchange and γZ^0 interference on the total NC e^+p cross section. The cross section for pure photon exchange is denoted σ_γ. The calculations are performed with the HECTOR program [24] at fixed x of 0.4.*

sizable at $Q^2 \approx M_Z^2$. For e^+p scattering γZ^0 interference leads to an effective reduction of the cross section, as illustrated in figure 2.3. For $Q^2 < 5\,000$ GeV^2 the effects of Z^0 exchange and γZ^0 interference largely cancel. At $Q^2 = 10\,000$ GeV^2 Z^0 exchange increases the cross section by ≈10%, while γZ^0 interference reduces it by ≈15%. The net effect is a reduction of 5%. At $Q^2 = 20\,000$ GeV^2 the contributions from Z^0 exchange and γ/Z^0 interference reduce the cross section by ≈30%.

The Born double differential cross section for the CC $e^+p \to \bar{\nu}_e X$ process can be expressed as:

$$\frac{d^2\sigma_{CC}^{e^+p}}{dx dQ^2} = \frac{G_F^2}{2\pi x}\left(\frac{M_W^2}{M_W^2 + Q^2}\right)^2 \phi_{CC}^{e^+p}(x, Q^2) \tag{2.13}$$

where M_W is the mass of the W^+ boson and G_F is the Fermi coupling constant. The structure function term ϕ_{CC} can be decomposed into generalized structure functions in a similar way to ϕ_{NC} in equation 2.11 (see e.g. [25]).

The different Q^2 dependences of the NC and CC cross sections are best seen using the relation $G_F = \pi\alpha/(\sqrt{2}M_W^2 \sin^2\theta_W)$. For $Q^2 \ll M_W^2$ and $\phi_{NC} \approx \phi_{CC}$ the CC cross section is much smaller than the NC cross section. Only at $Q^2 \approx M_W^2$ do they start to be of similar size. This is illustrated in figure 2.4 with a recent H1 measurement of the NC and CC e^+p cross sections, here shown as a function of Q^2 and integrated over x. At low Q^2 the CC cross section is much less steeply falling than the NC cross section. For $Q^2 \approx 500$ GeV^2 the cross sections differ by two orders of magnitude. When Q^2 approaches M_W^2 the cross sections start to agree in shape and magnitude. Note also that at this scale the effects of Z^0 exchange and γ/Z^0 interference start to become sizable. However, for e^+p scattering the CC cross section is always smaller than the NC cross section even at highest Q^2. This is due to the different boson-quark couplings in CC and NC interactions.

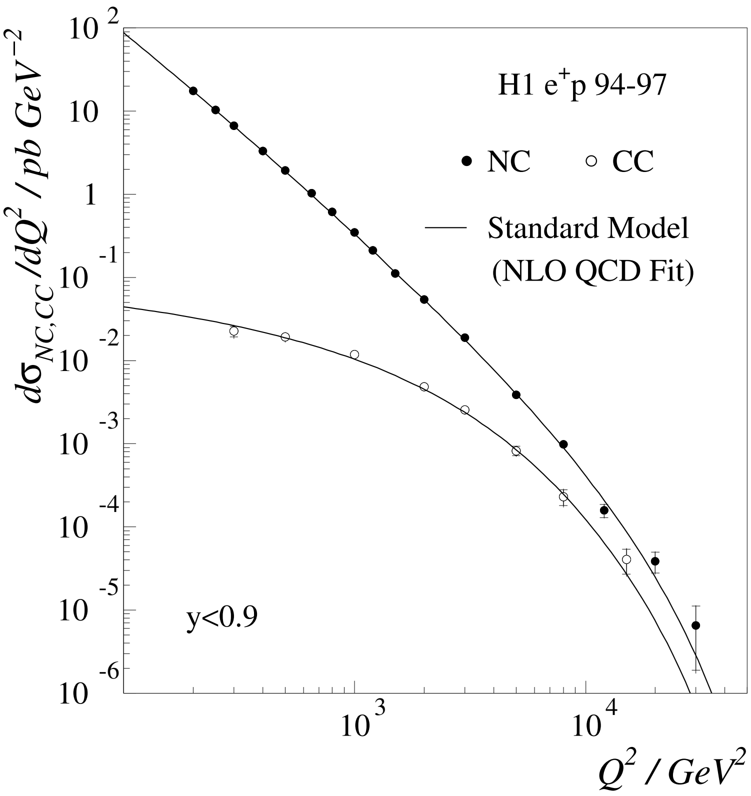

Figure 2.4: *H1 measurement of the differential NC and CC cross sections $d\sigma/dQ^2$ [2].*

This is illustrated within the simple picture of the QPM. Here, i.e. in leading order QCD, when neglecting Z^0 exchange, the NC structure function term (2.11) is given as:

$$\phi_{NC}^{e^+p} = [1 + (1-y)^2]x\left[\frac{4}{9}(u + c + \bar{u} + \bar{c}) + \frac{1}{9}(d + s + \bar{d} + \bar{s})\right], \qquad (2.14)$$

where the up, down, charm and strange quark densities are denoted u, d, c and s, respectively. Note that in the kinematic range of HERA the bottom and top quark densities do not contribute. The corresponding $\mathcal{O}(\alpha_s^0)$ approximation for the CC structure function term ϕ_{CC} can be expressed as

$$\phi_{CC}^{e^+p} = x[(\bar{u} + \bar{c}) + (1-y)^2(d+s)]. \qquad (2.15)$$

In this approximation the NC cross section at high x depends predominantly on the valence distribution of the u quark, whereas the CC cross section is mainly sensitive to the d valence quark density.

2.4 Cross Sections for Di-parton Final States

In the QPM the parton densities and thus the structure functions do not depend on Q^2. When taking higher order QCD processes into account this simple picture is distorted. In $\mathcal{O}(\alpha_s)$ the structure functions receive contributions from two fundamental processes

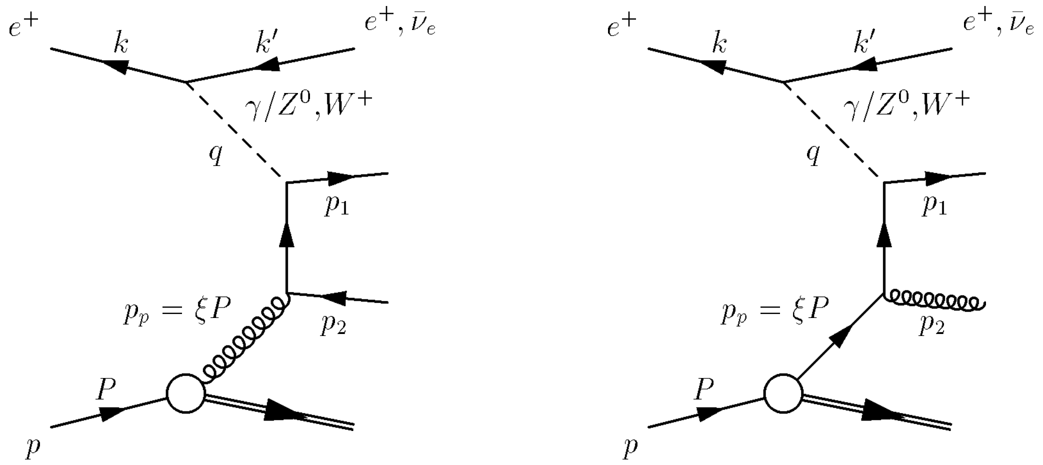

Figure 2.5: *Selected Feynman diagrams contributing to di-parton production: Boson-Gluon-Fusion (left) and QCD-Compton scattering (right).*

that each lead to two-parton final states: the Boson-Gluon-Fusion (BGF) $V^\star g \to q\bar{q}$ and the QCD-Compton $V^\star q \to gq$ scattering process ($V^\star$ denotes the virtual exchanged γ/Z^0 or W^+ boson). Selected Feynman diagrams for these processes are shown in figure 2.5.

The cross sections for these *di-parton* final states are fully described by five independent kinematic variables. Besides x and Q^2 the azimuthal angle Φ between the parton plane $(\vec{p}_p, \vec{p}_1)$ and the lepton plane $(\vec{k}, \vec{k}')$ in the hadronic centre-of-mass frame and the Lorentz invariant variables

$$x_p = \frac{Q^2}{2p_p q} = \frac{Q^2}{Q^2 + m_{12}^2} \quad \text{and} \quad z_i = \frac{p_p p_i}{p_p q}, \quad i = 1, 2, \tag{2.16}$$

are frequently used. The four momenta are labeled according to figure 2.5 and $m_{12}^2 = (p_1 + p_2)^2$ is the invariant mass squared of the di-parton system. The z_i are related by $z_1 + z_2 = 1$ for massless partons. The fivefold differential $\mathcal{O}(\alpha_s)$ cross sections for NC and CC interactions can be written as

$$\begin{aligned} \frac{2\pi x_p d^5\sigma_{NC}}{dx dQ^2 dx_p dz_1 d\Phi} &= \frac{2\pi\alpha^2}{Q^4}\frac{\alpha_s}{2\pi}[I_g^{NC} + I_q^{NC}], \\ \frac{2\pi x_p d^5\sigma_{CC}}{dx dQ^2 dx_p dz_1 d\Phi} &= \frac{G_F^2}{2\pi}\left(\frac{M_W^2}{M_W^2 + Q^2}\right)^2 \frac{\alpha_s}{2\pi}[I_g^{CC} + I_q^{CC}], \end{aligned} \tag{2.17}$$

where I_g and I_q denote the contributions of the BGF and QCD-Compton processes, respectively [26]. The NC and CC I_g and I_q terms differ with respect to the different couplings and helicity structures in NC and CC interactions.

The perturbative calculation of the cross sections is subject to singularities in certain regions of the di-parton phase space. This is best seen when expressing the cross sections in terms of the variables x_p and z_1. For the QCD-Compton contribution the cross section has the singularity structure:

$$d\sigma_{QCDC} \sim \frac{1 + x_p^2 z_1^2}{(1 - z_1)(1 - x_p)}. \tag{2.18}$$

The cross section diverges for $z_1, x_p \to 1$. This corresponds to the kinematic configurations where p_2 is collinear to p_p or p_1, or p_2 is soft, i.e. its energy approaches zero. The soft singularities are also called *infrared* singularities.

The singularity structure of the BGF contribution is given as:

$$d\sigma_{BGF} \sim \frac{[z_1^2 + (1 - z_1)^2][x_p^2 + (1 - x_p)^2]}{z_1(1 - z_1)}. \tag{2.19}$$

In addition to the singularity as $z_1 \to 1$, $d\sigma_{BGF}$ is singular for $z_1 \to 0$. This occurs if p_1 is collinear to p_p or if p_1 is soft.

The collinear and infrared singularities associated with the initial state can be absorbed into the redefined parton densities as discussed in section 2.2. The final state singularities cancel against corresponding singular terms in the $\mathcal{O}(\alpha_s)$ virtual di-parton corrections according to the Kinoshita-Lee-Nauenberg mechanism [27].

2.5 Jet Cross Sections in Perturbative QCD

Due to the phenomenon of hadronization the two partons originating from the processes discussed in the previous section will give rise to two jets of hadrons in the detector. The ability to clearly distinguish the two jets mainly depends on the separation of the primary partons, the nature of the hadronization process and the detector resolution. This makes necessary the introduction of a well-defined jet observable in order to define a genuine *dijet* cross section both on the parton and the (experimental) hadron level.

A jet observable generally is required to establish a close correspondence between the partonic and hadronic final states and to be only weakly affected by the long-distance hadronization processes. In order to be calculable order-by-order in perturbation theory a jet observable in addition has to fulfill the conditions of infrared and collinear safety. An observable $\mathcal{F}_{jet}$ meets this requirement if its value is independent of the number of soft and collinear particles in the final state. More precisely, $\mathcal{F}_{jet}$ should behave as $\mathcal{F}_{jet}^{m+1} \to \mathcal{F}_{jet}^{m}$ whenever the $(m+1)$-parton configuration is obtained from the m-parton configuration by adding a soft parton or replacing a parton by a pair of collinear partons with the same total momentum.

The property of infrared and collinear safety guarantees the cancellation of soft and collinear singularities from the real corrections against those of the virtual corrections to the equivalent process, as mentioned in the previous section. For practical applications in NLO calculations the cancellation of singularities has to be arranged in an observable independent way. Technically this is achieved by two different methods: the subtraction method [28] and the phase-space-slicing method [29]. The approach common to both methods is to first extract the singular parts of the cross section and treat them analytically. The remaining finite parts are then integrated numerically.

Subtraction method The separation of the cross section integral into a finite and a singular part is achieved by subtracting and adding back a quantity σ_{CT} which fulfills two conditions: it has the same point-wise singular behaviour as the real corrections and it is analytically integrable over the one-parton phase space giving rise to the collinear and soft divergences. When subtracted from the real corrections σ_{CT} acts as a counter term such that the integral can be solved numerically. The analytic integration of σ_{CT} yields poles which can be combined with those of the virtual corrections to cancel all divergences. The remaining integral can again be evaluated numerically.

Phase-space-slicing method The range of integration of the real corrections is split by introducing a small technical cut-off parameter s_{min}. The lower integral can be evaluated analytically using soft and collinear approximations of the integrand which regulate the singularity. The resulting singular expressions cancel against corresponding singular terms from the virtual corrections. The remaining (upper) integrals are finite and can be evaluated numerically. The method is exact in the limit where s_{min} vanishes. In practice s_{min} only has to be sufficiently small such that the soft and collinear approximations are valid.

Both methods are implemented in current programs which make possible the NLO calculation of arbitrary infrared and collinear safe observables in deep-inelastic scattering. These programs are introduced in the next chapter.

Chapter 3

QCD: Models and Calculations

In this chapter two different approaches to describe deep-inelastic ep scattering data are introduced. QCD Monte-Carlo event generators are discussed in the first section. They simulate DIS events based on model assumptions and parameter sets which have to be adjusted in comparison with experimental data. Programs for the perturbative calculation of cross sections in fixed order of the strong coupling are described afterwards. They are theoretically well-defined and almost entirely free of external parameters.

3.1 QCD Monte-Carlo Models

Monte-Carlo (MC) event generators are based on models for the simulation of higher order QCD processes and theoretically not described effects of hadronization. A comparison of MC predictions with measured data thus provides important information on the validity of the model assumptions. Providing the full record of all particles produced in a generated event MC models are in addition used to estimate: 1) the size of effects related to the limited acceptance and resolution of the detector, when combined with detector simulation programs and, 2), the size of hadronization effects needed for the comparison of perturbative QCD calculations with experimental data.

In this analysis the MC models ARIADNE 4.10 [30], LEPTO 6.5.2β [31], RAPGAP 2.08/06 [32] and HERWIG 5.9 [33] are used. The parameter sets of ARIADNE, LEPTO and HERWIG have been optimized in [34] to describe NC DIS data. In all MC simulations the CTEQ4L [35] parameterizations of the proton parton densities are taken.

ARIADNE simulates higher order QCD effects according to the color dipole model [36]. Gluons are generated by a chain of independently radiating color dipoles. The primary dipole is formed between the proton remnant and the struck quark. In order to include gluon-induced processes, exact $\mathcal{O}(\alpha_s)$ matrix elements are implemented. In a BGF process the starting point for further gluon radiation are two independent dipoles formed between the quark or the antiquark and the proton remnant. QCD-Compton processes originating from the matrix elements are discarded assuming that the first hard gluon emission is correctly reproduced by the QCD cascade. ARIADNE is interfaced with the LEPTO program which generates the electroweak part of the ep scattering process.

The fragmentation of the partons into the final state hadrons is performed with the Lund string model [37]. In this approach the color flux between a $q\bar{q}$ pair is represented by a narrow flux tube, a 'string', of constant energy density. The potential energy of the string increases when the particles are rapidly separating due to the rise of the strong force with increasing distance. When the energy is high enough a $q\bar{q}$ pair can tunnel out of the vacuum thereby breaking the string into smaller substrings, still rapidly separating. The final state hadrons are formed when no energy is left to produce further $q\bar{q}$ pairs.

LEPTO Higher order QCD processes are approximated by initial and final state parton showers [38] governed by the DGLAP evolution equations. The starting point for the initial state parton shower is a quark with a small spacelike virtuality. This quark becomes increasingly off-shell by emitting further partons until it is scattered by the virtual boson and turned into a quark that is either on-shell or has a timelike virtuality. According to its virtuality it can then radiate further partons to form the final state parton shower.

Hard processes are described by $\mathcal{O}(\alpha_s)$ matrix elements. The soft and collinear divergences of the matrix elements are avoided by restrictions on z_i. The first hard emission from the matrix elements and the parton showers are matched by restricting the maximum virtuality of the parton shower to the invariant mass $\hat{s}_{min}$ of the di-parton system. In practice the amount of parton radiation is steered by a parameter Q_0 which has a value in the order of the mass of a typical hadron ($\approx$1 GeV). Hadronization is performed according to the Lund string model.

RAPGAP is very similar to LEPTO for DIS processes. It is also based on the DGLAP parton showers and $\mathcal{O}(\alpha_s)$ matrix elements. In contrast to LEPTO it uses the transverse momentum of the di-parton system as a cut-off for the matrix elements. In addition, RAPGAP contains various models for diffractive processes and is able to generate events with a resolved virtual photon. RAPGAP also uses the Lund string model.

HERWIG is also based on initial and final state parton showers and $\mathcal{O}(\alpha_s)$ matrix elements. In contrast to LEPTO the HERWIG parton showers fully include QCD color coherence effects and azimuthal correlations from gluon polarization. Hadronization is performed according to a cluster fragmentation approach [39]. Here gluons are forced to split non-perturbatively into $q\bar{q}$ pairs after the parton shower evolution has terminated. Based on the concept of preconfinement [40], adjacent quarks and antiquarks are combined to form color singlet clusters. The final state hadrons arise non-perturbatively out of the decay of these clusters. The cluster fragmentation approach has the advantage of introducing only very few parameters for the modeling of the hadronization process compared to the Lund string model.

QED radiative corrections can have a large impact on inclusive cross section measurements and hadronic final state analyses. They are simulated in ARIADNE, LEPTO and RAPGAP by the DJANGO [41] interface to the HERACLES program [42]. HERACLES allows the integration of the inclusive differential NC and CC cross section including QED radiative processes. For NC interactions leptonic initial and final state bremsstrahlung processes as well as quarkonic radiation are implemented. For CC reactions only the contribution from initial state leptonic bremsstrahlung is included.

Throughout this thesis the MC simulation after the parton cascade and after hadronization is referred to as the *parton* and the *hadron level*, respectively. When combined with the H1 detector simulation, the MC output is referred to as the *detector level*.

3.2 Next-to-Leading Order QCD Programs

In contrast to MC models purely perturbative QCD calculations in DIS are essentially parameter-free. In principle the only input is a value for the strong coupling α_s, a choice for the renormalization and factorization scale and a set of proton parton density functions. Comparisons with measurements are thus a crucial test of QCD at short distances. Calculations of cross sections in NLO are necessary to reduce the renormalization (and factorization) scale dependence significantly compared with LO predictions (cf. section 2.1). NLO calculations are expected to provide reliable predictions in the presence of high energy scales. In regions where soft and collinear effects become important next-to-next-to-leading order or even higher order calculations may be required. At present, however, no such calculations for DIS are available.

Four NLO programs are currently available for the calculation of cross sections and distributions of arbitrary infrared and collinear safe observables: MEPJET [23], DISENT [43], JETVIP [44] and DISASTER++ [45]. All programs are able to calculate the total ep-cross section and the dijet cross section in perturbative QCD in NLO. They all provide the full partonic event record needed in order to apply arbitrary cuts on the final state.

MEPJET employs the phase-space-slicing method to organize the cancelation of final state soft and collinear divergences. It is at present the *only* program that includes besides γ exchange, Z^0 effects and W exchange. MEPJET is thus used in this thesis to analyze the CC dijet data. The renormalization and factorization scale can be chosen arbitrarily in MEPJET.

DISENT is based on the subtraction method with the subtraction terms constructed by means of dipole factorization [43]. Whereas any desired renormalization scale can be chosen in DISENT, the factorization scale is fixed to (multiples) of Q.

Among the four programs DISENT is by far the fastest with respect to computing time. In the present thesis it is used to calculate the NC NLO predictions.

JETVIP uses the phase-space-slicing method. It is the only program that includes photoproduction and contributions from resolved virtual photons in addition to DIS processes. In the present thesis JETVIP is only used as a cross-check to the DISENT predictions.

DISASTER++ The cancellation of singularities is achieved by the subtraction method in combination with a generalized partial fraction formula [45]. In contrast to the other programs DISASTER++ makes the full dependence on the number of quark flavours together with an arbitrary choice of the factorization scale explicitly available.

The consistency of the predictions of the four programs has been studied in [46]. For the LO NC jet cross sections all four programs are tested to agree better than a fraction of a per cent. Overall agreement is observed between the NLO jet cross section calculations of DISENT and DISASTER++. The only difference between DISENT and DISASTER++ recorded so far is observed for extreme values of a specific event shape variable [47]. These extreme phase space regions are however not relevant for the present analysis.

Neutral current NLO jet cross sections calculated with MEPJET are observed to be systematically lower than the DISENT and DISASTER++ predictions. Effects in the order 5–8% are seen [46]. The results are found to be independent of the choice for the value of the phase-space-slicing parameter. The reason for these discrepancies is not yet known. Likewise the reason for an observed unexpected strong dependence of the JETVIP calculations on the value of the phase-space-slicing parameter is so far unclear. However, for values between 10^{-3} and 10^{-4} the JETVIP results are in general agreement with DISENT and DISASTER++.

In [46] it is thus recommended to use DISENT or DISASTER++ for the calculation of NC jet cross sections. Due to the lack of alternatives, however, MEPJET is the only choice for CC calculations. Note that the observed discrepancies between MEPJET and the other programs do not necessarily affect the CC calculations.

Chapter 4

Data Selection

This analysis is based on the data taken with the H1 detector in 1994–1997. They correspond to an integrated luminosity of 35.7 pb^{-1}. The main selection criterion of CC events is the observation of a large imbalance in transverse momentum caused by the scattered neutrino which cannot be detected directly. Neutral current events are selected by requiring the identification of the scattered positron. For a direct comparison the CC and the NC data samples are defined analogously. The missing transverse momentum in CC events and the transverse momentum of the scattered positron in NC events must exceed 25 GeV. This leads to roughly 500 CC and 8 600 NC events. The corresponding Q^2 of the selected events is larger than 640 GeV^2.

The CC event selection used in this thesis is based on [48, 49]. The method used therein for the reconstruction of the missing transverse momentum as well as the techniques used for the rejection of background have been adopted. The NC event selection is essentially identical to that used for the H1 measurement of inclusive cross sections in [2]. This concerns primarily the positron energy calibration and the hadronic energy measurement. Details of both event selections can also be found in [13]. After short notes on kinematic reconstruction methods and the hadronic energy measurement, the main aspects of the CC and NC event selections will be described.

4.1 Kinematic Reconstruction

The *hadron method* reconstructs the kinematic variables entirely from the energies and momenta of the hadronic final state particles. It is the only kinematic reconstruction method that is available for CC events. The kinematic variables are given by [50]

$$y_h \equiv \frac{\sum_i (E_i - p_{z,i})}{2E_e}, \qquad Q_h^2 \equiv \frac{P_{T,h}^2}{1-y_h}, \qquad x_h \equiv \frac{Q_h^2}{s y_h}, \tag{4.1}$$

where the transverse momentum $P_{T,h}$ of the hadronic final state is defined as

$$P_{T,h} = \sqrt{(\sum_i p_{x,i})^2 + (\sum_i p_{y,i})^2}. \tag{4.2}$$

The sums in equations 4.1 and 4.2 run over all final state particles i with three momentum components $p_{x,i}, p_{y,i}, p_{z,i}$ and energy E_i, excluding the scattered lepton. Particle masses are neglected. The centre-of-mass energy squared and the energy of the incoming positron are denoted by s and E_e, respectively. The hadron method relies on the assumption that the amount of longitudinal momentum in the positron direction and the transverse momentum lost in the beam pipe are negligible.[1]

The Q^2 resolution of the hadron method degrades strongly with increasing y_h as

$$\frac{\delta Q_h^2 \mid_{y_h}}{Q_h^2} = \frac{\delta y_h}{1-y_h}, \qquad \frac{\delta Q_h^2 \mid_{P_{T,h}}}{Q_h^2} \sim \frac{\delta P_{T,h}}{P_{T,h}}. \tag{4.3}$$

For the kinematic selection of this analysis the Q^2 resolution decreases from $\approx$20% at low y_h to $\approx$30% at high y_h. The y resolution of the hadron method is in contrast essentially independent of y_h.

In NC events the kinematic variables can be reconstructed by various means since the detected scattered positron provides redundant information. In the present analysis the electron method is generally used. Given the energy E'_e and the polar angle θ_e of the scattered positron, the kinematic variables are defined by

$$y_e \equiv 1 - \frac{E'_e}{E_e}(1-\cos\theta_e), \qquad Q_e^2 \equiv 4E_eE'_e\cos^2\frac{\theta_e}{2}, \qquad x_e \equiv \frac{Q_e^2}{sy_e}. \tag{4.4}$$

The electron method provides the best Q^2 resolution over the entire phase space. However, the y resolution degrades severely with decreasing y according to

$$\frac{\delta y_e \mid_{E'_e}}{y_e} = \frac{y_e - 1}{y_e}\frac{\delta E'_e}{E'_e}, \qquad \frac{\delta y_e \mid_{\theta_e}}{y_e} = \frac{1-y_e}{y_e}\cot\left(\frac{\theta_e}{2}\right)\delta\theta_e. \tag{4.5}$$

In figure 4.1 the y resolution of the electron and the hadron method are compared for NC events generated with ARIADNE and passed through the H1 detector simulation. At low y the hadron method provides a much better y resolution (20%) than the electron method (40%). At high y the situation is the opposite. While the y resolution remains essentially unchanged for the hadron method, it drastically improves for the electron method (5%).

4.2 Hadronic Energy Measurement

The measurement of the hadronic energy flow is largely based on the LArC. However, for low momentum particles the energy resolution of the central tracking chambers is superior to that of the LArC. Therefore the hadronic energy measurement can be significantly improved by combining the calorimetric energy measurement with the

[1]Note that particles escaping through the beam pipe in proton direction (i.e. $\theta \approx 0°$) do not contribute to $\sum_i(E_i - p_{z,i})$.

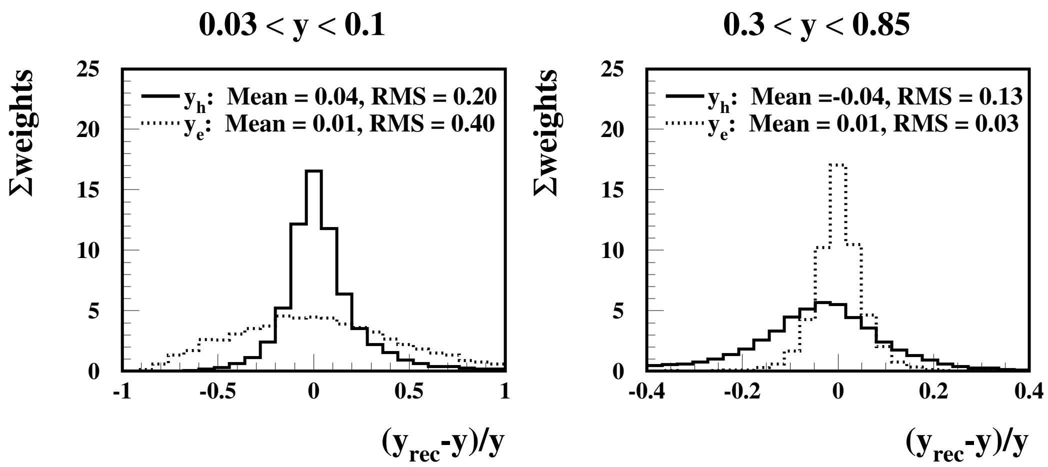

Figure 4.1: *Resolution of y_e and y_h for NC events generated with ARIADNE including the H1 detector simulation.*

momenta of low momentum tracks ($P_T < 2$ GeV) [2]. The method used for this purpose was developed in [51]. The calorimetric energy measured in the electromagnetic (hadronic) LArC in a cylinder of 15 (25) cm radius around a given track is compared to the track momentum. If the calorimetric energy is lower than the track momentum then the calorimetric energy is discarded and the track momentum is used. Otherwise, the calorimetric energy is taken and the track momentum is ignored henceforth. Double counting of energy is thus avoided. The hadronic energy measurement is further improved by including hadronic energy depositions measured in the SpaCal calorimeter.

4.3 Selection of Charged Current Events

- $\mathbf{P_{T,h} > 25}$ **GeV**

The main selection criterion for CC events is the observation of a large missing transverse momentum P_T^{miss}, assigned to the scattered neutrino escaping undetected. In this analysis P_T^{miss} is required to exceed 25 GeV. For CC events P_T^{miss} is identical to $P_{T,h}$ as defined in equation 4.2. $P_{T,h}$ is reconstructed from energy depositions in the LArC and the instrumented iron.

The CC cross section is a steeply falling function of $P_{T,h}$. Therefore, the requirement $P_{T,h} > 25$ GeV a priori strongly limits the available statistics. The reason for this tight requirement is the background from photoproduction and NC events which is predominant at low $P_{T,h}$. In [2] it is shown that an efficient rejection of this background at $P_{T,h} > 12$ GeV requires restrictions on the values of variables which utilize topological properties of the hadronic final state. This method may, however, produce a bias on the jet structure of the selected events and was thus not adopted in the present analysis.

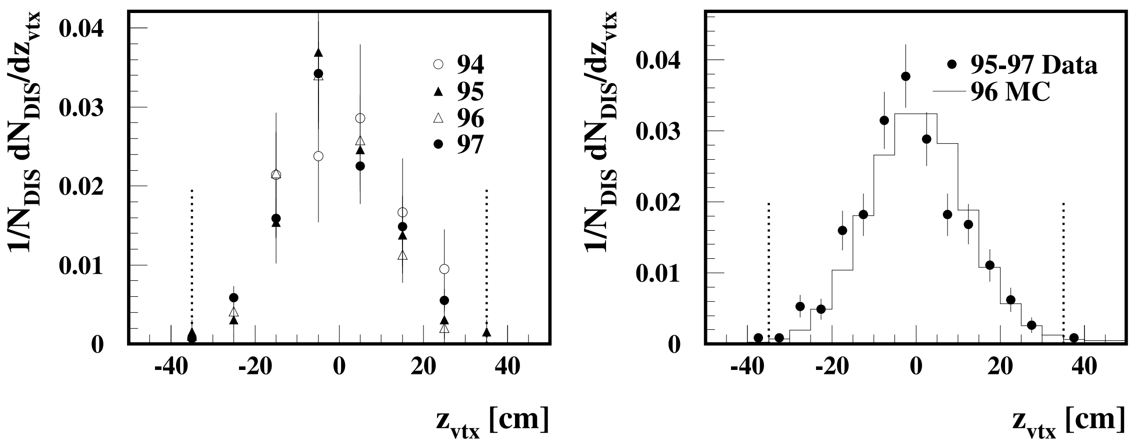

Figure 4.2: *Distribution of z_{vtx} for CC events with $P_{T,h} > 25$ GeV. The ARIADNE prediction includes the 1996 detector simulation. The dotted lines indicate the cuts applied in this analysis.*

- $\mid \mathbf{z_{vtx}} \mid$ **< 35 cm**

The z-coordinate z_{vtx} of the reconstructed primary vertex of the selected events is required to be within ±35 cm of its nominal position. This strongly reduces background from beam wall and beam gas interactions. Figure 4.2 shows the z_{vtx} distributions for the different years and the combined 1995–1997 data together with the MC prediction. The z_{vtx} distribution of 1994 data is shifted in positive z direction with respect to the other years. The 1994 data are reweighted to correct this effect. The MC prediction is shifted by ≈ 1.5 cm in positive z direction with respect to the 1995–1997 data. The MC events are reweighted to fit the data distributions.

- $\mathbf{0.03 < y_h < 0.85}$

The inelasticity y_h must fulfill $0.03 < y_h < 0.85$. The lower limit avoids the region where the CC trigger efficiency is small and steeply falling [13]. The upper limit excludes the high y region where the Q^2 resolution strongly decreases.

- **Background rejection**

There are two main sources of ep-induced background: NC events and photoproduction events in which the scattered positron escapes through the beam pipe. In both cases a poorly reconstructed hadronic final state or unidentified particles may lead to a sizable total transverse momentum. Most of this background is effectively reduced by the strong $P_{T,h}$ requirement [13].

Neutral current events are further suppressed by rejecting events where a positron has been identified (see also next section). In addition, events are discarded, when no positron was found but there was an isolated high momentum track pointing to a crack between the octants of a wheel (ϕ-crack) or two adjacent wheels (z-crack) of the LArC. It is also ensured that no event of the NC selection is contained in the CC selection. The remaining NC background is estimated with ARIADNE to be less than 1%.

The photoproduction background is evaluated with the MC generator PYTHIA [52] and tagged data events. It is less than 2%. Other sources of ep-background, e.g. semileptonic decays of real W bosons, are negligible [13].

Events from cosmic ray muons or proton beam halo muons may also pass the CC selection criteria. They can partially be reduced by using the timing information from the time-of-flight system. Events where a cosmic or beam halo muon overlaps with a photoproduction event are suppressed by topological requirements [53]. Finally the remaining CC candidates are scanned visually and events clearly identified as background are rejected.

- **Final data sample**

The final data sample contains 460 CC events. The kinematic selection implies a minimum Q^2 of 640 GeV^2. The average Q^2 of the events is 2 200 GeV^2, the average $x \approx 0.1$.

- **Trigger efficiency**

The subtriggers ST66 and ST77 are used to trigger CC events. The subtriggers are based on the LAr-E_T-miss trigger element which indicates are large total transverse energy in the LArC. The LAr-E_T-miss trigger element is used with a high threshold of 7.5 GeV in ST66. In ST77 it is used with a threshold of 6 GeV. Both subtriggers use timing information from the tracking chambers. The subtrigger ST66 in addition uses the timing information provided by the LArC. The inclusion of timing information in the subtriggers reduces background from non-ep interactions. Charged current events must fulfill either the ST66 or the ST77 trigger conditions.

For the determination of the efficiency of the subtriggers ST66 and ST77 the CC statistics is not sufficient. Therefore the *pseudo CC* technique is used which exploits the high NC statistics available [54]. After the NC events have been identified all information related to the scattered positron is removed from the subdetectors. The pseudo CC events are then reweighted to the CC cross section such that the CC x and Q^2 spectra are correctly reproduced. The technical aspects of the reweighting procedure are explained in detail in section 7.4.

The trigger efficiency as a function of $P_{T,h}$ and y_h is shown in figure 4.3. On average the CC trigger efficiency is 94%. The inefficiency of $\approx$ 15% at low $P_{T,h}$ is mainly visible at low and high y_h. At low y_h the hadronic final state is scattered forward. The inefficiency occurs primarily because the most forward part of the LArC is not included in the calculation of the LAr-E_T-miss trigger element.[2] At high y_h the hadronic final state is largely measured with the central part of the LArC. Here the electronic noise level and thus the energy thresholds for individual cells are relatively high. The trigger efficiency is reasonably well described by the MC prediction.

[2]The reason for this is that the forward part of the LArC is most sensitive to background from beam gas and beam wall interactions.

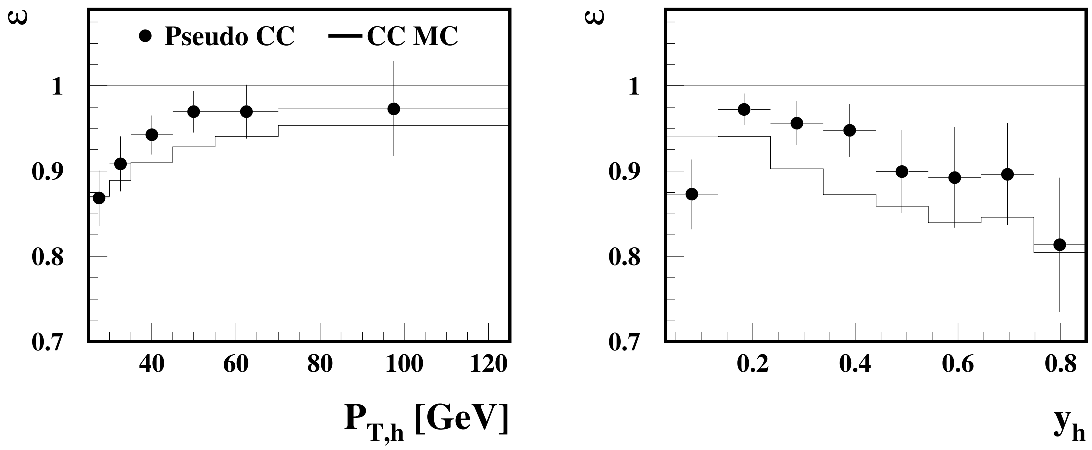

Figure 4.3: *Trigger efficiency for events with $P_{T,h} > 25$ GeV determined from the 1994–1997 pseudo CC data. The ARIADNE prediction is combined with the 1996 H1 detector simulation.*

In this thesis dijet event rates are measured, i.e. the dijet cross section as function of characteristic jet variables normalized to the total DIS cross section. Therefore, the actual value of the trigger efficiency, which is high, is of less importance than a possible dependence of the trigger efficiency on the event topology. This will be studied in section 6.2.

4.4 Selection of Neutral Current Events

- **Positron Identification**

The NC event selection requires the identification of the scattered positron in the LArC. The energy cluster with the highest transverse momentum in the electromagnetic section of the LArC is taken as the positron candidate. The cluster is then investigated in terms of spatial isolation and compactness. A reconstructed track pointing towards the positron cluster is required if the polar angle of the positron candidate lies within the acceptance of the central tracking chambers. The perpendicular distance from the associated track to the centre of gravity of the positron cluster is required to be less than 12 cm. The energy of the cluster and the polar angle of the track are taken as energy E'_e and polar angle θ_e of the scattered positron. If no track is assigned the angle is determined from the cluster position. Detailed information on the H1 electron finding algorithm can be found in [55].

- **$\mathbf{P_{T,e} > 25}$ GeV**

In analogy to the CC selection the transverse momentum of the scattered positron $P_{T,e}$ is required to exceed 25 GeV. It is reconstructed from the scattered positron's energy and polar angle according to $P_{T,e} = E'_e \sin\theta_e$. Events are discarded where the positron is scattered in a region of $\pm 2°$ around one of the eight ϕ-cracks or ± 5 cm around the z-crack at $z = 20$ cm between the CB2 and CB3 wheels of the LArC. This reduces the necessary corrections for energy lost in passive detector material and thus improves the positron energy measurement.

- $\mathbf{\mid z_{vtx} \mid < 35}$ **cm**

The z position of the reconstructed event vertex has to be within the same range as for the CC events. Its distribution is shown in figure 4.4. The shift of $\approx$4 cm of the 1994 data relative to the other years is now clearly visible. As for the CC events the MC prediction is shifted by $\approx$1.5 cm compared to the data. The 1994 data and the MC events are reweighted accordingly. The weights are determined from Gaussian fits to the respective distributions. The NC weights are also used to reweight the 1994 CC data.

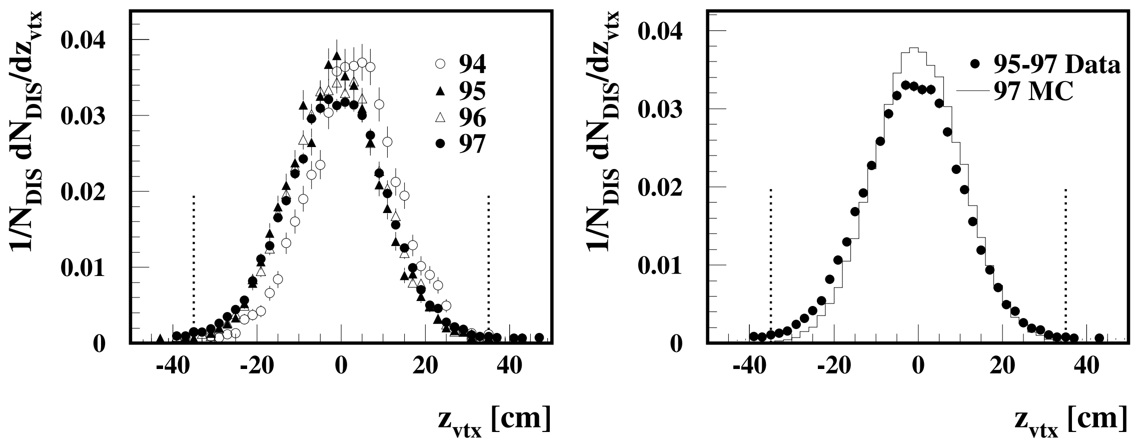

Figure 4.4: *Distribution of z_{vtx} for NC events with $P_{T,e} > 25$ GeV. The ARIADNE MC prediction includes the 1997 detector simulation. The dotted lines indicate the cuts applied in this analysis.*

- $\mathbf{y_h > 0.03}$, $\mathbf{y_e < 0.85}$

The constraint on y for NC events is based on y_h for $y > 0.03$ and on y_e for $y < 0.85$. This ensures the best y resolution over the entire phase space (cf. figure 4.1).

- **Background rejection**

The major contribution to the ep-induced background to NC events comes from photoproduction events where a hadron is misidentified as the scattered positron. It is partially reduced by the cluster-track-link requirement introduced above. The energy spectrum of these fake positrons is steeply falling leading to rather large values of y_e. The requirement $y_e < 0.85$ therefore reduces the number of misidentified energy clusters. In a perfectly reconstructed event

$$E - P_z \equiv \sum_i (E_i - p_{z,i}) = 2E_e = 55 \text{ GeV}, \tag{4.6}$$

due to energy and momentum conservation. Here, E_i and $p_{z,i}$ denote the energy and longitudinal momentum components of all detector objects i. Photoproduction events where the scattered positron is lost in the beam pipe (i.e. $\theta_e \approx 180°$) tend to have smaller values of $E - P_z$. In order to further reduce the photoproduction background $E - P_z$ is required to exceed 35 GeV. The size of the remaining photoproduction background is estimated with the MC model PYTHIA to be less than one per cent.

- **Trigger efficiency**

The trigger efficiency for NC events is determined in [13] to be nearly 100% for the entire phase space covered in this analysis. The trigger efficiency for dijet events is again briefly discussed in section 6.2.

- **Final data sample**

The final NC data sample contains 8 623 events. The average Q^2 of the selected events is 1 500 GeV^2, the average $x \approx 0.12$.

CC and NC kinematic distributions

The distributions of the CC and NC kinematic variables P_T, Q^2, x and y are shown in figure 4.5. The P_T spectra are steeply falling over four orders of magnitude. The differences between the CC and the NC distributions are mainly due to the different couplings and propagators of the bosons in CC and NC interactions (see also sections 2.3 and 7.4).[3] The data are well described by the ARIADNE prediction combined with the H1 detector simulation.

[3]Note that the distributions are normalized to the respective total number N_{DIS} of selected DIS events.

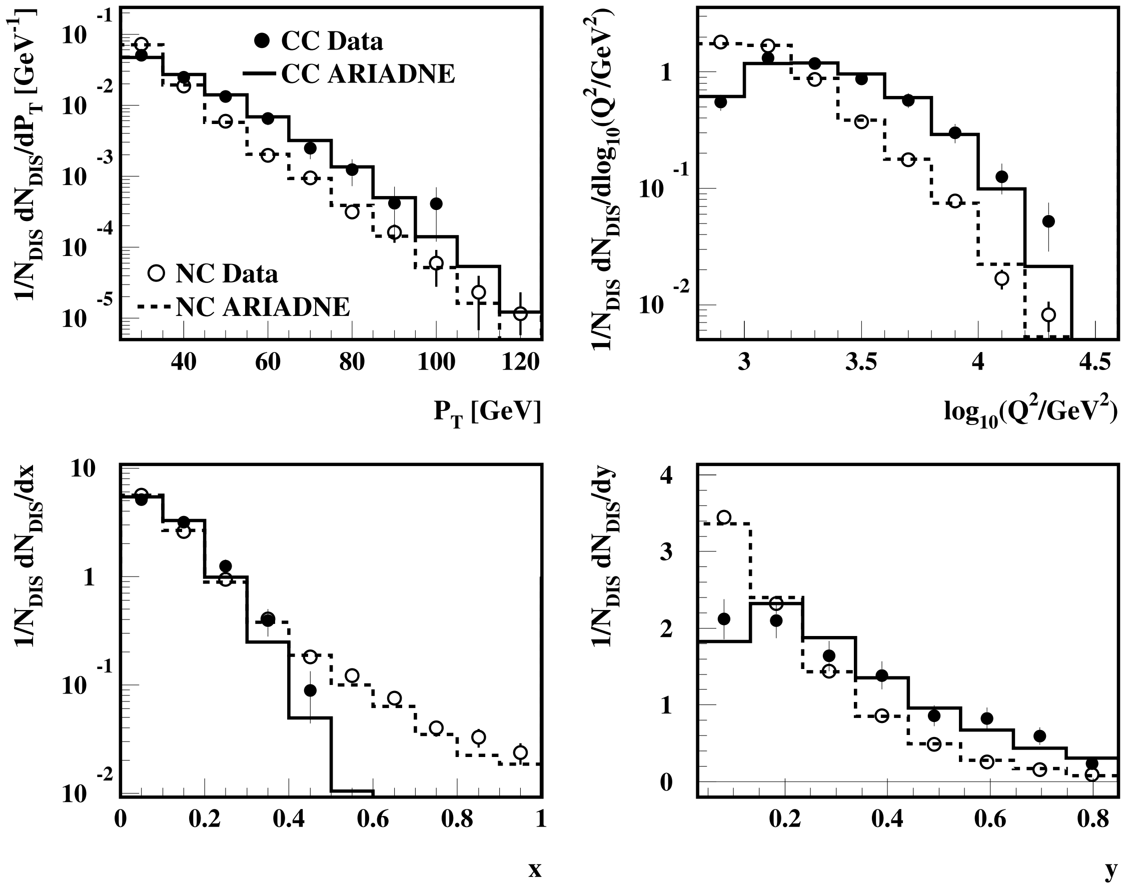

Figure 4.5: *Uncorrected data distributions for the selected CC and NC events. The kinematic variables are reconstructed from the hadronic final state and the scattered positron for the CC and the NC events, respectively. The errors are statistical only. Also shown are the CC (full line) and NC (dashed line) predictions of ARIADNE including the H1 detector simulation and QED radiative processes.*

Chapter 5

Jet Definition

Jets of hadrons provide one of the most suggestive indications for the presence of quarks and gluons in high energy particle collisions. *Pronounced* jet structures are, however, not the general case in deep-inelastic scattering. Generally, there is no way to assign a given hadron uniquely to a certain jet. This lead to the development of algorithms which define the jets and their properties from a specific configuration of final state particles. In DIS several *jet algorithms* are currently used. They can be characterized by a few common features: an iterative clustering procedure in which the *distance measure* and the *recombination scheme* determine whether and how a pair of unresolved particles is combined into a single pseudo-particle or jet; a *stopping condition* which determines when the clustering is ended and the remaining objects are treated as the final jets; a special *treatment of the proton remnant* which is necessary to account for the color flow between the proton fragments and the quarks and gluons from the hard scattering; the *reference frame* in which the algorithm is applied.

5.1 Jet Algorithm

The present analysis is based on a modified version of the Durham jet algorithm. The Durham algorithm was originally introduced in e^+e^- annihilation experiments [56]. The algorithm is applied in the laboratory frame. For its application in DIS it is modified by defining a *pseudo-particle* accounting for the large longitudinal momentum carried away through the beam pipe by the proton remnant. Its four-vector is defined as

$$P_{pp} = (p^{miss}, 0, 0, p^{miss}) \tag{5.1}$$

with

$$p^{miss} = E_p - E_e - (p_z^{lep} + \sum_i p_{z,i}) \tag{5.2}$$

where E_p denotes the energy of the incoming proton, E_e the energy of the incoming positron, p_z^{lep} the z-momentum component of the scattered lepton and $p_{z,i}$ the z-momentum component of any detector object excluding the scattered positron in NC events. For CC events the scattered neutrino is first reconstructed from the hadronic final state exploiting energy and momentum conservation.

For the experimental data the 'objects' entering the jet algorithm are the combinations of tracks and calorimetric energy depositions as explained in chapter 4.2 plus the pseudo-particle defined in equation 5.1. The scattered positron in NC events is removed. The polar angle of each object is required to exceed 7°. This avoids the region close to the edge of the LArC, thereby significantly improving the experimental resolution of jet variables [57].

Now, the algorithm calculates for each initial pair of objects (i, j) the quantity

$$k_{T,ij}^2 = 2\min[E_i^2, E_j^2](1 - \cos\theta_{ij}). \tag{5.3}$$

Here, E_i and E_j denote the energy of the objects i and j, and θ_{ij} denotes the angle between them[1]. The pair of objects (i, j) with the minimum $k_{T,ij}^2$ is combined to a 'proto jet' by adding their four momenta p_i and p_j. In this analysis the procedure is iterated until all objects and proto jets are combined to give *exactly* (2+1) jets (the '+1' is referring to the proton remnant jet). Thus at this stage *every* event is formally treated as a dijet event. Events with pronounced dijet structures are then selected by imposing a lower limit on y_2 defined as[2]

$$y_2 \equiv \min_{i,j}(k_{T,ij}^2)/W^2, \quad i, j \in \{1, 2, 2+1\}, \quad i \neq j. \tag{5.4}$$

Here, W corresponds to the invariant mass of the hadronic final state, calculated from all objects entering the jet algorithm. The choice of W as a reference scale reduces the experimental error because effects of the hadronic energy scale uncertainty largely cancel in the definition of y_2.

The algorithm is applied equally to the MC events after detector simulation. In MC events simulated at the hadron and parton level and in perturbative QCD calculations, the input objects are the hadron and parton four-momenta, respectively. The polar angle cut of 7°, introduced above for detector objects, is also applied to hadrons and partons. Objects with polar angle below 7° are added to the proton remnant.

The application of the jet algorithm in the laboratory frame avoids the additional experimental uncertainty induced by a Lorentz transformation into another reference frame. This is in particular relevant for the CC analysis given the poor Q^2 resolution of ≈30%.

[1] The (modified) Durham algorithm arose from the well-known JADE algorithm [58] by replacing E_iE_j with $\min[E_i^2, E_j^2]$ in the definition of $k_{T,ij}^2$ (equation 5.3). This avoids erroneous combinations of low-energetic objects separated by large angles θ_{ij}.

[2] Alternatively the jet algorithm can run with a fixed jet resolution parameter y_{cut}. In this case the clustering procedure ends, when the $k_{T,ij}^2/W^2$ of any pair of objects or proto jets is larger than y_{cut}.

5.2 Jet Variables

In addition to y_2 the distributions of the following dijet variables are studied:

- The invariant mass m_{12} of the two non-remnant jets. Jets are not necessarily massless. This is taken into account in the reconstruction of m_{12}.
- The variable x_p defined as
$$x_p \equiv \frac{Q^2}{Q^2 + m_{12}^2}. \tag{5.5}$$
In leading order QCD x_p is related to the scaling variable x and the fraction ξ of the protons momentum carried by the parton entering the hard scattering process by $x_p = x/\xi$. Equation 5.5 corresponds to the definition of x_p in equation 2.16 with the invariant mass of the di-parton system replaced by the invariant dijet mass. The value of x_p approaches one in the limit were the non-remnant jets are combined to form one jet, i.e. $m_{12} \approx 0$.
- The variable z_p is defined as
$$z_p \equiv \frac{\min_{i=1,2}[E_i(1-\cos\theta_i)]}{\sum_{i=1,2} E_i(1-\cos\theta_i)}, \tag{5.6}$$
where E_i and θ_i are the energies and the polar angles of the two non-remnant jets. Neglecting the jet masses z_p corresponds to the minimum of z_1 and z_2 defined in equation 2.16. In the limit where one jet is absorbed into the proton remnant jet z_p approaches zero.
- The polar angle θ_{fwd} of the most forward non-remnant jet and the polar angle θ_{bwd} of the backward jet in the laboratory frame.
- The corresponding transverse energies $E_{T,fwd}$ and $E_{T,bwd}$.

5.3 Definition of the Dijet Samples

The ability of the y_2 variable to resolve events with dijet topologies is demonstrated qualitatively by the two selected CC events displayed in figure 5.1. Both events show the imbalance in transverse momentum characteristic for CC events. For the upper event one hadronic jet is identified in the LArC. The corresponding value of y_2 is 0.0008. The lower event shows two clearly separated jets. For this event y_2 is 0.013, roughly a factor 20 larger than for the upper event.

An alternative measure to define a dijet event selection criterion is the mean transverse energy of the two jets in the Breit-frame. In this frame the momentum transfer q has only a z-component. The struck quark in the QPM enters in the Breit frame

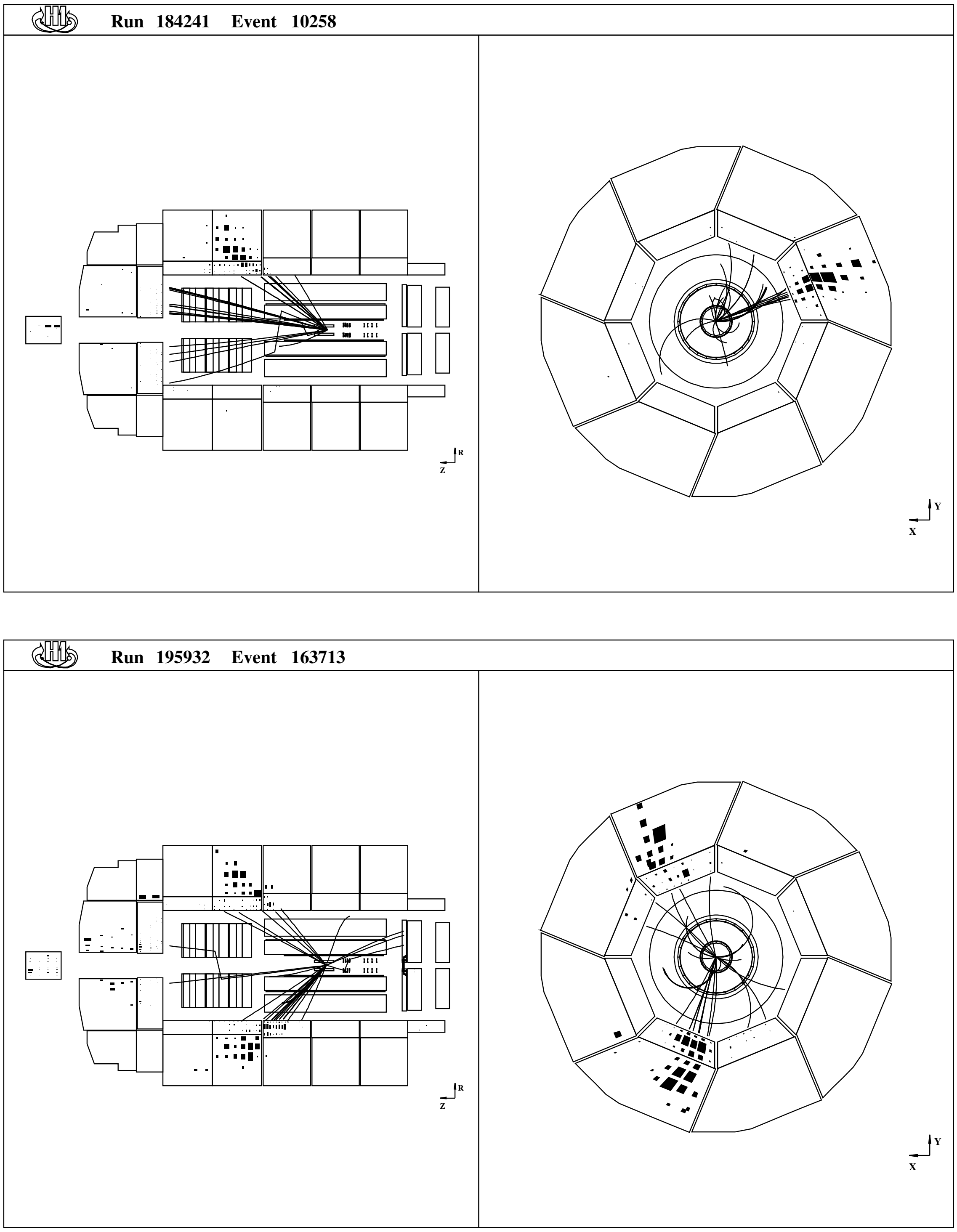

Figure 5.1: *A display of two selected CC events in the H1 detector. The full lines and filled rectangles correspond to tracks reconstructed in the tracking chambers and energy depositions in the calorimeter, respectively. For the upper event* $y_2 \approx 0.0008$ *and* $m_{12} \approx 12$ *GeV. For the the lower event* $y_2 \approx 0.013$ *and* $m_{12} \approx 80$ *GeV.*

with momentum $p_z = \frac{1}{2}Q$ and is simply rebounced from the exchanged virtual boson with momentum $p_z = -\frac{1}{2}Q$. Transverse energy in the Breit frame is produced by higher order QCD radiation. Jets with high transverse energy are thus indicative for the presence of hard QCD processes. The correlation between y_2 and the transverse jet energy in the Breit frame is studied in the following.

In figure 5.2 the mean transverse energy in the Breit-frame for CC events generated with the MC model ARIADNE is shown for three different lower y_2 limits. With increasing lower y_2 cut the distributions are clearly shifted towards higher mean transverse energies and very low transverse energy jets are effectively suppressed. For $y_2 > 0.002$ the average of the distribution is 8.3 GeV. The fraction of events classified as dijet events decreases from 40% for $y_2 > 0.001$ to roughly 20% for $y_2 > 0.003$.

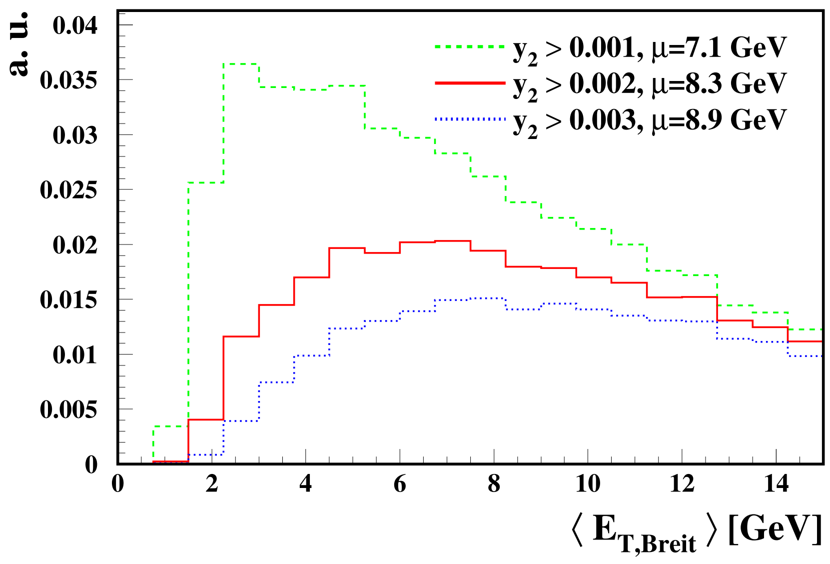

Figure 5.2: *Distribution of $\langle E_{T,Breit} \rangle$ for CC events as generated with ARIADNE for different lower y_2 limits. The mean value of the distributions is denoted μ.*

In a compromise between the limited number of CC events available and jet hardness an enriched CC *and* NC dijet sample is selected by imposing the following criteria:

- $y_2 > 0.002$,
- $10° < \theta_{jet} < 140°$.

The condition for the polar jet angles θ_{jet} restricts the jets to the acceptance of the LArC. From the 460 CC events selected 126 remain after applying these criteria. For the NC events 1 872 out of 8 623 remain as dijet events. With this definition of the dijet samples QPM-like events with only one jet originating from the struck quark are largely eliminated. Events involving higher order QCD processes are however included.

Chapter 6

Experimental Procedure

In this chapter the correction of the experimental data for detector effects, the trigger efficiency for dijet events and the systematic uncertainties of the measurement are discussed. It will be shown that the size of the detector corrections are typically below 15%, with a very small model dependence. The trigger efficiency of CC dijet events is found to be in agreement with the inclusive measurement. The total systematic error is determined to be 5% and 7% on average for the CC and the NC measurements, respectively.

6.1 Correction of the Data

Correction for detector effects

For a comparison with various theoretical predictions the measurement has to be independent of the specific experimental setup used. Thus in the present analysis the measured jet distributions have to be corrected for the effects of the limited acceptance and resolution of the H1 detector. For a binned distribution of a given observable $\mathcal{O}$, a simple way to correct the data is to multiply each bin i with the correction factor

$$C_{det,i} = \frac{O_i^{gen}}{O_i^{rec}}, \tag{6.1}$$

where O_i^{gen} is the generated ('true') value of the observable $\mathcal{O}$ and O_i^{rec} the reconstructed value in the i-th bin as predicted by the MC simulation on the hadron and detector level, respectively. [1]

[1] The correction method described above is a special case of the general approach

$$O_i^{rec} = \sum_j C_{ij} O_j^{gen}, \tag{6.2}$$

where the matrix elements C_{ij} represent the probability of reconstructing an event with true value in bin j in bin i. The data are then corrected by inverting C and multiplying it with the measured distribution. In practice, the inversion of C is a non-trivial problem. The finite statistical error of the MC simulation leads to oscillating solutions which have to be handled by complex mathematical methods [59]. In case migrations are small the off-diagonal elements of C may be neglected and (6.2) reduces to (6.1) with $C_i^D \equiv C_{ii}^{-1}$.

This simple *bin-by-bin correction factor method* does not take migration effects between individual bins into account. Its applicability is therefore limited to problems where migration effects can be kept small. This can be achieved by matching the bin sizes to the resolution of the detector for a given observable. If in addition the measured distributions are roughly described by the MC prediction on the detector level the bias on the corrected data due to residual migration effects is negligible.

Suitable measures for the size of the migrations are the *purity* and *efficiency* of a given bin. The purity (efficiency) of the i-th bin is defined as the number of events generated *and* reconstructed in bin i divided by the number of events reconstructed (generated) in that bin. In the present analysis the binning is chosen such that the purity in each bin of all distributions measured does not significantly fall below 40%. In order to facilitate a comparison the CC and NC dijet distributions are binned identically.

In the present analysis the MC models ARIADNE and LEPTO are used to correct the data. For the correction of CC events, the number of events simulated for either model is approximately 150 times larger than that of the experimental data. The number of NC events simulated is at least six times larger than that of the data. This ensures less sensitivity of the correction procedure to statistical fluctuations. The cluster and track selection criteria used for the experimental data are consistently applied to the simulated events also.

The purities and efficiencies as determined with ARIADNE and LEPTO are very similar[2]. On average both the purity and efficiency are 60%. For both the CC and NC analyses the lowest purities are observed in the last bin of the x_p distribution, being 50% and 35%, respectively. The estimated detector corrections are typically 10% with a maximum value of $\approx 20\%$ observed in the third bin of the x_p distribution. The model dependence of the correction factors is very small for all distributions. Statistically significant deviations between ARIADNE and LEPTO are only present in the first bin of the m_{12} distribution and the second bin of the CC z_p distribution. The correction factors and the bin purities and efficiencies of selected distributions are summarized in figure 6.1 and 6.2 for the CC and NC analysis.

The consistency of the correction has been tested by applying the correction factors determined with ARIADNE to the LEPTO prediction at the detector level. The agreement between the corrected jet distributions and the true LEPTO jet distributions on the hadron level is of the order of a few per cent. The largest deviations of 10% are observed in the m_{12} and z_p distributions.

The same results are obtained for the dijet distributions with the additional requirement $Q^2 > 5\,000$ GeV^2 (not shown). Here, a slight trend towards smaller detector corrections is observed, which is expected from the more energetic and pronounced jets at higher Q^2.

[2]The results presented in the following apply equally to the CC and NC analysis, unless stated otherwise.

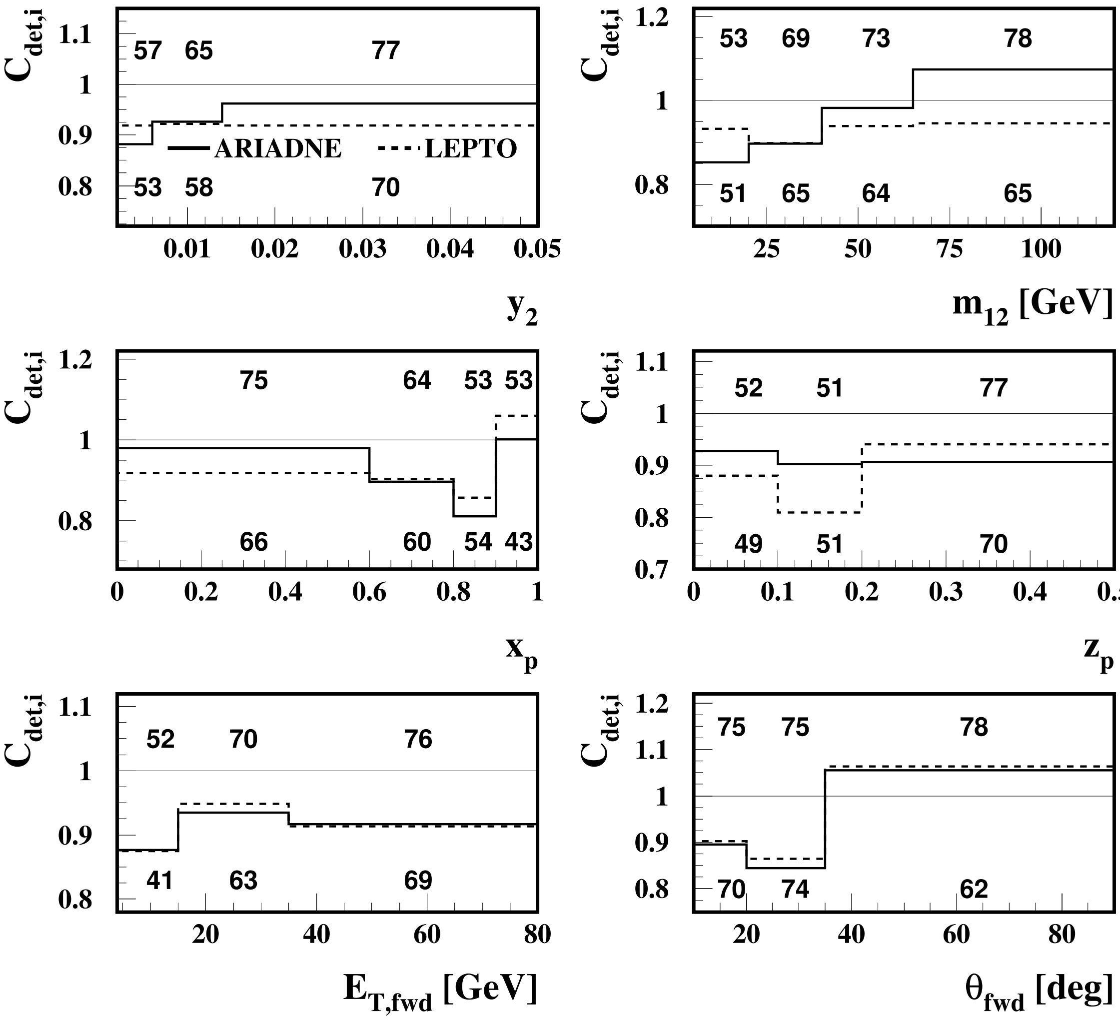

Figure 6.1: *Detector correction factors for the CC analysis as predicted by ARIADNE and LEPTO. The upper (lower) row of numbers is the average of the purities (efficiencies) in per cent for each bin determined with ARIADNE and LEPTO.*

Correction for effects of QED radiation

None of the NLO programs introduced in section 3.2 implement QED radiation off the initial and final state leptons. In addition to the correction for detector effects the data are therefore also corrected for QED radiative processes. For this purpose two additional MC event samples are generated for both ARIADNE and LEPTO. The first sample corresponds to the one used above for the determination of the detector corrections but it contains much more events. The second is the same but now QED radiative processes are excluded. As above a correction factor for each bin i can then be determined as

$$C_{QED,i} \equiv \frac{O_i^{gen}(\text{w/o QED corr.})}{O_i^{gen}(\text{with QED corr.})}, \tag{6.3}$$

where O_i^{gen} is the generated value of a given observable O in the i-th bin with and without QED radiative processes. The hadronic final state of events simulated including QED radiative processes is defined in close analogy to the experimental conditions.

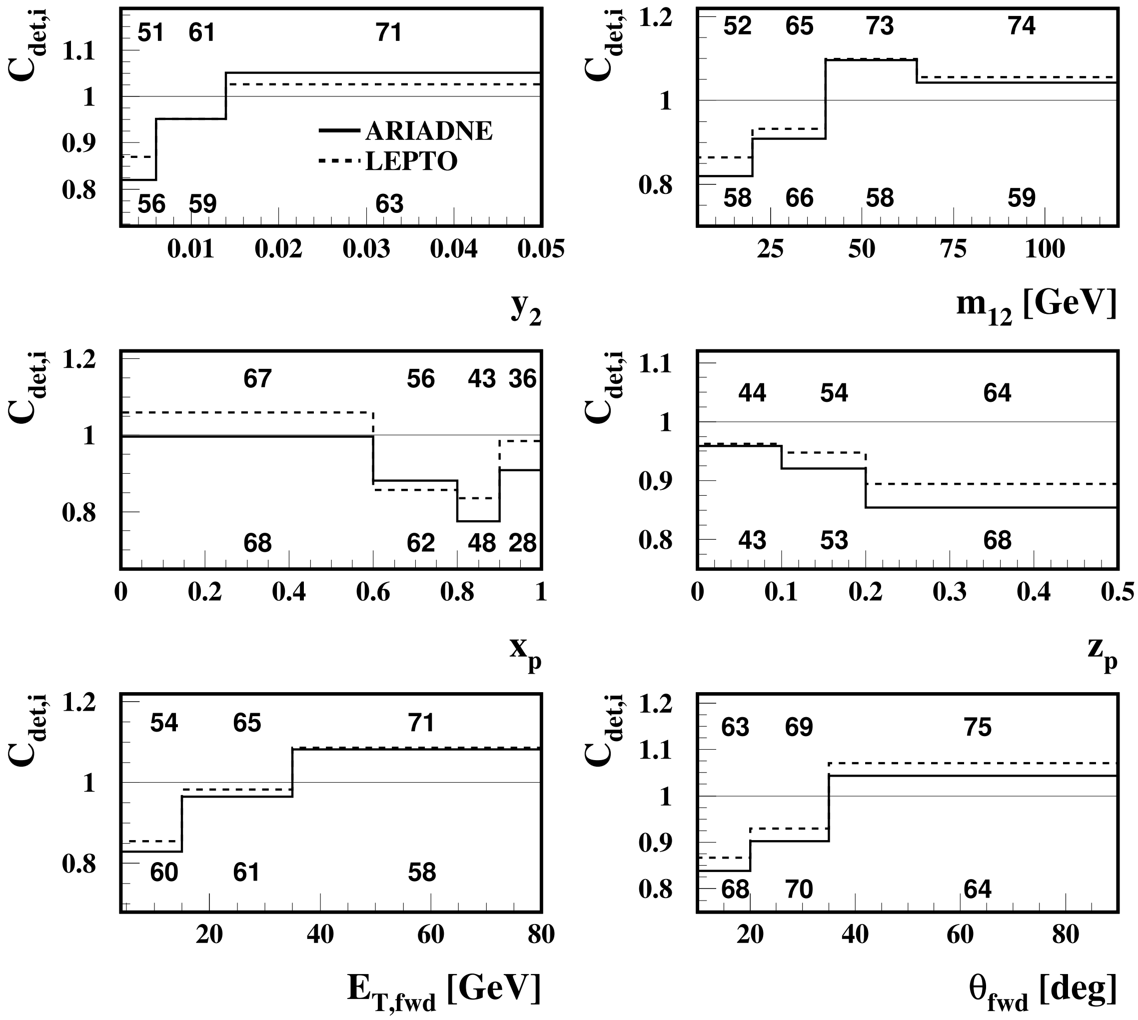

Figure 6.2: *Detector correction factors for the NC analysis as predicted by ARIADNE and LEPTO. The upper (lower) row of numbers is the average of the purities (efficiencies) in per cent for each bin determined with ARIADNE and LEPTO.*

Bremsstrahlung photons emitted off the incoming positron at polar angles less than 5° are excluded from the hadronic final state. Experimentally these photons are lost in the beam pipe. The scattered positron in NC events and a photon radiated from it are merged if the latter was emitted with an angle less than 5° relative to the direction of the scattered positron. This simulates the limited detector resolution. Note that this procedure leads to stable and small correction factors. Different definitions of the hadronic final state in the presence of QED radiative processes should, however, result in the same corrected data distributions.

The size of the QED corrections is typically 5% for both the CC and NC distributions. For the CC analysis the largest effect of ≈10% is seen in the x_p distribution. For the NC analysis the maximum correction is 10% in the tail of the m_{12} distribution. The model dependence of the correction factors is always smaller than 5%. No significant Q^2 dependence of the size of the corrections is observed.

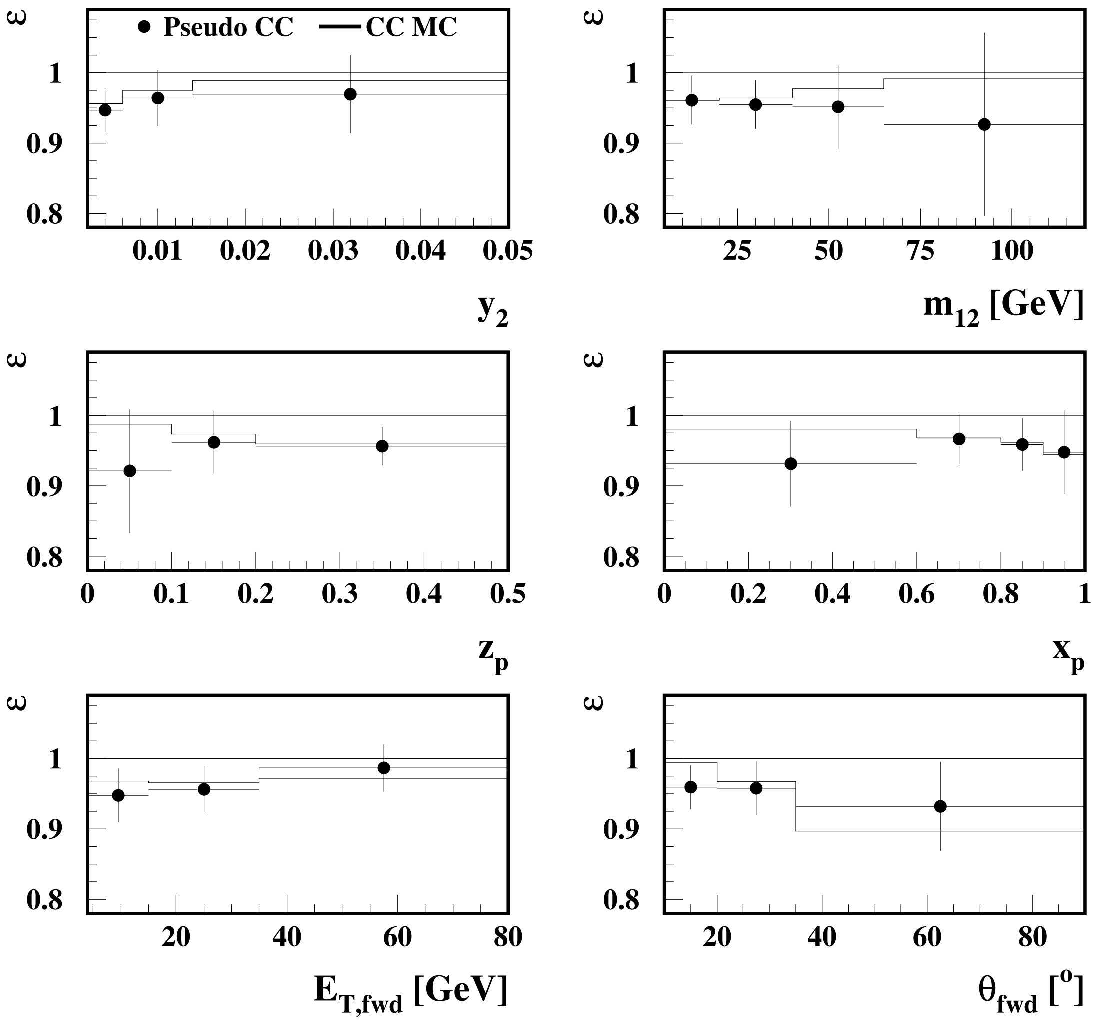

Figure 6.3: *Trigger efficiencies for dijet events determined from the 1994–1997 Pseudo CC data. The ARIADNE prediction is combined with the 1996 H1 detector simulation.*

The final correction factor is taken to be the average of the combined detector and QED radiation correction factors from ARIADNE and LEPTO for each bin.

6.2 Trigger Efficiency for Dijet Events

The CC trigger efficiency of 94% quoted in section 4.3 is determined on the basis of the inclusive event sample. This is dominated by one-jet-like events, for which the hadronic final state is mostly concentrated in one particular part of the detector. In order to investigate a possible dependence of the CC trigger efficiency on the event topology the trigger efficiency is re-determined for the dijet event sample as defined in section 5.3. Again the pseudo CC technique is applied with the subtriggers ST66 and ST77 as described in section 4.3.

The CC trigger efficiency for selected dijet variables is shown in figure 6.3. The average CC trigger efficiency is ≈95%, confirming the results obtained in section 4.3. It is essentially a flat function of each individual dijet variable, within the relatively large statistical errors. A significant decrease of the trigger efficiency for hard dijet events, which are predominantly expected at high y_2 or m_{12}, is not observed. The trigger efficiencies determined from the data are well described by the MC prediction including the H1 detector simulation. The measured CC distributions are corrected for the trigger inefficiencies using the results derived with the pseudo CC data.

The selection of NC events relies almost completely on the identification of the scattered positron in the LArC. Thus any possible dependence of the trigger efficiency on the event topology is expected to be very small. In fact in [60] it is shown that the trigger efficiency for pronounced dijet events differs by less than 1% from the inclusive trigger efficiency.

6.3 Experimental Systematic Error

Three major sources of experimental systematic error are considered in the present analysis: the uncertainty in the hadronic energy scale of the LArC; the model dependence of the correction factors; the uncertainty in the scattered positron energy measurement (for NC events only). The total systematic error is taken as the quadratic sum of the individual contributions. The results summarized below are listed in detail in appendix A.

Hadronic energy calibration

In [2] a systematic uncertainty of 2% on the relative hadronic energy scale is quoted. This improvement was mainly achieved after applying the techniques for the combination of cluster and tracking information, described in section 4.2. However, the calibration is based on an inclusive data sample consisting mostly of events with one well reconstructed jet in the LArC. Thus it is not necessarily applicable for specific final state topologies as e.g. in dijet events.

In the present analysis the hadronic energy scale uncertainty is conservatively taken to be 4% as determined in [14]. This is justified by exploiting the transverse momentum balance between the precisely measured scattered positron and the hadronic system in NC events. The ratio P_T^h/P_T^e is shown for the NC dijet sample defined in section 5.3 in the left plot of figure 6.4 together with the prediction of ARIADNE. Due to miscalibration, energy losses in passive detector material or hadronic showers not (fully) contained in the LArC the events are on average not perfectly balanced ($\langle P_T^h/P_T^e\rangle \approx 0.95$). The deviations between the data and the MC simulation are a measure of the uncertainty on the hadronic energy scale. Varying the energies of hadronic clusters of the MC simulation around the assumed $\pm 4\%$ yields the shaded areas shown in the right plot of figure 6.4. The data points are well contained within this spread.

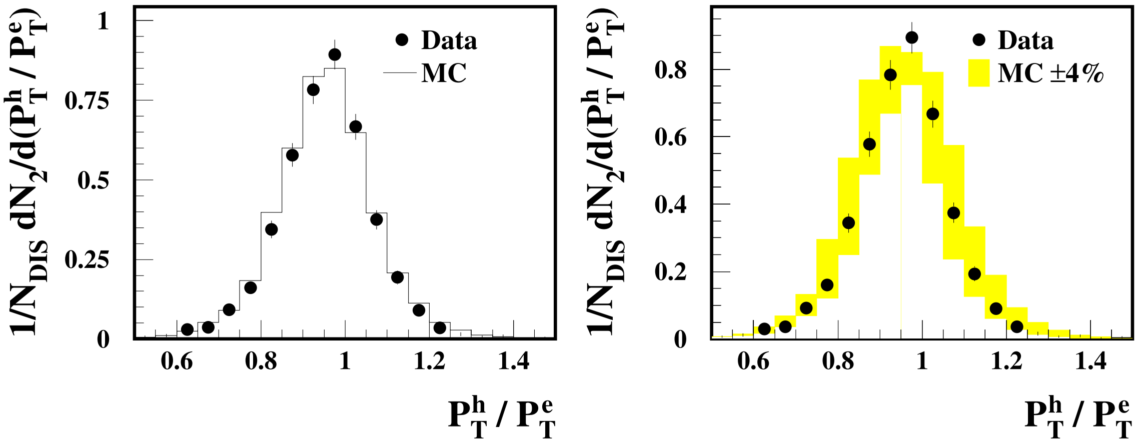

Figure 6.4: *Transverse momentum balance between the scattered positron and the hadronic final state for the selected NC dijet events together with the predictions of ARIADNE. The shaded areas represent a variation of ±4% of hadronic MC cluster energies.*

The systematic effect of this uncertainty on the measured dijet distributions is estimated by repeating the analysis with the energies of hadronic clusters shifted by ±4%. The energy shift is applied to the MC simulation and not to the data. This reduces the influence of statistical fluctuations. The observed changes in the dijet distributions depend considerably on the variable studied. For the y_2 distribution a systematic effect of ≈3% is observed. Here a small effect is expected because calibration factors largely cancel in the definition of y_2 (cf. equation 5.4). Relatively large effects up to a maximum of 11% are observed in single bins of the m_{12}, x_p and $E_{T,fwd(bwd)}$ distributions. Small errors of less than 3% are observed for the jet polar angle distributions which depend only indirectly on the hadronic energy measurement. Similar effects are observed for the NC measurement. For the dijet distributions measured at $Q^2 > 5\,000$ GeV^2 the observed effects are of comparable size.

An assumed uncertainty of ±3% on the track momenta of charged particles leads to an error of less than one percent on average for the CC and the NC measurement.

Positron energy calibration

The error on the absolute electromagnetic energy scale depends on the specific wheel of the LArC considered [2]. An error of 0.7% is assigned to the CB1-CB2 wheels. For the majority of the selected NC events the positron is scattered in this part of the detector. The uncertainty increases up to 3% in the most forward part of the LArC.

The effect of the electromagnetic energy scale uncertainty on the measured NC dijet distributions is estimated by shifting the energy of the electromagnetic cluster associated to the scattered electron accordingly. Again this is done for the MC simulation rather than for the experimental data. The size of the resulting changes is in the order of 1% for the majority of the variables studied. The maximum effect of approximately

3% is observed in the θ_{fwd} distribution. For $Q^2 > 5\ 000$ GeV^2 the systematic error tends to be larger as is expected due to the increased uncertainty of the electromagnetic energy scale in the forward region.

Model dependence of correction factors

The systematic error due to the model dependence of the correction factors is taken to be the average difference between the two data distributions corrected with ARIADNE and LEPTO. The error is smaller than 3% on average for both the CC and the NC measurements. The largest error of 11% is observed in the CC z_p distribution and is most probably overestimated. The comparison with the measured z_p distribution and the other MC models suggest a technical bug of the LEPTO program.

Total systematic error

The total systematic error is 5% on average for the CC measurement. For the NC measurement the combined systematic uncertainty is ≈7%. The difference is mostly due to the electromagnetic energy scale uncertainty which has no effect on the CC measurement. Compared with the statistical error of ≈20% the accuracy of the CC measurement is clearly limited by the small number of CC events available. For the NC measurement the total systematic error and the statistical error of ≈6% on average are of comparable size.

Chapter 7

Results

In this chapter the main results of the CC and NC dijet measurements are presented. The first differential CC dijet distributions are shown and compared to MC models and to perturbative QCD calculations in NLO. Charged current and NC dijet production at $Q^2 > 5\ 000$ GeV^2 is studied in detail. The jet structure of NC events at $Q^2 > 10\ 000$ GeV^2 is analysed and compared to the standard model expectation. Finally, a direct, model independent comparison of the CC and NC dijet data is presented. It allows an investigation of the expected independence of QCD processes from the underlying electroweak scattering vertex.

The presented differential dijet cross sections are normalized to the respective total DIS cross section for the kinematic selections defined in sections 4.3 and 4.4. The measured distributions are always corrected for detector effects and QED radiative processes as described in the previous chapter. The quoted total errors of the CC and NC measurements are defined as the quadratic sum of the statistical and the total experimental systematic error. The numerical values of the measured differential dijet event rates are listed in appendix A.

7.1 Comparison with MC Predictions

The measured CC differential dijet event rates are introduced in figure 7.1. They are based on the 126 events remaining after the jet selection. The y_2 and m_{12} distributions are strongly decreasing. The events with clear dijet structures are situated in the tails of these distributions. The highest invariant dijet mass with $\approx$80 GeV is reconstructed for the event displayed in the lower part of figure 5.1. The sample contains four events with $m_{12} > 65$ GeV and 13 events with $y_2 > 0.014$. The z_p distribution shows a drop at small values of z_p. This is due to the dijet selection cut $y_2 > 0.002$. The x_p distribution is peaked towards large x_p values, because the minimum Q^2 of the selected events is already large. Note that the mean Q^2 of the dijet sample is $\approx 3\ 000$ GeV^2 and the mean $m_{12}^2 \approx 1\ 000$ GeV^2. The average value of ξ is approximately 0.1.

The forward jet distributions are strongly increasing at small polar angles and small transverse energies. This is qualitatively expected for gluon bremsstrahlung off an incoming quark. The mean polar angle of the forward jet is ≈20°, the mean transverse energy in the laboratory frame ≈18 GeV. Although clearly shifted towards larger angles the backward jet is also predominantly measured in the forward part of the detector. This is due to the large average x transferred to the current jet at high Q^2.

The same characteristics are observed for the NC dijet distributions displayed in figure 7.2. They contain the 1 872 events having passed the jet selection requirements, defined in section 5.3. The highest invariant dijet mass observed is 115 GeV. Note that the total error of the NC measurement is much smaller than that of the CC measurement due to the reduced statistical error.

The corrected dijet distributions are compared to the predictions of ARIADNE, LEPTO, HERWIG and RAPGAP on hadron level. Overall, the CC and NC data are best described by ARIADNE. The prediction of ARIADNE is almost always contained within the statistical error of the data. The same is true for the RAPGAP model with the exception of the NC $\theta_{fwd}, \theta_{bwd}$ and x_p distributions where RAPGAP overshoots the data at the peak values. Note that these bins are strongly correlated. HERWIG tends to overestimate the CC and NC data in various distributions. It nevertheless provides a reasonable description of the data. In contrast, LEPTO has serious problems in reproducing the data distributions. For both the CC and NC measurement it significantly overshoots the data at high y_2 values and generally tends to predict larger invariant dijet masses. It fails to describe the z_p distributions. These observations are of particular interest because both LEPTO and RAPGAP are based on DGLAP parton showers and the Lund string fragmentation model (cf. section 3.1). They differ, however, in the procedure used to match the LO matrix elements and the parton showers. The observed discrepancies may be related to this difference.

7.2 Comparison with pQCD in NLO

The outcome of perturbative QCD calculations are properties of *parton* jets. A comparison with the corrected data therefore makes necessary an estimation of the size of the non-perturbative hadronization effects. This is achieved by comparing the jet distributions of the MC simulation after hadronization and after parton showering. The MC models ARIADNE and HERWIG are studied below because they are based on different hadronization models (cf. section 3.1).

The predicted hadronization corrections are on average smaller than 15% as is illustrated in figure 7.3 for the y_2 and $E_{T,fwd}$ distributions. The difference between HERWIG and ARIADNE is typically less than 10%. It increases up to 20% in the regions where the events with less pronounced jet structures are expected, e.g. at low y_2 and m_{12}. Generally, HERWIG predicts more dijet events on the parton level than on the hadron level, whereas for ARIADNE the sign of the correction may change within

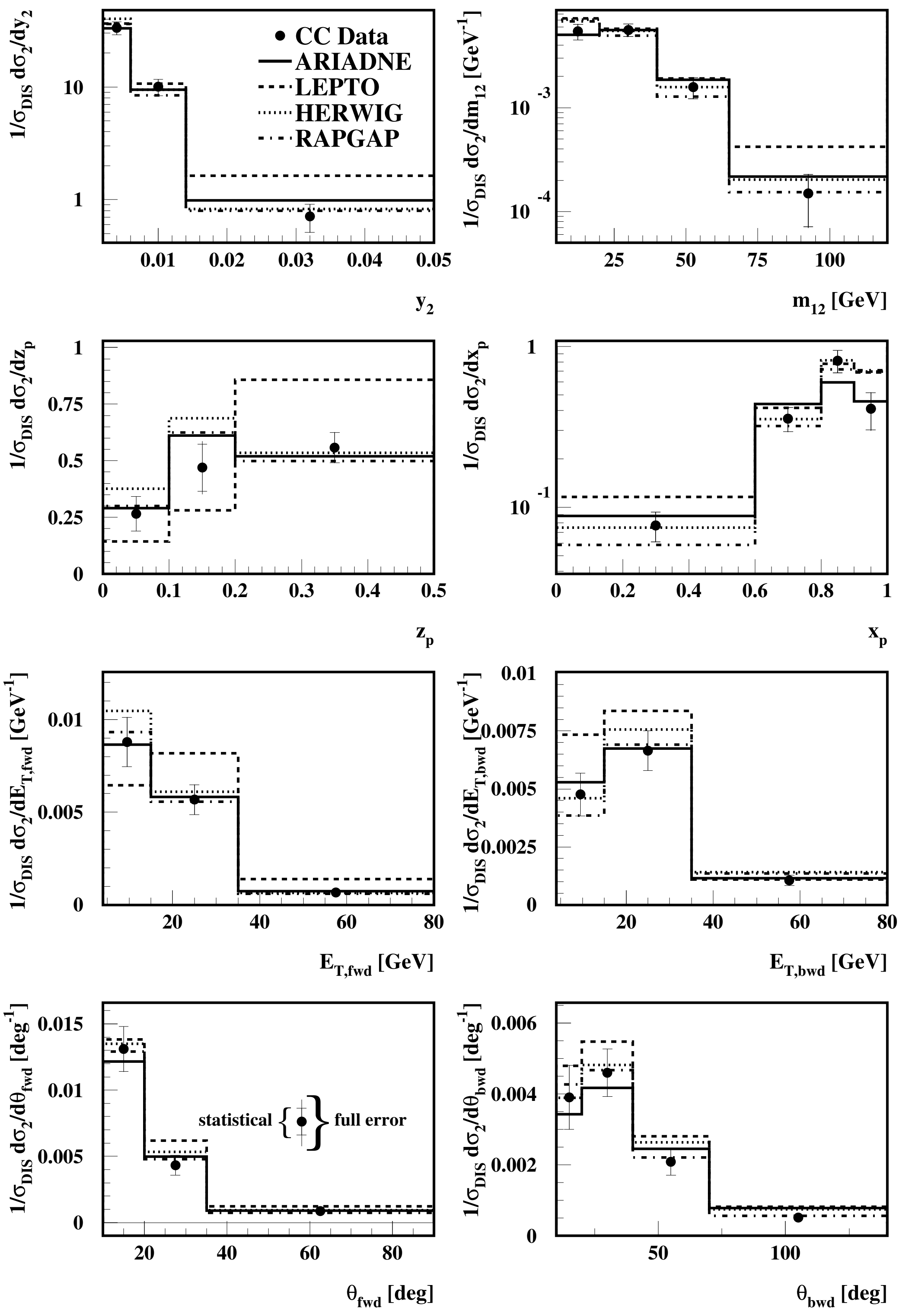

Figure 7.1: *Dijet distributions for CC events together with the predictions of ARIADNE, LEPTO, HERWIG and RAPGAP. The data are corrected for detector effects and QED radiative processes.*

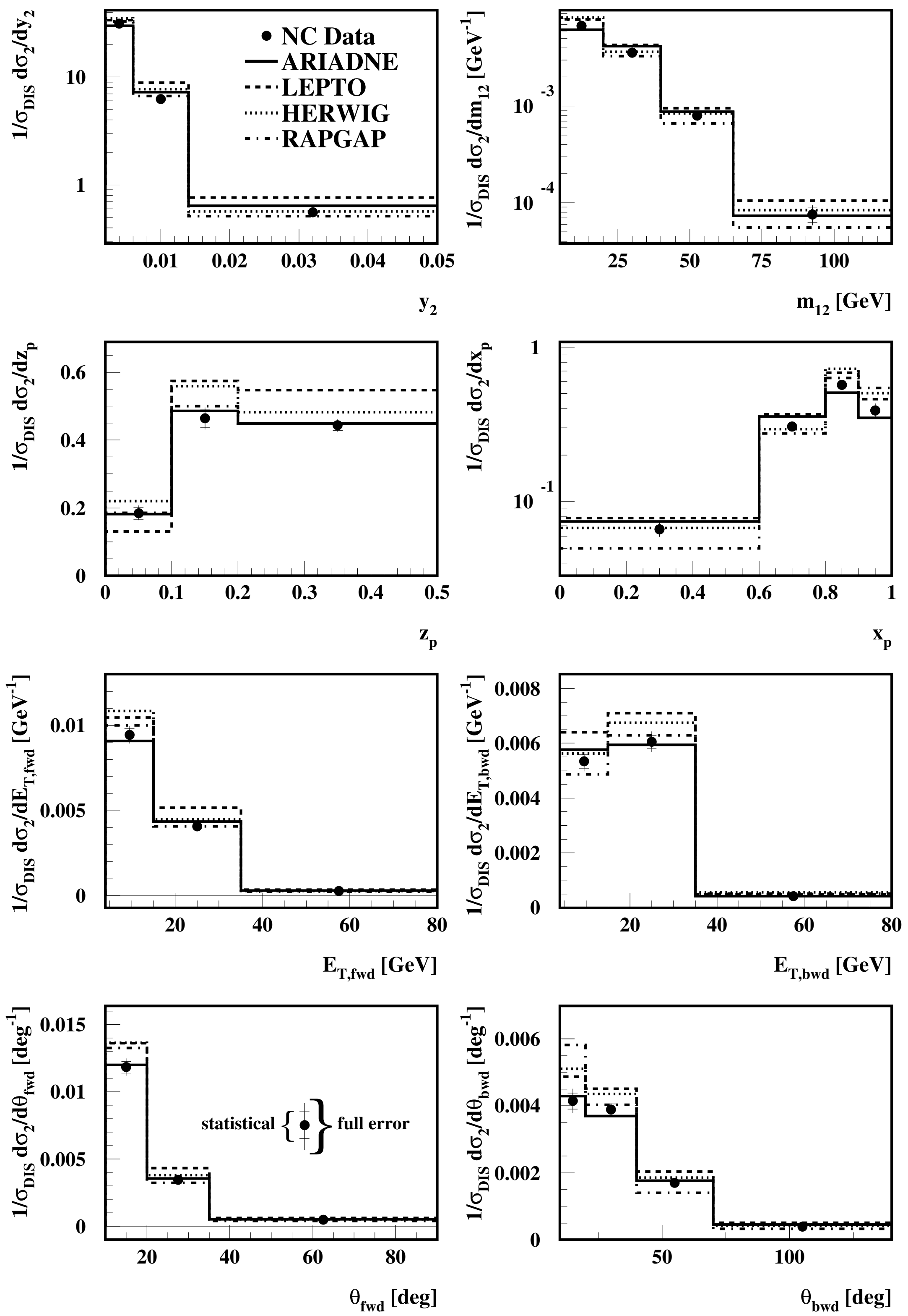

Figure 7.2: *Dijet distributions for NC events together with the predictions of ARIADNE, LEPTO, HERWIG and RAPGAP. The data are corrected for detector effects and QED radiative processes.*

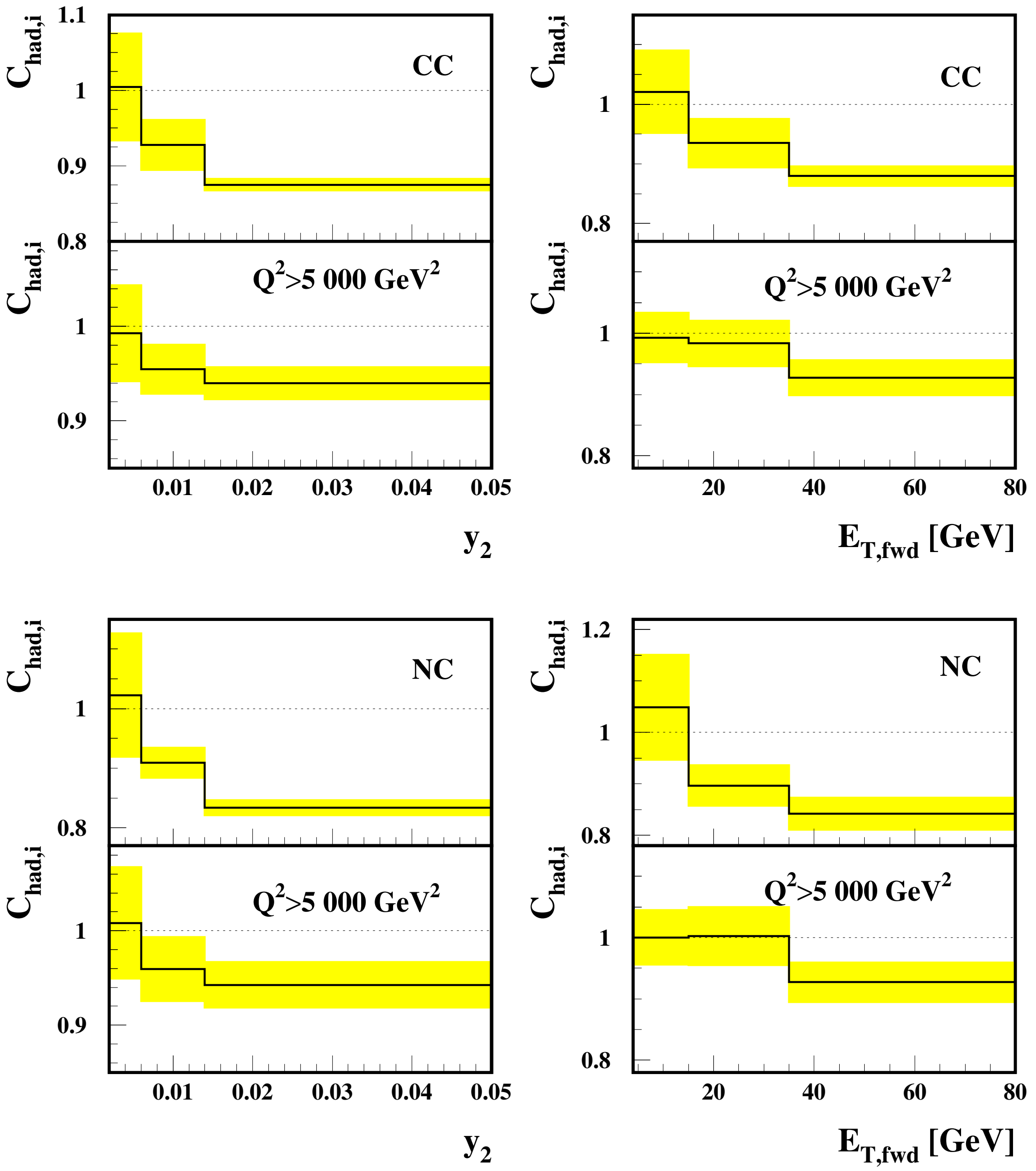

Figure 7.3: *Hadronization corrections for CC and NC dijet distributions. The shaded areas indicate the spread as predicted by ARIADNE and HERWIG. The full line is the mean hadronization correction factor applied to the NLO calculations.*

a given distribution (not shown). A trend towards smaller corrections is observed with increasing Q^2. This is in principle expected from the alternative approach of analytical power corrections which are typically of the order $1/Q^p$, where p is an integer [61].

The average hadronization corrections and the accuracy of the measurement are of comparable size. Therefore the pQCD calculations are corrected bin-by-bin using the mean of the correction factor as predicted by the two MC models (full line in figure 7.3). The spread of the predictions of ARIADNE and HERWIG is taken as the systematic uncertainty.

The pQCD calculations are performed in NLO with the program MEPJET for CC and with DISENT for NC processes. The proton parton densities (PDF) used in the calculations are taken from a QCD fit to the H1 measurement of the inclusive DIS cross section [2]. The value of the strong coupling α_s at the Z^0 mass is set to 0.1183, as assumed in the PDF's. The renormalization and factorization scale is chosen to be Q unless otherwise stated.

Results

The CC dijet distributions are compared to the NLO calculations in figure 7.4. MEPJET provides a reasonable description of the data within the experimental errors of $\approx$20%. The maximum deviation is $\approx$35%, observed in single bins of the y_2, m_{12}, z_p and x_p distributions. The MEPJET prediction tends to underestimate the data in several bins of various distributions. However, possible inconsistencies of the MEPJET prediction, which are observed for the NC calculations (cf. section 3.2), cannot be resolved with the current experimental precision of the CC measurement.

Given the direct evidence provided by the lower CC event displayed in figure 5.1 and the significant number of CC events at high y_2 and m_{12} the existence of dijet events in CC interactions is clearly established. The overall agreement with the NLO calculations confirms this statement at a quantitative level. As discussed in section 2.4 quark-induced *and* gluon-induced processes contribute to the dijet cross section. Due to the steeply falling gluon distribution of the proton as a function of x and the implicitly high x of $\approx$0.1 of the CC selection, the gluon induced processes are, however, strongly suppressed.

The NLO calculations for the quark- and gluon-induced processes are shown separately in figure 7.4[1]. The predicted fraction of gluon-induced events is 20% for the phase space covered in this analysis. It changes by less than 1% when varying the renormalization or factorization scale Q between $Q/2$ and $2Q$. The comparison suggests that both processes are needed to consistently describe dijet production in CC interactions. The large statistical errors and the small fraction of gluon-induced processes, however, forbid a quantitative conclusion.

The NC dijet data are compared to the pQCD predictions in figure 7.5. The DISENT calculation gives a good description of the measured data. The precision of the test of pQCD is much increased compared with the CC analysis and is $\approx$10% on average. The largest deviations are $\approx$20%, observed in the highest m_{12} and x_p bins. Figure 7.5 also shows the pure NLO calculation, i.e. without application of the hadronization correction factors. The corrections, although small, always lead to an improved data description.

Due to the slightly higher average x of the NC data sample the predicted fraction of gluon-induced processes is $\approx$15%, smaller than in the CC analysis. The quark-induced contribution to the (normalized) dijet cross section is also shown in figure 7.5.

[1]Note that the quark- and gluon-induced contributions to the dijet cross section are also normalized to the total DIS cross section including both processes.

As known from previous measurements at low Q^2 (e.g. [14, 62]) the gluon-induced processes are needed to describe the measured data.

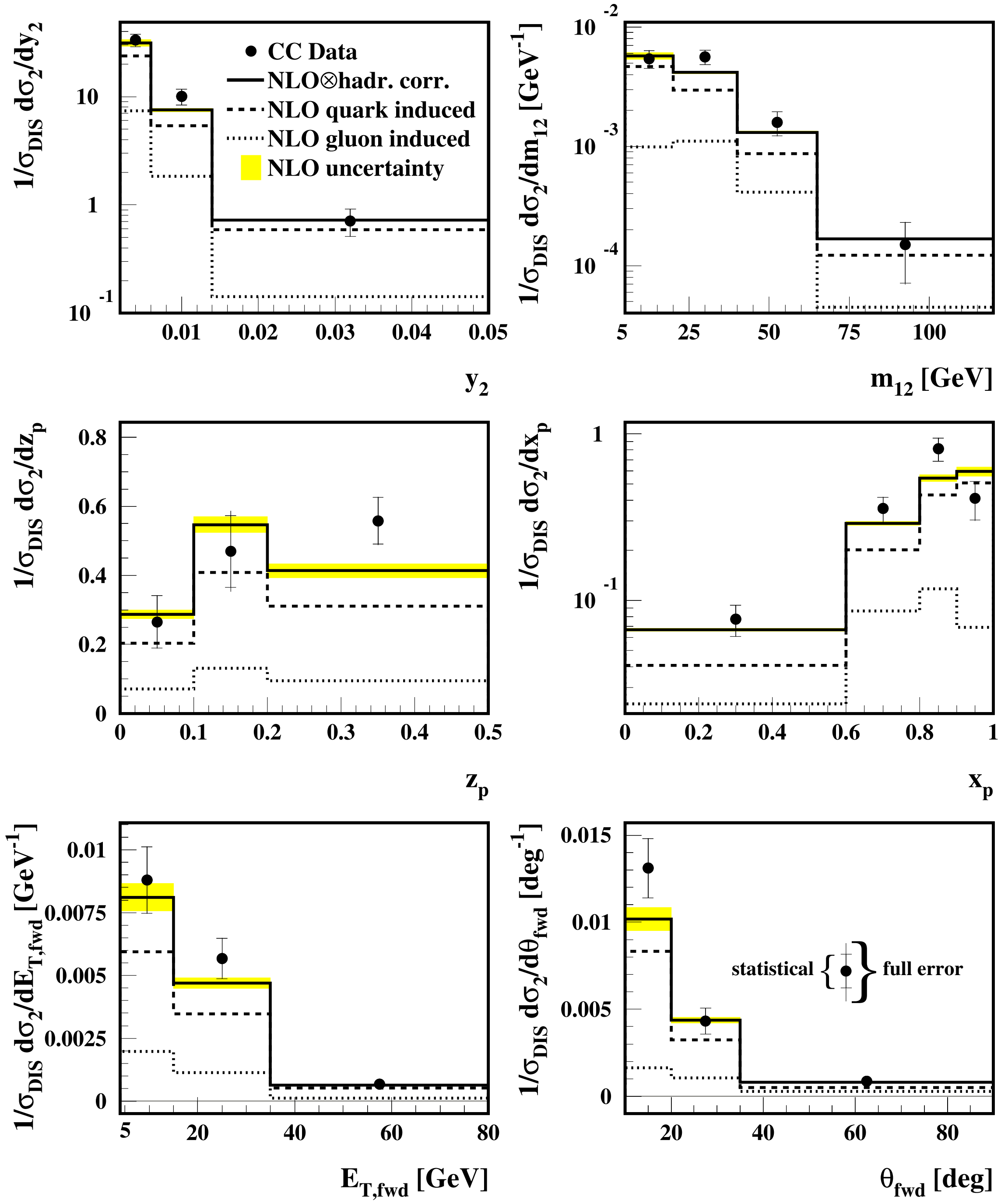

Figure 7.4: *Dijet distributions for CC events. The NLO pQCD calculations are corrected for hadronization effects. The shaded areas represent the uncertainties of the hadronization corrections. In addition, the dijet distributions for quark- and gluon-induced processes are shown separately.*

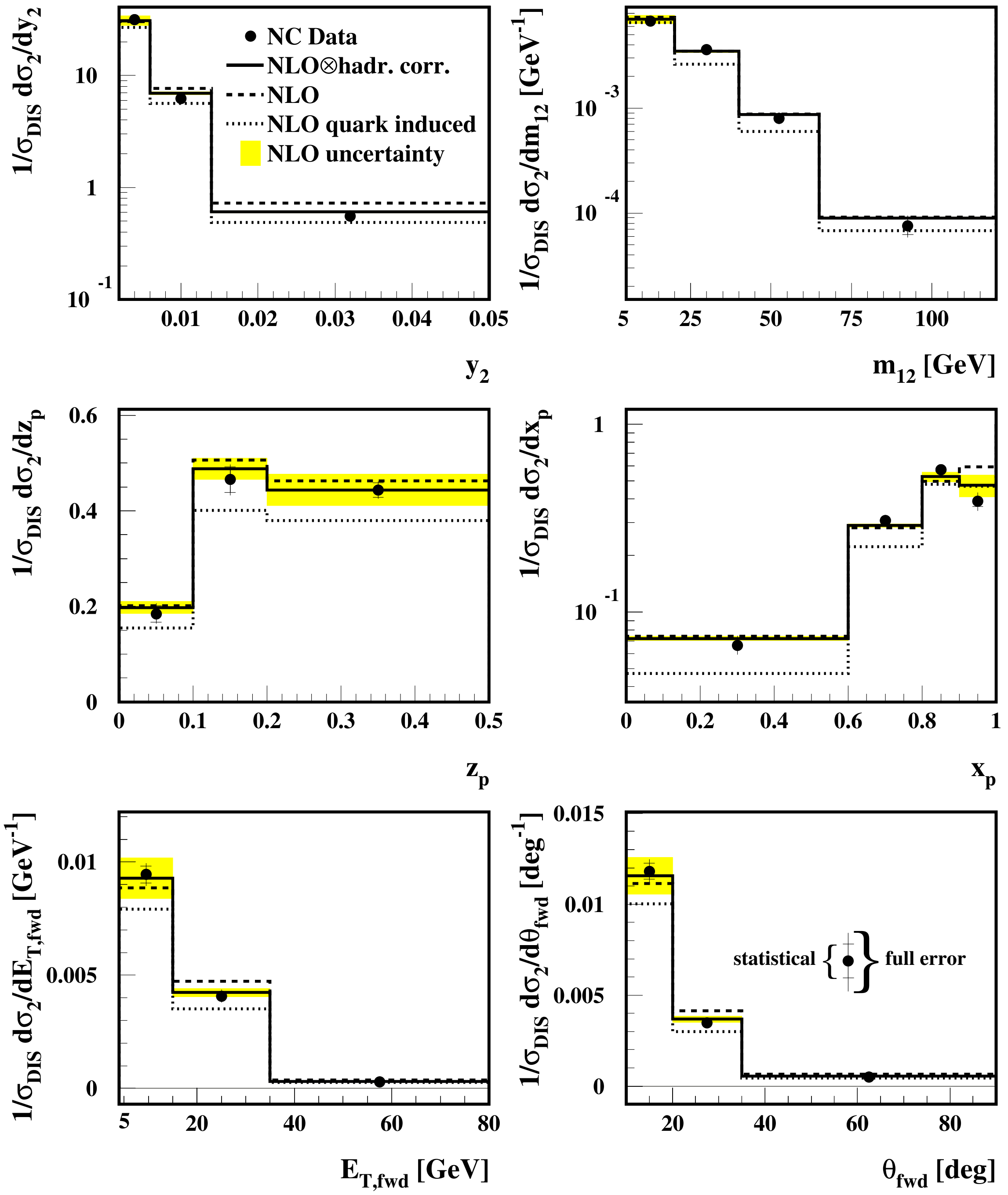

Figure 7.5: *Dijet distributions for NC events. The NLO pQCD calculations are shown with (full line) and without (dashed line) hadronization corrections. The shaded areas represent the uncertainties of the hadronization corrections. In addition, the dijet distributions for quark-induced processes are shown separately.*

Uncertainties of the NLO calculations

The truncation of the perturbation series in NLO introduces a dependence of the calculations on the renormalization scale μ_R. The size of the scale dependence is related to the size of the unknown higher order corrections and may depend on the choice made for μ_R. This choice is in principle arbitrary but it should correspond to a relevant energy scale of the process. Besides Q, the mean transverse energy of the jets in the Breit frame $\langle E_{T,Breit} \rangle$ is frequently chosen as the renormalization scale. For a given choice of μ_R there is no stringent theoretical prescription of how to estimate the uncertainty assigned to the NLO calculations. Conventionally the spread of the calculations from a variation of μ_R by factors of $1/2$ and 2 is taken as the theoretical uncertainty.

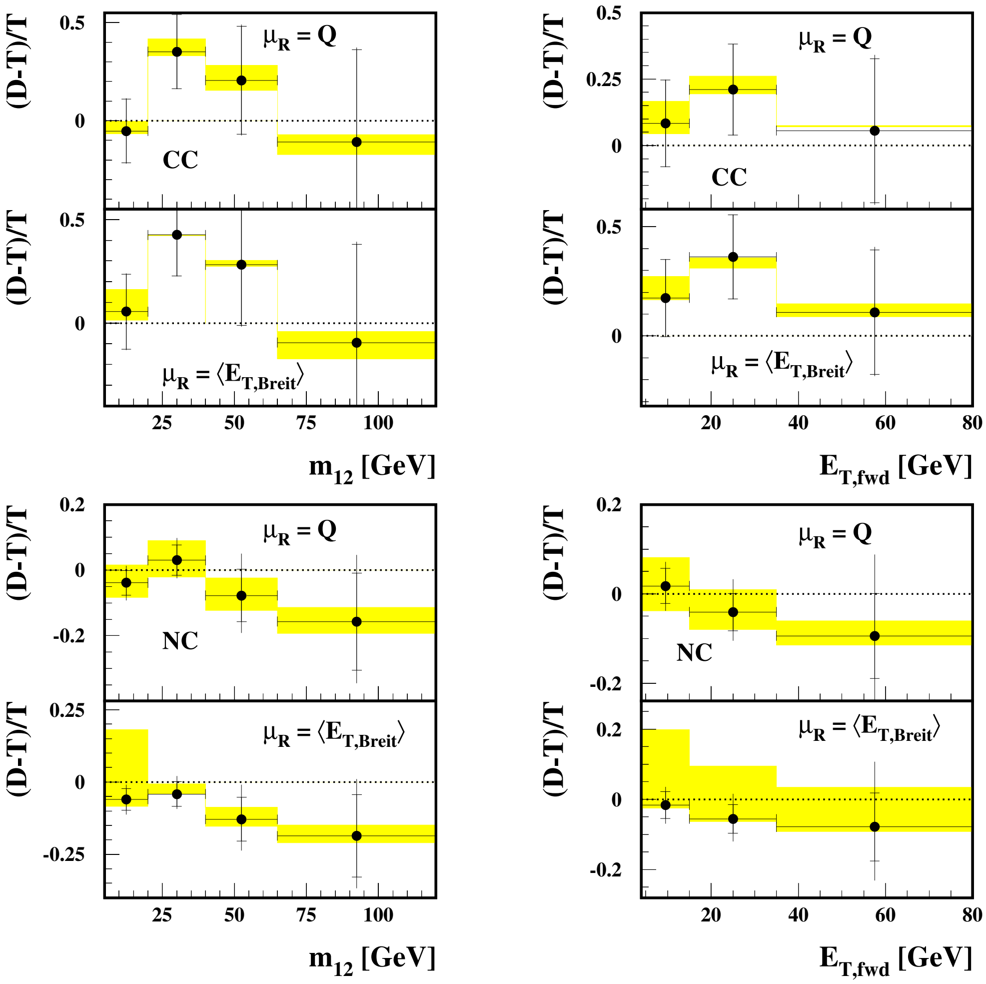

Figure 7.6: *Relative deviation of the CC (upper plots) and NC (lower plots) data from the respective NLO pQCD predictions for two different choices of the renormalization scale μ_r. The shaded areas reflect the uncertainty due to a variation of either scale Q and $\langle E_{T,Breit} \rangle$ by factors of* $1/2$ *and* 2.

The uncertainty related to the choice $\mu_R = Q$ for the present analysis is illustrated in figure 7.6 for the m_{12} and $E_{T,fwd}$ distributions. The relative deviations of the CC and NC data from the respective NLO predictions are shown. The shaded areas indicate the effect of a variation of μ_R as defined above. The uncertainty is always less than 10% for both the CC and NC calculations. The same is shown for $\mu_R = \langle E_{T,Breit} \rangle$ in the lower part of each plot. Firstly, one realizes that with this choice of μ_R the CC and NC data are also well described by the NLO calculations. The NLO calculations are changed by typically 5% with respect to $\mu_R = Q$. Note that $\langle E_{T,Breit} \rangle$ can be as low as 2–3 GeV for a given event. Its average value, however, is ≈10 GeV. The uncertainty estimated for $\mu_R = \langle E_{T,Breit} \rangle$ is slightly larger than for $\mu_R = Q$. It increases up to 20% in the regions where soft particle emissions dominate, e.g. at low invariant dijet masses. The same results are obtained for the other jet variables (not shown).

The corresponding uncertainty associated with the choice of the factorization scale μ_F is estimated to be negligible. The NLO calculations change by less than 2%, when varying μ_F between $Q/2$ and $2Q$.

Another source of uncertainty on the NLO calculations is introduced by the choice of the set of proton parton densities used as input. The PDF's may differ in the data sets used for the fits, the form of the parameterization of the individual parton densities, the scale at which the DGLAP evolution starts and the assumed value of α_s. The effect of different PDF's on the dijet distributions is estimated by using four alternative sets of PDF's in the NLO calculations: the most recent CTEQ 5M [63] and MRST4 [64] parameterizations and the older CTEQ4A3 [35] and MRSA′3 [65] sets.

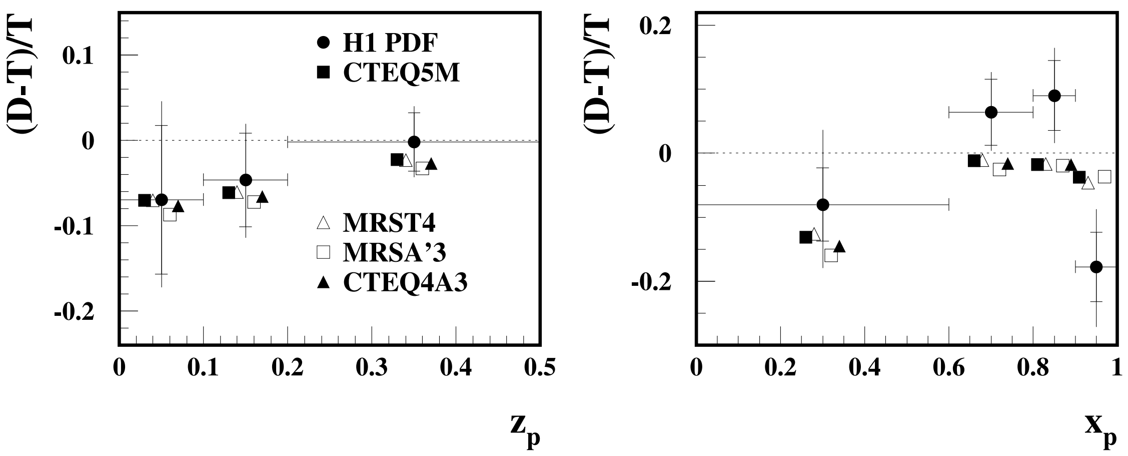

Figure 7.7: *Relative deviation of the NC data from the NLO pQCD predictions for different sets of parton density functions.*

The results are illustrated in figure 7.7 for the z_p and x_p distributions. Shown is the relative deviation of the NC data from the NLO calculations performed with DISENT. For the z_p distribution the predictions for all five sets usually agree within a few percent. The same is true for the other jet variables (not shown). In general a slight trend for a global difference between the H1 PDF's and the other sets is observed.

This is not unexpected because the H1 PDF's contain different and more recent data. The trend is enhanced at large x_p values. The difference increases from ≈5% at low x_p values to ≈15% in the highest x_p bin. All sets of PDF's used, however, agree within the experimental errors. The same results are observed for the CC NLO calculations with MEPJET.

In section 3.2 systematic differences between the available NLO programs were mentioned. In order to study whether these differences are also present in the dijet phase space covered in this analysis, the NC NLO calculations were also performed with MEPJET and JETVIP[2]. The results are presented in figure 7.8 for the y_2 and θ_{fwd} distributions. Whereas the DISENT and JETVIP predictions agree within ≈2%, the MEPJET calculation generally differs by 5–10% from the two programs and is clearly disfavored by the NC data. The same is observed for the other jet distributions. This confirms the results of [46].

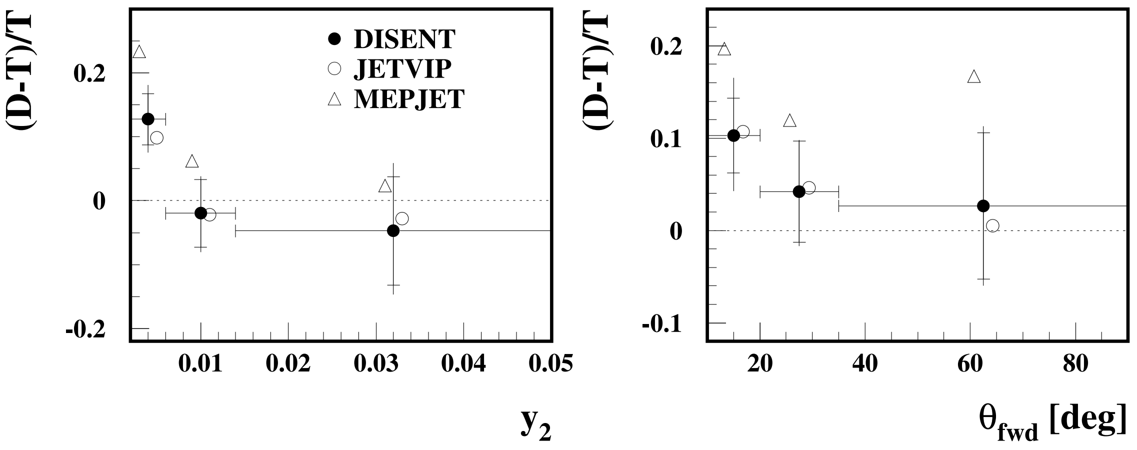

Figure 7.8: *Relative deviations of the NC data from the NLO pQCD predictions as calculated by the programs DISENT, MEPJET, and JETVIP. In the pQCD calculations the GRV HO 94 set of parton densities is used.*

NLO corrections

The size of the NLO corrections for the phase space covered in this analysis was estimated by comparing the NLO and LO calculations of DISENT[3]. The size of the NLO corrections, frequently referred to as the k-factor, is ≈20% for all bins of all distributions, independent of Q^2. The same results are obtained with MEPJET. In figure 7.9 the measured NC m_{12} and θ_{fwd} distributions are compared to the NLO and LO predictions. The LO predictions are not compatible with the data.

[2]In JETVIP the phase space slicing parameter y_{cut} is set to 3×10^{-4}.
[3]The same PDF's and the same value of α_s are used in the LO and NLO calculations.

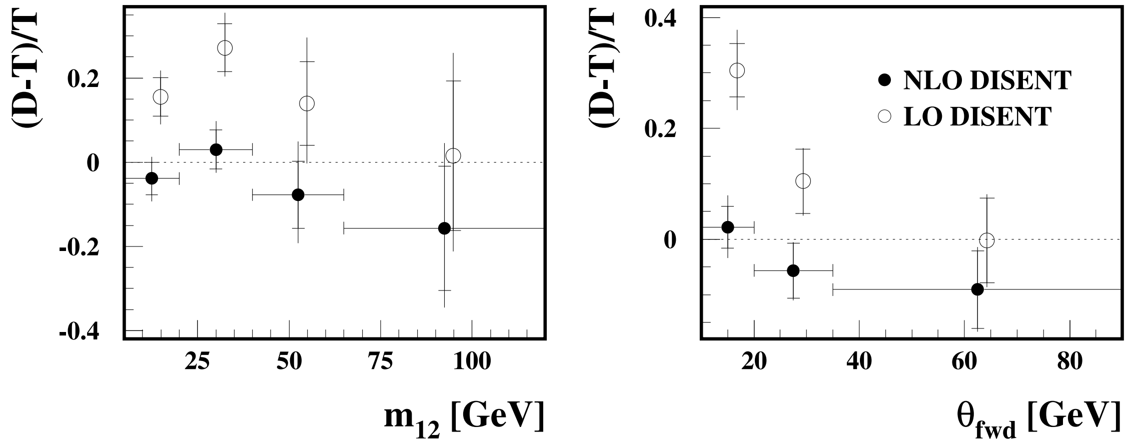

Figure 7.9: *Relative deviations of the NC data from the pQCD predictions in NLO and LO as calculated with DISENT. The renormalization scale is Q.*

Results for $\mathbf{Q^2 > 5\ 000\ GeV^2}$

Charged current and NC dijet distributions are also measured for a subsample of the DIS selection defined by the additional requirement $Q^2 > 5\ 000\ \mathrm{GeV}^2$. The CC subsample contains 71, the NC subsample 300 DIS events. After the jet cuts 17 CC and 91 NC dijet events remain.[4]

As discussed in section 2.3, Z^0 effects in NC processes start to become sizable in this kinematic region. The effects are largely reduced by the normalization of the dijet cross section to the total DIS cross section. Lacking a reliable NLO prediction that takes Z^0 exchange into account, the remaining effects are estimated with ARIADNE. The effects are below 5% for all dijet distributions considered. The DISENT calculations which do not consider Z^0 effects are corrected correspondingly.

The CC and NC data are compared to the respective NLO calculations of MEPJET and DISENT in figure 7.10. The data are well described by the NLO predictions. This is true for both choices of the renormalization scale Q and $\langle E_{T,Breit} \rangle$. The uncertainty assigned to the NLO calculations is given as the quadratic sum of the uncertainty of the hadronization corrections and the uncertainty related to the choice $\mu_R = Q$. The size of the renormalization scale uncertainty does not significantly depend on Q^2 in this analysis. The MC model RAPGAP describes the data equally well as the NLO calculations.

The results presented in this section show that dijet production in CC and NC interactions at high Q^2 is well described by QCD. No deviations from the standard model are observed. These results complement recent measurements of the *inclusive* CC and NC cross sections at high Q^2 at HERA [2, 3].

[4] Note that the dijet distributions are now normalized to the total DIS cross section for $Q^2 > 5\ 000\ \mathrm{GeV}^2$ and $0.03 < y < 0.85$.

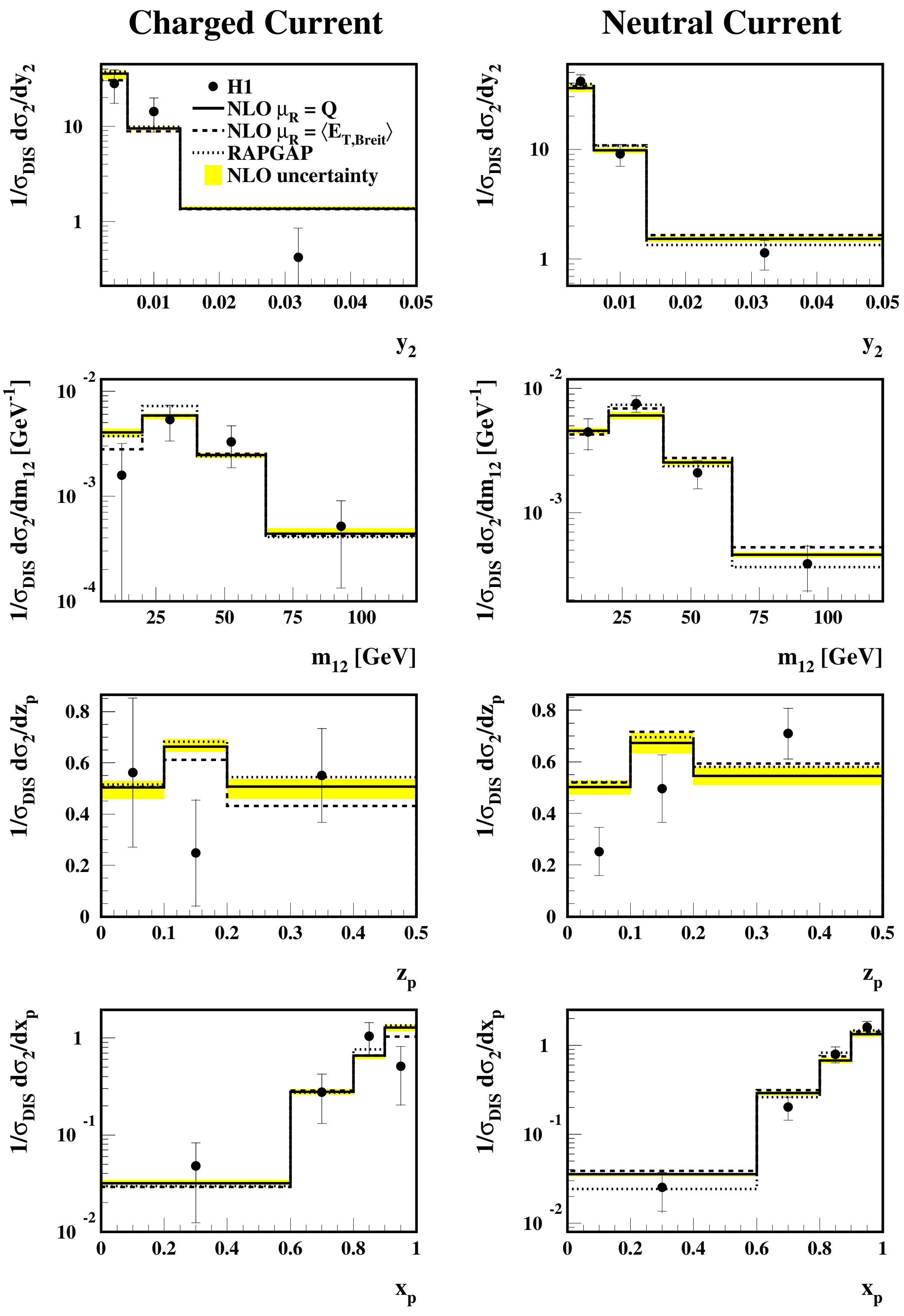

Figure 7.10: *CC (left column) and NC (right column) dijet distributions for* $Q^2 > 5\,000$ *GeV*^{2}*. The perturbative QCD calculations are corrected for hadronization effects. The shaded areas reflect the error due to the uncertainty of the hadronization corrections and a variation of the renormalization scale* Q *from* $Q/2$ *to* $2Q$*. Also shown are the NLO calculations choosing* $\langle E_{T,Breit}\rangle$ *as renormalization scale, and the predictions of RAPGAP.*

7.3 NC Jet Production at Highest $\mathbf{Q^2}$

In recent years the kinematic region of very high Q^2 has attracted some attention. In [66] an excess of NC and CC DIS events over the standard model expectation at $Q^2 > 15\ 000\ \mathrm{GeV}^2$ was reported. The analysis is based on the 1994–1996 data. Including the recent data the excess could not yet be confirmed. The analysis is essentially inclusive, i.e. the characteristics of the hadronic final state are not studied in detail. It is therefore important to investigate if the hadronic final state in this kinematic region shows any anomalies.

In particular no explicit measurement of jet production beyond $Q^2 > 10\ 000\ \mathrm{GeV}^2$ yet exists. However, the 17 CC DIS events selected at $Q^2 > 10\ 000\ \mathrm{GeV}^2$ in the present analysis do not allow the study of CC jet production in this kinematic region with meaningful precision. In contrast, the larger NC e^+p cross section makes possible the measurement of differential jet distributions at these highest scales so far observed in DIS experiments.

In order to increase the number of NC events at the highest Q^2, the jet selection requirement is loosened to $y_2 > 0.001$. This yields a sample of 3 079 dijet events for the DIS event selection defined in section 4.4. At $Q^2 > 10\ 000\ \mathrm{GeV}^2$ 24 dijet events are selected. This almost doubles the number of events with respect to $y_2 > 0.002$. From the discussion in section 5.3 it follows that the dijet sample receives a relatively large contribution of events with very low transverse jet energies in the Breit frame. This makes the comparison of the measured data with NLO calculations a critical test of pQCD at low energy scales. In order to constrain the standard model expectation at lower Q^2 the distributions of y_2, m_{12}, x_p and θ_{fwd} are measured differentially in Q^2. The Q^2-bin boundaries and the numbers of selected DIS and dijet events are listed in table 7.1.

Q^2 intervall	Number of DIS events	Number of dijet events
$640 < Q^2 < 2\ 000\ \mathrm{GeV}^2$	6 918	2 428
$2\ 000 < Q^2 < 5\ 000\ \mathrm{GeV}^2$	1 405	521
$5\ 000 < Q^2 < 10\ 000\ \mathrm{GeV}^2$	254	106
$Q^2 > 10\ 000\ \mathrm{GeV}^2$	46	24

Table 7.1: *Intervals in Q^2 and number of NC DIS and dijet events with* $y_2 > 0.001$.

The size of the correction factors for detector effects and QED radiative processes are essentially not affected by the lower y_2-cut. This is demonstrated in figure 7.11 for the y_2 and θ_{fwd} distributions. The mean correction as predicted by ARIADNE and LEPTO is typically smaller than 15%. A clear trend towards smaller corrections with increasing Q^2 is observed. The model differences are generally below 10%, independent of Q^2 (shaded areas). The same is true for the m_{12} and x_p distributions (not shown). Note that except for the y_2 distribution the binning of the jet distributions is unchanged.

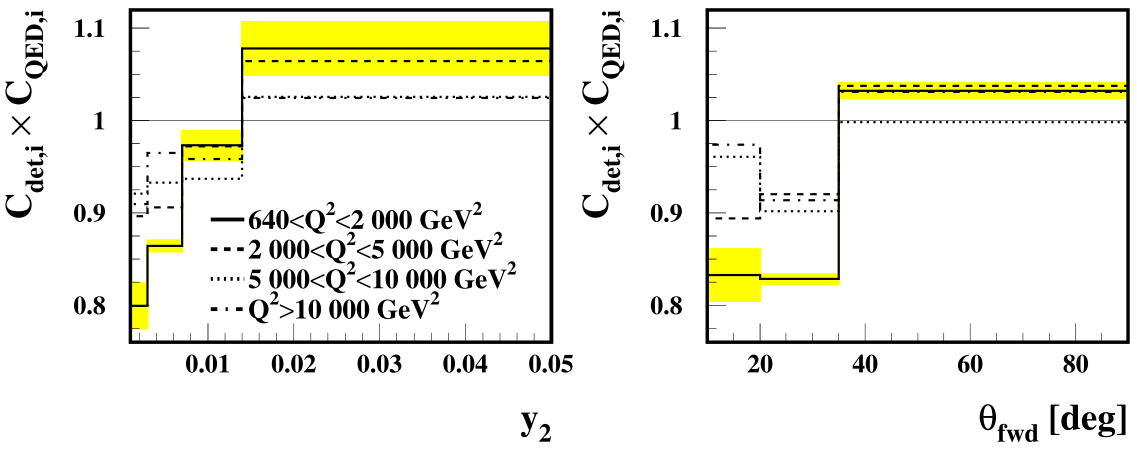

Figure 7.11: *The mean of the combined detector and QED radiation correction factors from ARIADNE and LEPTO for the four Q^2 ranges and $y_2 > 0.001$. The shaded areas indicate the difference between the two models for the lowest Q^2 interval.*

The hadronization corrections for the four Q^2 intervals are shown in figure 7.12 for the m_{12} and x_p distributions. The corrections, given as the mean of the predictions of ARIADNE and HERWIG, are again below 15% on average. A significant Q^2 dependence of the hadronization corrections is not observed. This generally depends on the jet algorithm and on the dijet selection requirement. The (modified) Durham algorithm is known to lead to a weak Q^2 dependence of the hadronization corrections [60]. The differences between the predictions of ARIADNE and HERWIG can become markedly large at low invariant dijet masses and high x_p. This is expected from the events with low transverse jet energies in the Breit frame which are mostly located in these regions.

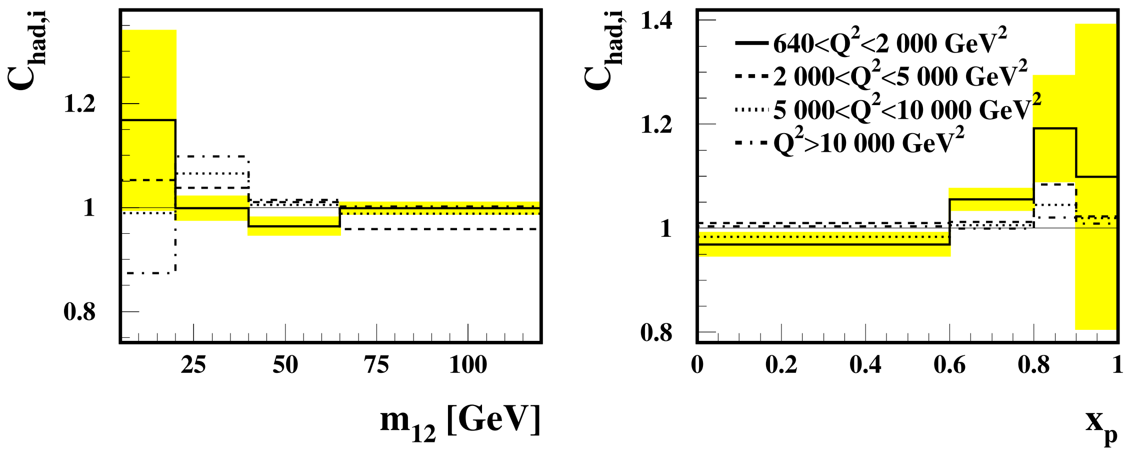

Figure 7.12: *The mean of the hadronization correction factors from ARIADNE and HERWIG for four Q^2 ranges and $y_2 > 0.001$. The shaded areas indicate the difference between the two models for the lowest Q^2 interval.*

The pQCD calculations in NLO are performed with the DISENT program as described in the previous section. They are always corrected for hadronization effects and the effect of Z^0 exchange for $Q^2 > 5\ 000$ GeV^2. The renormalization scale uncertainty is estimated to be 5% on average. The model uncertainty of the hadronization corrections and the renormalization scale uncertainty is added in quadrature to give the total uncertainty of the NLO calculation.

The measured distributions of $y_2, m_{12}, \theta_{fwd}$ and x_p are presented in figures 7.13 and 7.14 for the four Q^2 intervals. The y_2 distribution shows a weak Q^2 dependence with larger mean values for increasing Q^2. The Q^2 dependence of the m_{12} distribution is stronger with a trend towards higher masses with increasing Q^2. This is essentially a phase space effect as can be seen from the superimposed phase space calculation given by DISENT. The θ_{fwd} distribution is strongly increasing at small polar angles. By definition the x_p distribution becomes more peaked at high values with increasing Q^2 (cf. equation 5.5).

The NLO predictions provide a good description of the data over the entire Q^2 range and in particular for $Q^2 > 10\ 000$ GeV^2. The agreement is mostly better than 10%. Note that the systematic error of the measurement is ≈5% on average. The good description of the data by the perturbative QCD prediction is in particular remarkable as low energy jets significantly contribute to the dijet sample.

Also shown are the corresponding leading order calculations (only for y_2 and m_{12}). They are typically 30% lower than the NLO calculations and fail to describe the data. This demonstrates the sensitivity of the distributions to the NLO matrix elements. The phase space calculation predicts a much less steeply falling y_2 spectrum and a rather flat m_{12} distribution. It drastically differs from the data. The MC models ARIADNE and RAPGAP also provide a reasonable description of the data for all Q^2 ranges (only shown for θ_{fwd} and x_p).

Concluding, jet production at $Q^2 > 10\ 000$ GeV^2 is accurately described by the standard model expectation. This conclusion is justified by the small experimental uncertainties and the small corrections applied to the data and the NLO calculations at high Q^2. Precision tests of QCD in this kinematic region are, however, only possible with the high luminosities expected after the HERA 2000/2001 upgrade.

7.4 Comparison of CC and NC Dijet Data

The conclusions derived from the measured data in the previous sections were essentially based on comparisons with model predictions or NLO calculations. In this section the CC and NC data presented in sections 7.1 and 7.2 are compared directly. Naively one expects that QCD processes should proceed largely independently of the underlying electroweak scattering process. Thus the (normalized) CC and NC dijet distributions should be essentially identical.

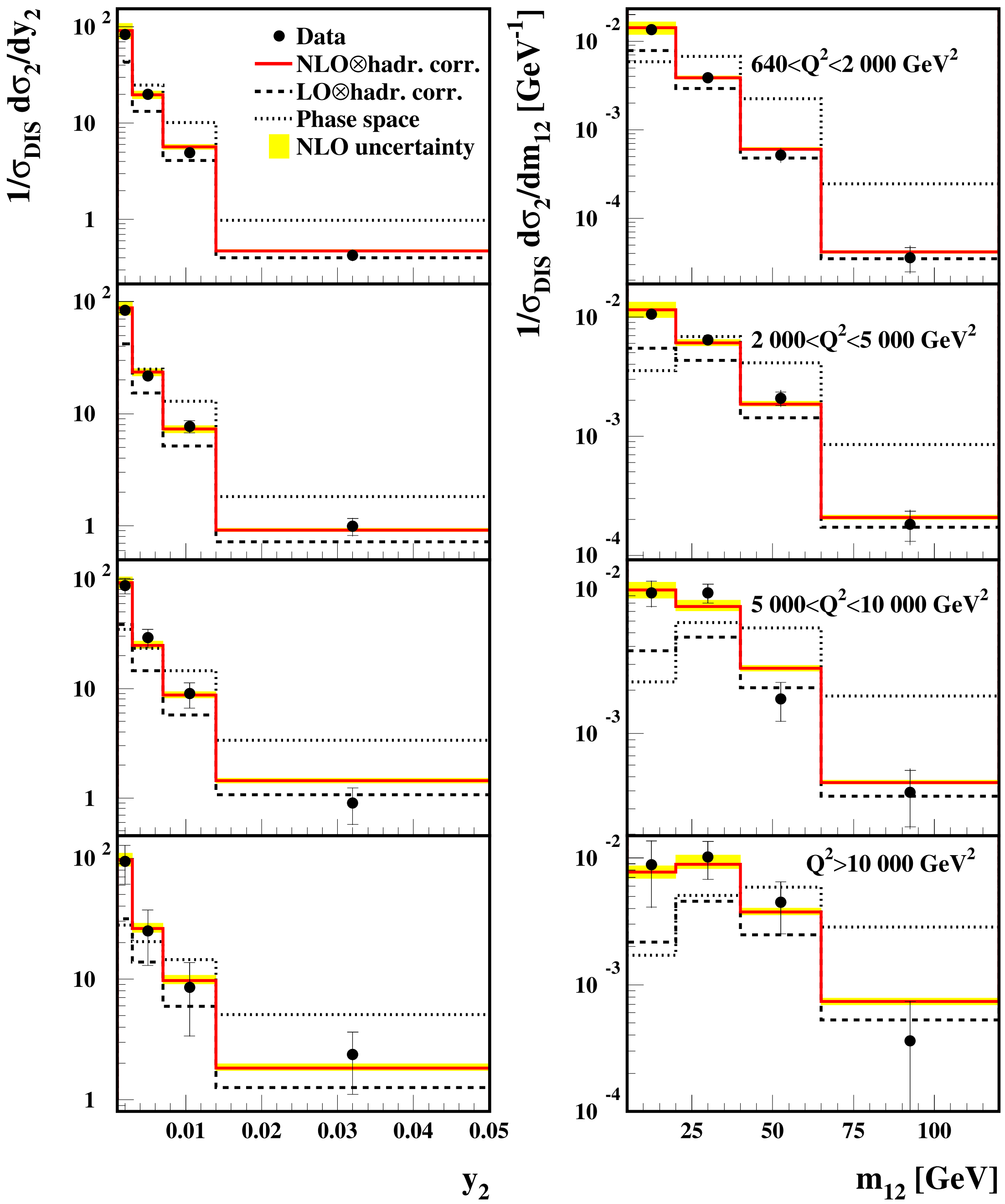

Figure 7.13: *Jet distributions as a function of Q^2 for NC events selected with $y_2 > 0.001$. The NLO and LO pQCD calculations are corrected for hadronization effects and Z^0 exchange. The shaded areas reflect the error due to the uncertainty of the hadronization corrections and a variation of the renormalization scale Q from $Q/2$ to $2Q$. Also shown is a pure phase space calculation. Note, that the last m_{12} bin for $Q^2 > 10\ 000\ GeV^2$ contains only one event.*

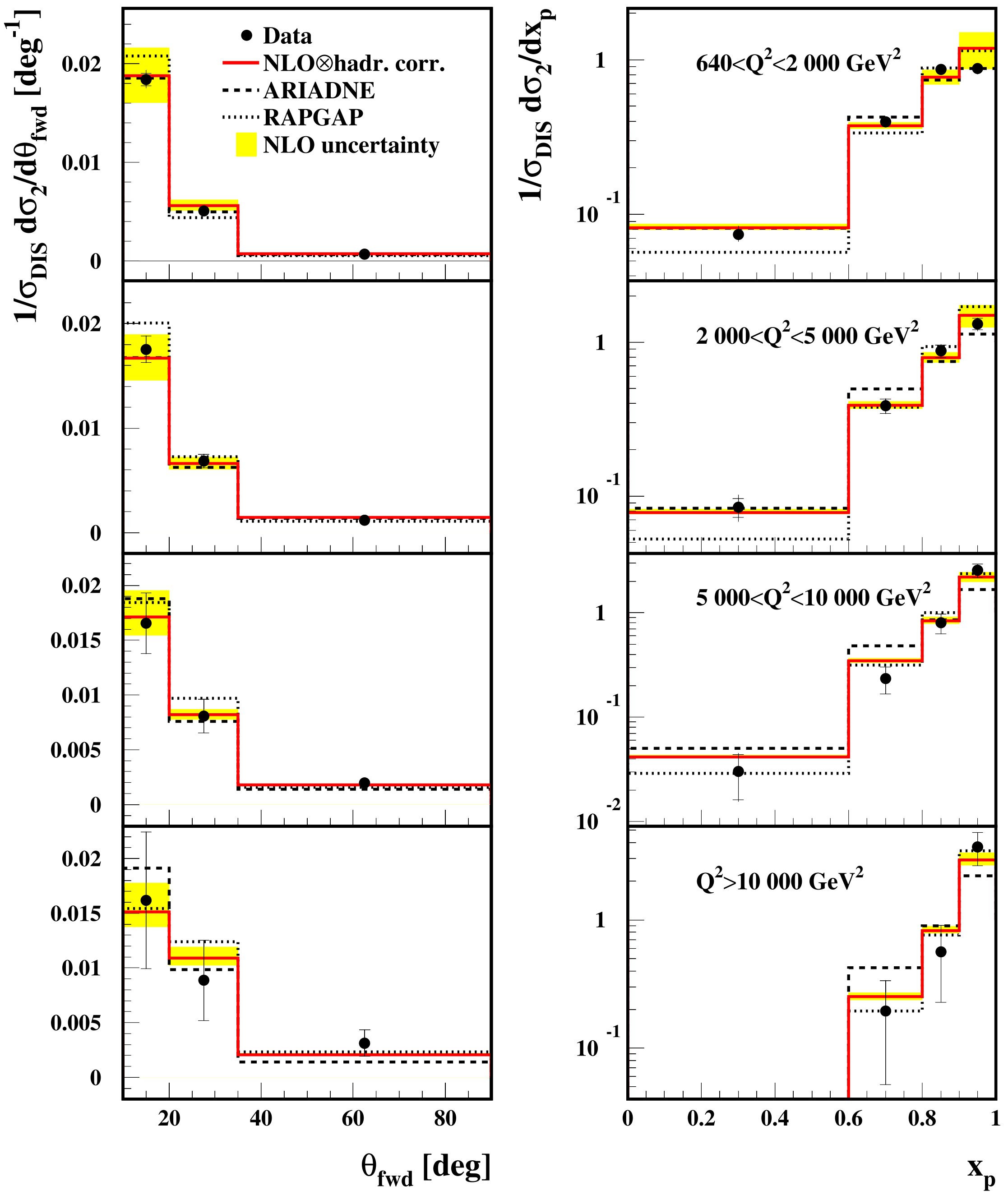

Figure 7.14: *Jet distributions as a function of Q^2 for NC events selected with $y_2 > 0.001$. The NLO pQCD calculations are corrected for hadronization effects. The shaded areas reflect the error due to the uncertainty of the hadronization corrections and a variation of the renormalization scale Q from $Q/2$ to $2Q$. Also shown are the predictions of ARIADNE and RAPGAP on hadron level.*

Effects which are expected to result in differences between the hadronic final states in CC and NC interactions are:

- the different couplings and propagators of the respective bosons in CC and NC interactions. The flattened Q^2 dependence of the CC cross section leads to a more forward shifted angular distribution of the scattered neutrino and thus to a different average orientation of the hadronic final state compared to NC interactions;
- the different fragmentation properties of e.g. the u- and the c-quark,
- the different fraction of gluon-induced events in CC and NC processes;
- helicity effects.

In the following a model independent technique is presented which strongly reduces these effects. This makes possible a direct data comparison which mainly probes the QCD dynamics of the CC and NC interactions.

Reweighting technique

Figure 7.15 shows the ratio of the NC and CC m_{12} and x_p distributions as predicted by ARIADNE,RAPGAP and LEPTO. For the m_{12} distribution the ratio strongly deviates from unity. Effects as large as $\approx$70% are observed. Except for LEPTO, the x_p distribution in contrast appears to be less sensitive to the effects described above. The differences are on average 15%. This is mainly due to the direct Q^2 dependence of the x_p variable in which kinematic effects are expected to largely cancel at high Q^2 (cf. equation 5.5).

The differences are now strongly reduced by reweighting the NC events to reproduce the inclusive CC cross section. After the reweighting the NC and CC kinematic

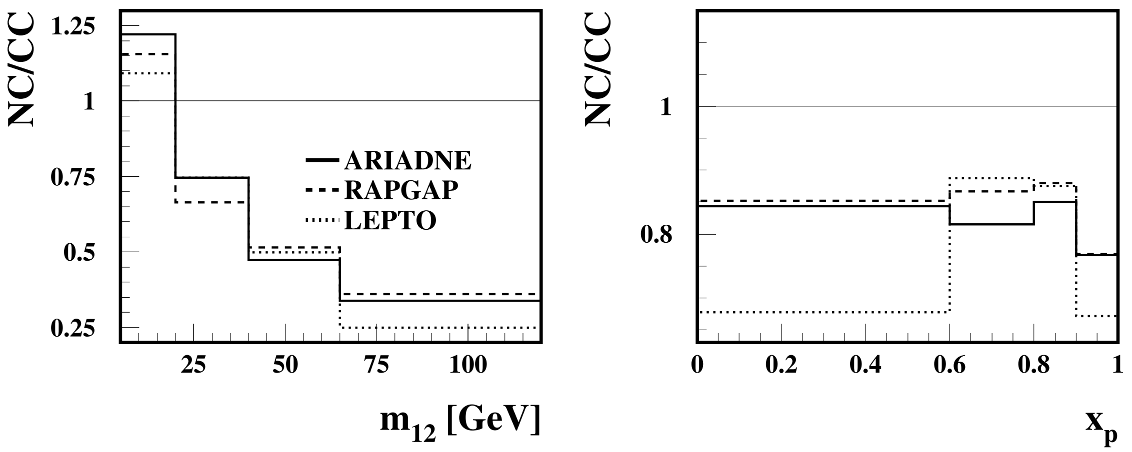

Figure 7.15: *Ratio of simulated NC and CC dijet distributions as predicted by ARIADNE, RAPGAP and LEPTO.*

distributions agree by definition. The weights are determined as a function of x and Q^2 by

$$w(x, Q^2) \equiv \frac{d^2\sigma_{CC}^{e^+p}}{dxdQ^2} / \frac{d^2\sigma_{NC}^{e^+p}}{dxdQ^2}. \tag{7.1}$$

The respective cross sections are calculated in a x/Q^2-grid with the HERACLES program including QED radiative corrections.[5] The values of x and Q^2 are consistently reconstructed using the hadron method in both CC and NC events. In the presence of photon bremsstrahlung off the incoming positron the centre-of-mass energy is effectively reduced. For the reconstruction of the kinematic variables this is only correctly taken into account by the hadron method. Practically speaking, a NC event in which the incoming positron emits a photon may be reconstructed in the wrong x/Q^2-cell of the cross section grid when using the electron method. Experimentally the electron method is 'blind' for the effects of initial state QED radiation because the photon is mostly lost in the beam pipe.

Note that the reweighting technique only uses as input a set of proton parton densities and the inclusive cross sections calculated out of it. It is thus essentially independent of the modeling of the hadronic final state.

The effect of the reweighting procedure can, however, be tested with MC models. This is shown in figure 7.16 for ARIADNE, RAPGAP and LEPTO. The reweighted NC and the CC m_{12} and x_p distributions mostly agree within 5%. The same results are observed for the other jet variables. Note that the statistical error (not shown) of the MC simulations is on average less than 2%. For LEPTO the reweighting completely fails. The reason is so far unknown. In view of the deficient data description (cf. section 7.1) a technical bug seems likely.

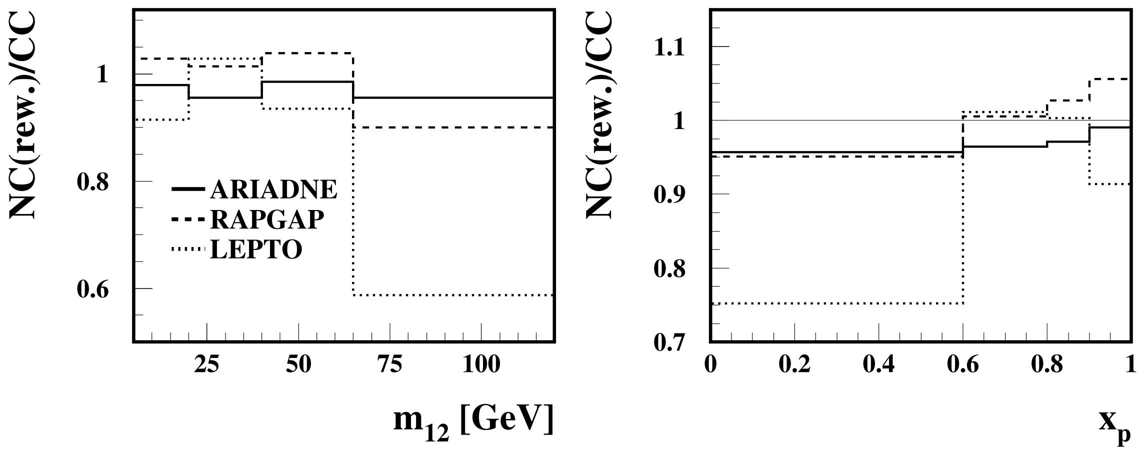

Figure 7.16: *Ratio of the reweighted NC and CC dijet distributions as obtained by ARIADNE, RAPGAP and LEPTO.*

[5] Note that the weights are always smaller than one, because the inclusive NC e^+p cross section is always larger than the CC e^+p cross section (cf. figure 2.3).

The results were cross checked by recalculating the weights with the HECTOR program [24]. HECTOR also includes QED radiative corrections and allows for the determination of the cross sections using both leptonic and hadronic variables. The effect on the reweighted NC dijet distributions is found to be negligible.

Results of the data comparison

The reweighted NC data are corrected for detector effects and QED radiative processes using the reweighted NC Monte-Carlo models in the same way as described in section 6.1. The absolute size of the correction factors is not affected by the reweighting. They turn out to agree with the CC correction factors. A possible effect of the different CC and NC event selection with respect to the kinematic reconstruction method was estimated by repeating the NC event selection with the requirement $P_{T,h} > 25$ GeV. The corrected NC jet distributions change by less than 2%.

The dijet distributions of the reweighted NC data are presented together with the CC and (pure) NC data in figure 7.17. The comparison of the (pure) NC and CC data shows differences of the same size as observed for the MC prediction in figure 7.15.

For all distributions the *reweighted* NC and CC data perfectly agree within the accuracy of the measurement. The data thus support the expectation that at short distances the QCD dynamics of the hadronic final state are largely independently of the underlying electroweak scattering process. It should be noticed, however, that this statement applies, strictly speaking, only to dijet hadronic final states as analysed in this thesis. Quantitative conclusions to what extent this statement is valid are so far prevented by the limited number of CC events available.

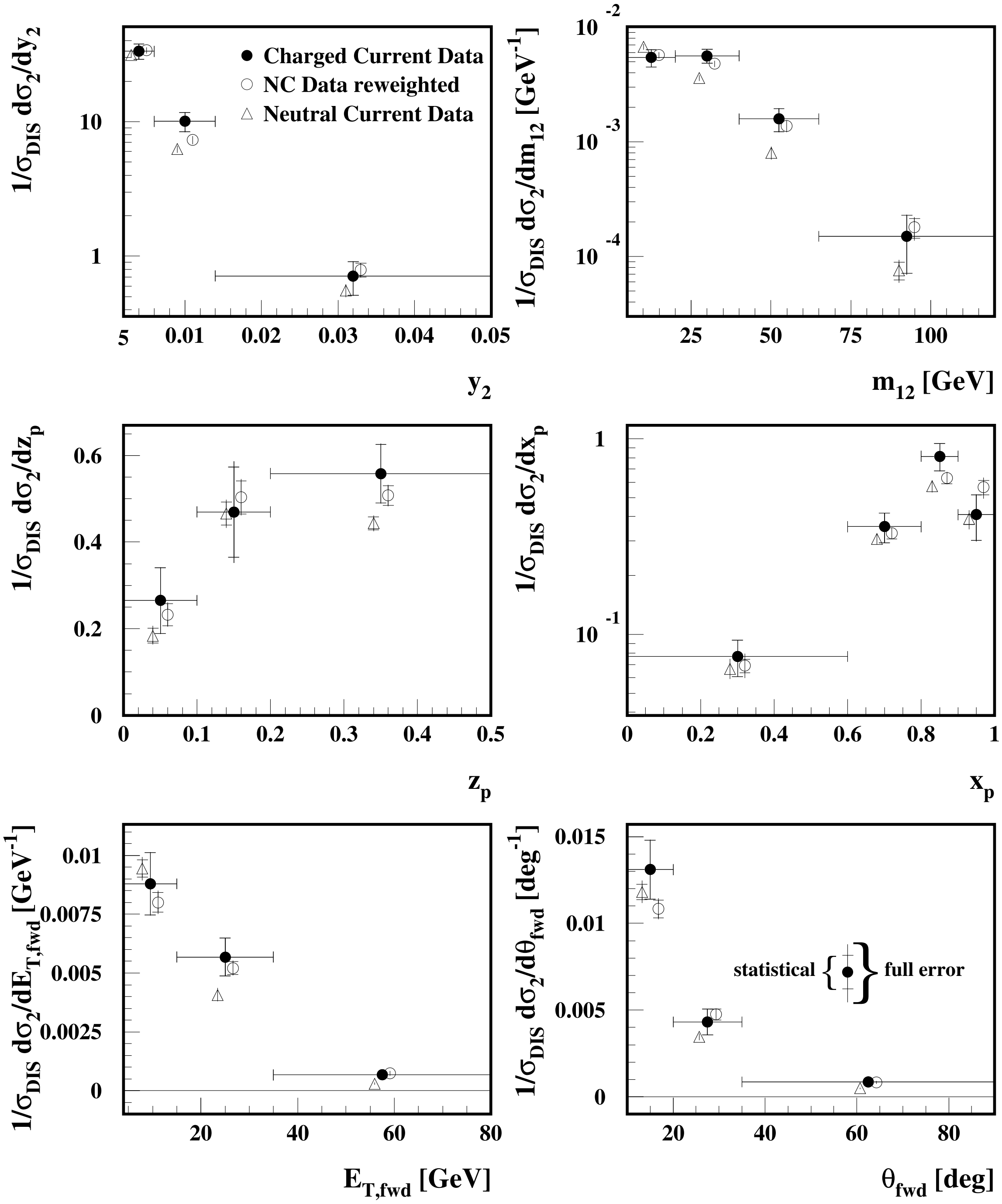

Figure 7.17: *Dijet distributions for CC, NC and reweighted NC data. The CC and NC data points are identical to the ones shown in figure 7.4 and 7.5, respectively. For clarity, the NC and reweighted NC data points have been shifted horizontally.*

Summary

In this thesis an analysis of dijet production in deep-inelastic positron-proton scattering at HERA is presented. The analysis is based on 460 charged current and 8 600 neutral current events with a virtuality of the exchanged W^+ and γ/Z^0 bosons ranging from 640 to 35 000 GeV^2. Jets are reconstructed in the laboratory frame with a modified version of the Durham algorithm. Dijet analyses are hence extended into the kinematic region of very high boson virtualities, Q^2, where so far only inclusive cross section measurements have been made.

Differential CC dijet distributions have been measured for the first time. Pronounced CC dijet structures with invariant masses up to 80 GeV are observed. The measurement of various dijet distributions is found to be in agreement with perturbative calculations in $\mathcal{O}(\alpha_s^2)$. The existence of dijet events in CC interactions is clearly established. The NLO calculations suggest that both quark- and gluon-induced processes are needed to give a consistent description of the CC dijet data.

Dijet production in CC and NC events is also compared directly with essentially no dependence on any model assumptions. The standard model expectation that QCD processes proceed largely independently from the electroweak scattering vertex is confirmed.

Neutral current jet production is in addition analysed for $Q^2 > 10\ 000$ GeV^2, a kinematic region where deviations from the standard model have been reported [66]. The standard model prediction is constrained at lower Q^2 with a high statistics NC data sample obtained with a loosened dijet selection criterion. Neutral current jet production for $Q^2 > 10\ 000$ GeV^2 is found to be entirely consistent with the standard model expectation.

Generally, the full dijet sample analysed differentially in Q^2 is well described by the next-to-leading order calculations. This is in particular remarkable as low energy jets significantly contribute to this dijet sample. Given the small total experimental uncertainty and the small corrections applied to the theoretical predictions the presented NC measurements have established perturbative QCD as a reliable prediction at the highest scales. This may serve as a basis for the interpretation of future high precision measurements at HERA.

Appendix A

Tables of Results

The following tables list the results of the measurements presented in sections 7.1, 7.2 and 7.3. All errors are given in per cent. The systematic errors have been equalized. The largest deviation assigned to an individual systematic uncertainty in a given bin is taken conservatively as the systematic error for that bin.

$\mathbf{y_2}$	$\frac{1}{\sigma_{DIS}}\frac{d\sigma}{dy_2}$	δ_{stat}	δ_{sys}	*Hadronic energy scale*	*Track momenta*	*Correction uncertainty*
0.002 – 0.006	33	± 13	±2	±2	±0	±1
0.006 – 0.014	10	± 17	±2	±1	±1	±2
0.014 – 0.05	0.7	± 28	±3	±3	±1	±1
$\mathbf{m_{12}}$ [GeV]	$\frac{1}{\sigma_{DIS}}\frac{d\sigma}{dm_{12}}$ [GeV^{-1}]	δ_{stat}	δ_{sys}	*Hadronic energy scale*	*Track momenta*	*Correction uncertainty*
5 – 20	0.005	± 17	±4	±2	±0	±3
20 – 40	0.006	± 14	±2	±1	±1	± 2
40 – 65	0.0016	± 23	±5	±5	±1	± 2
65 – 120	0.0002	± 53	±12	±11	±1	± 4
$\mathbf{z_p}$	$\frac{1}{\sigma_{DIS}}\frac{d\sigma}{dz_p}$	δ_{stat}	δ_{sys}	*Hadronic energy scale*	*Track momenta*	*Correction uncertainty*
0. – 0.1	0.27	± 29	±5	±4	±1	± 1
0.1 – 0.2	0.47	± 22	±11	±1	±1	± 11
0.2 – 0.5	0.56	± 12	±3	±2	±0	± 2
$\mathbf{x_p}$	$\frac{1}{\sigma_{DIS}}\frac{d\sigma}{dx_p}$	δ_{stat}	δ_{sys}	*Hadronic energy scale*	*Track momenta*	*Correction uncertainty*
0. – 0.6	0.077	± 21	±2	±0	±1	± 2
0.6 – 0.8	0.36	± 17	±3	±2	±0	± 2
0.8 – 0.9	0.81	± 16	±3	±1	±1	± 2
0.9 – 1.0	0.41	± 26	±6	±6	±1	± 2

Table A.1: *Normalized dijet cross sections for CC events selected with* $P_T > 25$ *GeV and* $0.03 < y < 0.85$. *The jets are reconstructed with the modified Durham algorithm. The dijet events satisfy the cuts* $y_2 > 0.002$ *and* $10° < \theta_{jet} < 140°$.

$\mathbf{E_{T,fwd}}$ [GeV]	$\frac{1}{\sigma_{DIS}}\frac{d\sigma}{dE_{T,fwd}}$ [GeV^{-1}]	δ_{stat}	δ_{sys}	*Hadronic energy scale*	*Track momenta*	*Correction uncertainty*
4 –15	0.0088	± 15	±2	±0	±0	± 2
15 – 35	0.0057	± 14	±2	±1	±1	± 1
35 – 80	0.00067	± 26	±7	±7	±1	± 1
$\mathbf{E_{T,bwd}}$ [GeV]	$\frac{1}{\sigma_{DIS}}\frac{d\sigma}{dE_{T,bwd}}$ [GeV^{-1}]	δ_{stat}	δ_{sys}	*Hadronic energy scale*	*Track momenta*	*Correction uncertainty*
4 – 15	0.0048	± 20	±1	±1	±0	± 1
15 – 35	0.0067	± 13	±2	±1	±1	± 1
35 – 80	0.0011	± 21	±7	±7	±1	± 0
$\theta_{\mathbf{fwd}}$ [deg]	$\frac{1}{\sigma_{DIS}}\frac{d\sigma}{d\theta_{fwd}}$ [deg^{-1}]	δ_{stat}	δ_{sys}	*Hadronic energy scale*	*Track momenta*	*Correction uncertainty*
10 – 20	0.013	± 13	±2	±2	±0	± 0
20 – 35	0.0043	± 17	±2	±2	±1	± 0
35 – 90	0.00086	± 23	±3	±3	±1	± 1
$\theta_{\mathbf{bwd}}$ [deg]	$\frac{1}{\sigma_{DIS}}\frac{d\sigma}{d\theta_{bwd}}$ [deg^{-1}]	δ_{stat}	δ_{sys}	*Hadronic energy scale*	*Track momenta*	*Correction uncertainty*
10 – 20	0.0039	± 23	±4	±3	±1	± 3
20 – 40	0.0046	± 15	±2	±2	±1	± 1
40 – 70	0.0021	± 18	±2	±1	±1	± 1
70 – 140	0.0005	± 25	±4	±3	±1	± 2

Table A.2: *Normalized dijet cross sections for CC events selected with $P_T > 25$ GeV and $0.03 < y < 0.85$. The jets are reconstructed with the modified Durham algorithm. The dijet events satisfy the cuts $y_2 > 0.002$ and $10^\circ < \theta_{jet} < 140^\circ$.*

$\mathbf{y_2}$	$\frac{1}{\sigma_{DIS}}\frac{d\sigma}{dy_2}$	δ_{stat}	δ_{sys}	*Hadronic energy scale*	*Track momenta*	*El. magn. energy scale*	*Correction uncertainty*
0.002 – 0.006	31.4	± 3.5	±3.1	±1.0	±0.7	±0.8	± 2.8
0.006 – 0.014	6.3	± 5.4	±2.8	±2.7	±0.3	±0.6	± 0.3
0.014 – 0.05	0.56	± 8.9	±6.1	±5.9	±1.3	±0.9	± 0.3
$\mathbf{m_{12}}$ [GeV]	$\frac{1}{\sigma_{DIS}}\frac{d\sigma}{dm_{12}}$ [GeV^{-1}]	δ_{stat}	δ_{sys}	*Hadronic energy scale*	*Track momenta*	*El. magn. energy scale*	*Correction uncertainty*
5 – 20	0.0067	± 4.0	±3.9	±1.5	±0.2	±0.6	± 3.5
20 – 40	0.0036	± 4.5	±3.9	±3.8	±1.1	±0.2	± 0.1
40 – 65	0.0008	± 8.7	±10	±9.5	±1.4	±0.7	± 1.7
65 – 120	0.00008	± 18	±15	±15	±1.2	±0.4	± 2.0
$\mathbf{z_p}$	$\frac{1}{\sigma_{DIS}}\frac{d\sigma}{dz_p}$	δ_{stat}	δ_{sys}	*Hadronic energy scale*	*Track momenta*	*El. magn. energy scale*	*Correction uncertainty*
0. – 0.1	0.18	± 9.4	±7.0	±6.8	±0.8	±0.8	± 1.1
0.1 – 0.2	0.47	± 5.7	±4.1	±1.7	±0.5	±0.5	± 3.6
0.2 – 0.5	0.44	± 3.4	±2.4	±1.4	±0.7	±0.3	± 1.8
$\mathbf{x_p}$	$\frac{1}{\sigma_{DIS}}\frac{d\sigma}{dx_p}$	δ_{stat}	δ_{sys}	*Hadronic energy scale*	*Track momenta*	*El. magn. energy scale*	*Correction uncertainty*
0. – 0.6	0.066	± 6.2	±10	±9.7	±1.6	±0.8	± 1.0
0.6 – 0.8	0.31	± 4.9	±3.1	±2.5	±0.8	±0.3	± 1.6
0.8 – 0.9	0.57	± 5.0	±4.7	±0.9	±0.5	±0.4	± 4.5
0.9 – 1.0	0.39	± 6.6	±9.0	±6.0	±0.4	±0.4	± 6.7

Table A.3: *Normalized dijet cross sections for NC events selected with* $P_T > 25$ *GeV and* $0.03 < y < 0.85$. *The jets are reconstructed with the modified Durham algorithm. The dijet events satisfy the cuts* $y_2 > 0.002$ *and* $10° < \theta_{jet} < 140°$.

$\mathbf{E_{T,fwd}}$ [GeV]	$\frac{1}{\sigma_{DIS}}\frac{d\sigma}{dE_{T,fwd}}$ [GeV^{-1}]	δ_{stat}	δ_{sys}	*Hadronic energy scale*	*Track momenta*	*El. magn. energy scale*	*Correction uncertainty*
4 – 15	0.0094	± 3.9	±3.7	±2.1	±0.2	±0.8	± 2.9
15 – 35	0.0041	± 4.4	±5.7	±5.6	±1.2	±0.2	± 0.2
35 – 80	0.00029	± 10	±15	±15	±1.3	±1.4	± 0.9
$\mathbf{E_{T,bwd}}$ [GeV]	$\frac{1}{\sigma_{DIS}}\frac{d\sigma}{dE_{T,bwd}}$ [GeV^{-1}]	δ_{stat}	δ_{sys}	*Hadronic energy scale*	*Track momenta*	*El. magn. energy scale*	*Correction uncertainty*
4 – 15	0.0053	± 4.8	±4.6	±4.3	±0.2	±1.5	± 0.6
15 – 35	0.0061	± 3.7	±4.8	±3.9	±1.0	±0.3	± 2.5
35 – 80	0.00042	± 9.1	±15	±15	±1.4	±2.1	± 3.0
$\theta_{\mathbf{fwd}}$ [deg]	$\frac{1}{\sigma_{DIS}}\frac{d\sigma}{d\theta_{fwd}}$ [deg^{-1}]	δ_{stat}	δ_{sys}	*Hadronic energy scale*	*Track momenta*	*El. magn. energy scale*	*Correction uncertainty*
10 – 20	0.0118	± 3.7	±4.2	±2.3	±0.4	±0.1	± 3.5
20 – 35	0.0035	± 5.2	±1.7	±1.0	±1.3	±0.4	± 0.2
35 – 90	0.0005	± 7.7	±3.4	±1.8	±0.8	±2.5	± 1.2
$\theta_{\mathbf{bwd}}$ [deg]	$\frac{1}{\sigma_{DIS}}\frac{d\sigma}{d\theta_{bwd}}$ [deg^{-1}]	δ_{stat}	δ_{sys}	*Hadronic energy scale*	*Track momenta*	*El. magn. energy scale*	*Correction uncertainty*
10 – 20	0.0041	± 5.9	±6.5	±3.2	±0.4	±0.3	± 5.7
20 – 40	0.0039	± 4.3	±2.5	±1.5	±0.8	±0.5	± 1.7
40 – 70	0.0017	± 5.6	±2.1	±1.6	±0.6	±1.2	± 0.2
70 – 140	0.00039	± 7.4	±2.4	±1.1	±0.9	±1.8	± 0.6

Table A.4: *Normalized dijet cross sections for NC events selected with $P_T > 25$ GeV and $0.03 < y < 0.85$. The jets are reconstructed with the modified Durham algorithm. The dijet events satisfy the cuts $y_2 > 0.002$ and $10° < \theta_{jet} < 140°$.*

$Q^2 > 5\,000$ GeV^2						
$\mathbf{y_2}$	$\frac{1}{\sigma_{DIS}}\frac{d\sigma}{dy_2}$	δ_{stat}	δ_{sys}	*Hadronic energy scale*	*Track momenta*	*Correction uncertainty*
0.002 – 0.006	30	± 40	±4	±3	±1	± 3
0.006 – 0.014	14	± 40	±4	±0	±2	± 4
0.014 – 0.05	0.4	±100	±4	±4	±2	± 1
$\mathbf{m_{12}}$ [GeV]	$\frac{1}{\sigma_{DIS}}\frac{d\sigma}{dm_{12}}$ [GeV^{-1}]	δ_{stat}	δ_{sys}	*Hadronic energy scale*	*Track momenta*	*Correction uncertainty*
5 – 20	0.002	±100	±11	±11	±1	± 1
20 – 40	0.005	± 38	±4	±4	±1	± 0
40 – 65	0.003	± 43	±4	±4	±1	± 1
65 – 120	0.0005	± 74	±7	±4	±1	± 3
$\mathbf{z_p}$	$\frac{1}{\sigma_{DIS}}\frac{d\sigma}{dz_p}$	δ_{stat}	δ_{sys}	*Hadronic energy scale*	*Track momenta*	*Correction uncertainty*
0. – 0.1	0.6	± 52	±4	±4	±2	± 0
0.1 – 0.2	0.2	± 83	±16	±1	±2	± 16
0.2 – 0.5	0.6	± 33	±3	±2	±1	± 2
$\mathbf{x_p}$	$\frac{1}{\sigma_{DIS}}\frac{d\sigma}{dx_p}$	δ_{stat}	δ_{sys}	*Hadronic energy scale*	*Track momenta*	*Correction uncertainty*
0. – 0.6	0.05	± 74	±9	±9	±2	± 3
0.6 – 0.8	0.3	± 52.4	±4	±3	±1	± 2
0.8 – 0.9	1.0	± 38	±4	±4	±1	± 1
0.9 – 1.0	0.5	± 60	±6	±6	±1	± 2

Table A.5: *Normalized dijet cross sections for CC events selected with* $Q^2 > 5\,000$ *GeV*^{2} *and* $0.03 < y < 0.85$. *The jets are reconstructed with the modified Durham algorithm. The dijet events satisfy the cuts* $y_2 > 0.002$ *and* $10^\circ < \theta_{jet} < 140^\circ$.

$Q^2 > 5\ 000\ \mathrm{GeV}^2$							
$\mathbf{y_2}$	$\frac{1}{\sigma_{DIS}}\frac{d\sigma}{dy_2}$	δ_{stat}	δ_{sys}	*Hadronic energy scale*	*Track momenta*	*El. magn. energy scale*	*Correction uncertainty*
0.002 – 0.006	41	± 15	±1	±1	±0	±0	± 1
0.006 – 0.014	9.0	± 22	±3	±0	±0	±1	± 3
0.014 – 0.05	1.1	± 30	±5	±4	±1	±1	± 2
$\mathbf{m_{12}}$ [GeV]	$\frac{1}{\sigma_{DIS}}\frac{d\sigma}{dm_{12}}$ [GeV^{-1}]	δ_{stat}	δ_{sys}	*Hadronic energy scale*	*Track momenta*	*El. magn. energy scale*	*Correction uncertainty*
5 – 20	0.0045	± 28	±8	±8	±1	±1	± 1
20 – 40	0.0076	± 15	±2	±0	±0	±1	± 2
40 – 65	0.002	± 26	±2	±2	±0	±0	± 1.9
65 – 120	0.0004	± 39	±14	±14	±2	±1	± 3
$\mathbf{z_p}$	$\frac{1}{\sigma_{DIS}}\frac{d\sigma}{dz_p}$	δ_{stat}	δ_{sys}	*Hadronic energy scale*	*Track momenta*	*El. magn. energy scale*	*Correction uncertainty*
0. – 0.1	0.25	± 37	±5	±4	±0	±1	± 3
0.1 – 0.2	0.50	± 26	±2	±1	±1	±0	± 2
0.2 – 0.5	0.71	± 14	±3	±1	±1	±1	± 2
$\mathbf{x_p}$	$\frac{1}{\sigma_{DIS}}\frac{d\sigma}{dx_p}$	δ_{stat}	δ_{sys}	*Hadronic energy scale*	*Track momenta*	*El. magn. energy scale*	*Correction uncertainty*
0. – 0.6	0.03	± 46	±19	±18	±1	±2	± 2
0.6 – 0.8	0.20	± 29	±3	±2	±1	±0	± 1
0.8 – 0.9	0.79	± 20	±3	±1	±1	±1	± 2
0.9 – 1.0	1.6	± 16	±4	±4	±0	±0	± 1

Table A.6: *Normalized dijet cross sections for NC events selected with $Q^2 > 5\ 000\ GeV^2$ and $0.03 < y < 0.85$. The jets are reconstructed with the modified Durham algorithm. The dijet events satisfy the cuts $y_2 > 0.002$ and $10° < \theta_{jet} < 140°$.*

$640 < Q^2 < 2\ 000$ GeV^2							
$\mathbf{y_2}$	$\frac{1}{\sigma_{DIS}}\frac{d\sigma}{dy_2}$	δ_{stat}	δ_{sys}	*Hadronic energy scale*	*Track momenta*	*El. magn. energy scale*	*Correction uncertainty*
0.001 – 0.003	83.6	± 3.5	±3.3	±1.0	±0.4	±0.5	± 3.1
0.003 – 0.007	19.9	± 4.8	±1.5	±0.6	±0.7	±0.7	± 0.7
0.007 – 0.014	4.9	± 7.3	±5.5	±5.0	±0.6	±1.0	± 1.6
0.014 – 0.05	0.42	± 11.6	±7.1	±6.4	±1.5	±0.8	± 2.7
$\mathbf{m_{12}}$ [GeV]	$\frac{1}{\sigma_{DIS}}\frac{d\sigma}{dm_{12}}$ [GeV^{-1}]	δ_{stat}	δ_{sys}	*Hadronic energy scale*	*Track momenta*	*El. magn. energy scale*	*Correction uncertainty*
5 – 20	0.014	± 3.3	±3.9	±0.7	±0.3	±0.3	± 3.8
20 – 40	0.0039	± 4.9	±5.4	±5.1	±1.0	±0.3	± 1.6
40 – 65	0.00052	± 13	±14	±13	±1.9	±0.6	± 5.0
65 – 120	0.00004	± 31	±18	±15	±0.0	±2.7	± 8.8
$\theta_{\mathbf{fwd}}$ [deg]	$\frac{1}{\sigma_{DIS}}\frac{d\sigma}{d\theta_{fwd}}$ [deg^{-1}]	δ_{stat}	δ_{sys}	*Hadronic energy scale*	*Track momenta*	*El. magn. energy scale*	*Correction uncertainty*
10 – 20	0.018	± 3.4	±3.8	±1.7	±0.1	±0.2	± 3.4
20 – 35	0.0051	± 4.8	±1.8	±0.7	±1.5	±0.5	± 0.6
35 – 90	0.00071	± 7.0	±3.0	±1.2	±1.1	±2.4	± 0.8
$\mathbf{x_p}$	$\frac{1}{\sigma_{DIS}}\frac{d\sigma}{dx_p}$	δ_{stat}	δ_{sys}	*Hadronic energy scale*	*Track momenta*	*El. magn. energy scale*	*Correction uncertainty*
0. – 0.6	0.074	± 6.7	±9.8	±9.2	±1.4	±1.3	± 2.8
0.6 – 0.8	0.39	± 4.9	±4.1	±3.0	±0.7	±0.5	± 2.7
0.8 – 0.9	0.87	± 4.6	±5.8	±1.9	±0.6	±0.4	± 5.3
0.9 – 1.0	0.88	± 4.9	±6.4	±4.0	±0.1	±0.4	± 5.0

Table A.7: *Normalized dijet cross sections for NC events selected with* $640 < Q^2 < 2\ 000\ GeV^2$ *and* $0.03 < y < 0.85$. *The jets are reconstructed with the modified Durham algorithm. The dijet events satisfy the cuts* $y_2 > 0.001$ *and* $10° < \theta_{jet} < 140°$.

$2\,000 < Q^2 < 5\,000$ GeV^2							
$\mathbf{y_2}$	$\frac{1}{\sigma_{DIS}}\frac{d\sigma}{dy_2}$	δ_{stat}	δ_{sys}	*Hadronic energy scale*	*Track momenta*	*El. magn. energy scale*	*Correction uncertainty*
0.001 – 0.003	84	± 7.6	±2.9	±1.0	±0.3	±0.2	± 2.7
0.003 – 0.007	22	± 10	±2.4	±0.8	±0.3	±0.2	± 2.2
0.007 – 0.014	7.7	± 13	±3.1	±2.4	±0.7	±0.8	± 1.4
0.014 – 0.05	1.0	± 17	±7.9	±5.8	±1.0	±1.0	± 5.1
$\mathbf{m_{12}}$ [GeV]	$\frac{1}{\sigma_{DIS}}\frac{d\sigma}{dm_{12}}$ [GeV^{-1}]	δ_{stat}	δ_{sys}	*Hadronic energy scale*	*Track momenta*	*El. magn. energy scale*	*Correction uncertainty*
5 – 20	0.011	± 7.8	±3.0	±2.6	±0.2	±0.2	± 1.3
20 – 40	0.0064	± 8.3	±2.8	±1.9	±0.4	±0.2	± 2.0
40 – 65	0.0021	± 13	±10	±9.3	±1.6	±0.9	± 1.2
65 – 120	0.00018	± 28	±17	±17	±1.9	±1.6	± 1.1
$\boldsymbol{\theta_{fwd}}$ [deg]	$\frac{1}{\sigma_{DIS}}\frac{d\sigma}{d\theta_{fwd}}$ [deg^{-1}]	δ_{stat}	δ_{sys}	*Hadronic energy scale*	*Track momenta*	*El. magn. energy scale*	*Correction uncertainty*
10 – 20	0.018	± 7.2	±2.2	±1.8	±0.2	±0.4	± 1.1
20 – 35	0.00685	± 9.5	±3.4	±1.5	±0.5	±0.5	± 2.9
35 – 90	0.0012	± 12	±2.7	±1.3	±0.9	±1.3	± 1.7
$\mathbf{x_p}$	$\frac{1}{\sigma_{DIS}}\frac{d\sigma}{dx_p}$	δ_{stat}	δ_{sys}	*Hadronic energy scale*	*Track momenta*	*El. magn. energy scale*	*Correction uncertainty*
0. – 0.6	0.084	± 14	15	±13	±1.6	±1.6	± 4.9
0.6 – 0.8	0.39	± 11	±3.5	±2.4	±0.7	±0.3	± 2.3
0.8 – 0.9	0.87	± 10	±4.3	±2.6	±0.2	±0.2	± 3.6
0.9 – 1.0	1.3	± 8.7	±4.5	±4.2	±0.2	±0.3	± 1.3

Table A.8: *Normalized dijet cross sections for NC events selected with* $2\,000 < Q^2 < 5\,000$ *GeV*^{2} *and* $0.03 < y < 0.85$. *The jets are reconstructed with the modified Durham algorithm. The dijet events satisfy the cuts* $y_2 > 0.001$ *and* $10° < \theta_{jet} < 140°$.

$5\ 000 < Q^2 < 10\ 000$ GeV^2							
$\mathbf{y_2}$	$\frac{1}{\sigma_{DIS}}\frac{d\sigma}{dy_2}$	δ_{stat}	δ_{sys}	*Hadronic energy scale*	*Track momenta*	*El. magn. energy scale*	*Correction uncertainty*
0.001 – 0.003	88	± 16	±2	±1	±0	±0	± 1
0.003 – 0.007	29	± 19	±2	±0	±1	±1	± 2
0.007 – 0.014	9.0	± 26	±3	±0	±0	±1	± 3
0.014 – 0.05	0.9	± 37	±5	±5	±1	±1	± 2
$\mathbf{m_{12}}$ [GeV]	$\frac{1}{\sigma_{DIS}}\frac{d\sigma}{dm_{12}}$ [GeV^{-1}]	δ_{stat}	δ_{sys}	*Hadronic energy scale*	*Track momenta*	*El. magn. energy scale*	*Correction uncertainty*
5 – 20	0.009	± 20	±6	±6	±0	±1	± 1
20 – 40	0.010	± 15	±3	±1	±0	±1	± 3
40 – 65	0.0017	± 30	±3	±2	±0	±0	± 2
65 – 120	0.0004	± 42	±17	±17	±2	±1	± 2
$\theta_{\mathbf{fwd}}$ [deg]	$\frac{1}{\sigma_{DIS}}\frac{d\sigma}{d\theta_{fwd}}$ [deg^{-1}]	δ_{stat}	δ_{sys}	*Hadronic energy scale*	*Track momenta*	*El. magn. energy scale*	*Correction uncertainty*
10 – 20	0.017	± 17	±3	±3	±0	±0	± 2
20 – 35	0.008	± 19	±3	±1	±1	±1	± 3
35 – 90	0.002	± 20	±2	±1	±0	±2	± 1
$\mathbf{x_p}$	$\frac{1}{\sigma_{DIS}}\frac{d\sigma}{dx_p}$	δ_{stat}	δ_{sys}	*Hadronic energy scale*	*Track momenta*	*El. magn. energy scale*	*Correction uncertainty*
0. – 0.6	0.03	± 46	±18	±18	±1	±1	± 2
0.6 – 0.8	0.24	± 29	±3	±3	±1	±0	± 2
0.8 – 0.9	0.80	± 22	±3	±2	±1	±0	± 2
0.9 – 1.0	2.6	± 15	±4	±3	±0	±0	± 2

Table A.9: *Normalized dijet cross sections for NC events selected with* $5\ 000 < Q^2 < 10\ 000$ *GeV*^{2} *and* $0.03 < y < 0.85$. *The jets are reconstructed with the modified Durham algorithm. The dijet events satisfy the cuts* $y_2 > 0.001$ *and* $10° < \theta_{jet} < 140°$.

$Q^2 > 10\ 000$ GeV^2							
$\mathbf{y_2}$	$\frac{1}{\sigma_{DIS}}\frac{d\sigma}{dy_2}$	δ_{stat}	δ_{sys}	*Hadronic energy scale*	*Track momenta*	*El. magn. energy scale*	*Correction uncertainty*
0.001 – 0.003	95	$\pm$ 36	$\pm$1	$\pm$1	$\pm$1	$\pm$0	$\pm$ 0
0.003 – 0.007	25	$\pm$ 48	$\pm$2	$\pm$0	$\pm$0	$\pm$0	$\pm$ 2
0.007 – 0.014	9	$\pm$ 61	$\pm$2	$\pm$1	$\pm$1	$\pm$0	$\pm$ 2
0.0014 – 0.05	2	$\pm$ 53	$\pm$3	$\pm$2	$\pm$0	$\pm$1	$\pm$ 2
$\mathbf{m_{12}}$ [GeV]	$\frac{1}{\sigma_{DIS}}\frac{d\sigma}{dm_{12}}$ [GeV^{-1}]	δ_{stat}	δ_{sys}	*Hadronic energy scale*	*Track momenta*	*El. magn. energy scale*	*Correction uncertainty*
5 – 20	0.009	$\pm$ 54	$\pm$11	$\pm$10	$\pm$0	$\pm$1	$\pm$ 3
20 – 40	0.010	$\pm$ 33	$\pm$2	$\pm$0	$\pm$0	$\pm$0	$\pm$ 2
40 – 65	0.004	$\pm$ 44	$\pm$2	$\pm$2	$\pm$0	$\pm$0	$\pm$ 1
65 – 120	0.0004	$\pm$100	$\pm$9	$\pm$8	$\pm$1	$\pm$2	$\pm$ 3
$\theta_{\mathbf{fwd}}$ [deg]	$\frac{1}{\sigma_{DIS}}\frac{d\sigma}{d\theta_{fwd}}$ [deg^{-1}]	δ_{stat}	δ_{sys}	*Hadronic energy scale*	*Track momenta*	*El. magn. energy scale*	*Correction uncertainty*
10 – 20	0.02	$\pm$ 39	$\pm$2	$\pm$1	$\pm$0	$\pm$2	$\pm$ 0
20 – 35	0.009	$\pm$ 41	$\pm$2	$\pm$1	$\pm$1	$\pm$1	$\pm$ 1
35 – 90	0.003	$\pm$ 39	$\pm$3	$\pm$1	$\pm$1	$\pm$3	$\pm$ 1
$\mathbf{x_p}$	$\frac{1}{\sigma_{DIS}}\frac{d\sigma}{dx_p}$	δ_{stat}	δ_{sys}	*Hadronic energy scale*	*Track momenta*	*El. magn. energy scale*	*Correction uncertainty*
0.6 – 0.8	0.2	$\pm$ 73	$\pm$5	$\pm$4	$\pm$0	$\pm$2	$\pm$ 1
0.8 – 0.9	0.6	$\pm$ 60	$\pm$2	$\pm$2	$\pm$1	$\pm$0	$\pm$ 0
0.9 – 1.0	3.7	$\pm$ 29	$\pm$2	$\pm$2	$\pm$0	$\pm$0	$\pm$ 1

Table A.10: *Normalized dijet cross sections for NC events selected with $Q^2 > 10\ 000$ GeV^2 and $0.03 < y < 0.85$. The jets are reconstructed with the modified Durham algorithm. The dijet events satisfy the cuts $y_2 > 0.001$ and $10° < \theta_{jet} < 140°$.*

Bibliography

[1] **H1 Collaboration, I. Abt et al.**
A Measurement of Multi-jet Rates in Deep-Inelastic-Scattering at HERA
Z. Phys. C61 (1994) 59

ZEUS Collaboration, M. Derrick et al.
Jet Production in High Q^2 Deep-Inelastic ep Scattering at HERA
Z. Phys. C67 (1995) 81

[2] **H1 Collaboration, C. Adloff et al.**
Measurement of Neutral and Charged Current Cross-Sections in Positron-Proton Collisions at Large Momentum Transfer
Eur. Phys. J. C13 (2000) 609

[3] **ZEUS Collaboration, J. Breitweg et al.**
Measurement of High Q^2 Neutral Current e+p Deep Inelastic Scattering Cross Sections at HERA
Eur. Phys. J. C11 (1999) 427

ZEUS Collaboration, J. Breitweg et al.
Measurement of High Q^2 Charged-Current e+p Deep Inelastic Scattering Cross Sections at HERA
Eur. Phys. J. C12 (2000) 411

[4] **H1 Collaboration, C. Adloff et al.**
Mesurement ans QCD Analysis of Jet Cross Sections in Deep-Inelastic Positron-Proton Collisions at $\sqrt{s}$ of 300 GeV
DESY 00-145, submitted to Eur. Phys. J. C

[5] **ZEUS Collaboration, J. Breitweg et al.**
Measurement of differential cross sections for dijet production in neutral current DIS at high Q^2 and determination of α_s
Contributed paper to ICHEP 2000, Osaka, Japan

[6] **ZEUS Collaboration, M. Derrick et al.**
Study of Charged-Current ep Interactions at $Q^2 > 200$ GeV^2
with the ZEUS Detector at HERA
Z. Phys. C72 (1996) 47

[7] **ZEUS Collaboration, J. Breitweg et al.**
Measurement of Jet Shapes in High Q^2 Deep Inelastic Scattering at HERA
Eur. Phys. J. C8 (1999) 367

[8] **M. Derrick et al.**
Hadron production mechanisms in anti-neutrino-proton
charged current interactions
Phys. Rev. D24 (1981) 1071, Erratum-ibid. D30 (1984) 1129

WA21 Collaboration, G.T. Jones et al.
W^2 and Q^2 dependence of charged hadron and pion multiplicities
in neutrino p and anti-neutrino p charged current interactions
Z. Phys. C46 (1990) 25

[9] **H1 Collaboration, C. Adloff et al.**
Dijet Production in Charged and Neutral Current
e^+p Interactions at High Q^2
DESY 00-143, submitted to Eur. Phys. J. C

[10] **H1 Collaboration, I. Abt et al.**
The H1 Detector at HERA
Nucl. Instr. and Meth. A386 (1997) 310

[11] **H1 Calorimeter Group, B. Andrieu et al.**
Results from Pion Calibration Runs for the H1 Liquid Argon Calorimeter
Nucl. Instr. and Meth. A336 (1993) 499

[12] **H1 Calorimeter Group, B. Andrieu et al.**
Beam Tests and Calibration of the H1 Liquid Argon Calorimeter with Electrons
Nucl. Instr. and Meth. A350 (1994) 57

[13] **Beate Heinemann**
Measurement of Charged Current and Neutral Current Cross Sections
in Positron Proton Collisions at $\sqrt{s} \approx 300$ GeV
Ph.D. Thesis, Hamburg (1999)

[14] **H1 Collaboratiom, S. Aid et al.**
A measurement and QCD analysis of the proton
structure function $F_2(x, Q^2)$ at HERA
Nucl. Phys. B470 (1996) 3

[15] **H1 Calorimeter Group, B. Andrieu et al.**
The H1 Liquid Argon Calorimeter System
Nucl. Instr. and Meth. A336 (1993) 460

[16] **H1 SpaCal Group, I. Abt et al.**
Nucl. Instr. and Meth. A374 (1996) 149

[17] **H1 SpaCal Group, I. Abt et al.**
Nucl. Instr. and Meth. A382 (1996) 395

[18] **C.G. Callan**
Broken scale invariance in scalar field theory
Phys. Rev. D2 (1970) 1541

[19] **R.K. Ellis, W.J. Stirling, B.R. Webber**
QCD and Collider Physics
Cambridge University Press (1996)

[20] **Particle Data Group, C. Caso et al.**
Review of Particle Physics
Eur. Phys. J. C3 (1998) 1

[21] **W.A. Bardeen, A.J. Buras, D.W. Duke, T. Muta**
Deep Inelastic Scattering beyond the Leading order
in Asymptotically Free Gauge Theories
Phys. Rev. D18 (1978) 3998

[22] **V.N. Gribov, L.N. Lipatov**
Deep-Inelastic ep-Scattering in Perturbation Theory
Sov. J. Nucl. Phys. 15 (1972) 438

G. Altarelli, G. Parisi
Asymptotic Freedom in Parton Language
Nucl. Phys. B126 (1977) 298

Yu.L. Dokshitzer
Calculations of the Structure Functions for Deep-Inelastic Scattering and
e^+e^- Annihilation by Perturbation Theory in QCD
Sov. Phys. JETP 46(1977) 641

[23] **E. Mirkes, D. Zeppenfeld**
Dijet Production at HERA in Next-to-Leading Order
Phys. Lett. B380 (1996) 205

[24] **A. Arbuzov et al.**
`HECTOR 1.00`: A program for the calculation of QED, QCD and
electroweak corrections to ep and $l^{\pm}N$ deep inelastic
neutral and charged current scattering
Comput. Phys. Commun. 94 (1996) 128

[25] **J. Blümlein et al.**
Proceedings of the Workshop "Physics at HERA"
Vol. 1, eds. W. Buchmüller, G. Ingelmann, DESY (1992) 67

[26] **J.G. Körner, E. Mirkes, G.A. Schuler**
QCD Jets at HERA
Int. J. Mod. Phys. A4 (1989) 1781

[27] **T. Kinoshita**
Mass Singularities of Feynman Amplitudes
J. Math. Phys. 3 (1962) 650

T.D. Lee, M. Nauenberg
Degenerate Systems and Mass Singularities
Phys. Rev. B113 (1964) 1549

[28] **R.K. Ellis, D.A. Ross, A.E. Terrano**
The Perturbative Calculation of Jet Structure in e^+e^- Annihilation
Nucl. Phys. B178 (1981) 421

[29] **K. Fabricius, I. Schmitt, G. Kramer, G. Schierholz**
Higher Order Perturbative QCD Calculation of Jet Cross-Sections in e^+e^- Annihilation
Z. Phys. C11 (1981) 315

[30] **L. Lønnblad**
ARIADNE: A Program for Simulation of QCD Cascades Implementing the Color Dipole Model
Comp. Phys. Comm. 71 (1992) 15

[31] **G. Ingelmann, A. Edin, J. Rathsmann**
LEPTO 6.5: a Monte Carlo Generator for Deep Inelastic Lepton-Nucleon Scattering
Comp. Phys. Comm. 101 (1997) 108

[32] **H. Jung**
Hard Diffractive Scattering in High-Energy *ep* Collisions and the Monte Carlo Generation RAPGAP
Comp. Phys. Comm. 86 (1995) 147

[33] **G. Marchesini et al.**
HERWIG: a Monte Carlo Event Generator
Comp. Phys. Comm. 67 (1992) 15

[34] **N.H. Brook et al.**
Proc. of the Workshop "Monte Carlo Generators for HERA"
Eds. A.T. Doyle, G. Grindhammer, G. Inglemann, H. Jung, hep-ex/9912053

[35] **CTEQ Collaboration, H.L. Lai et al.**
Improved Parton Distributions from Global Analysis of Recent Deep Inelastic Scattering and Inclusive Data
Phys. Rev. D55 (1997) 1280

[36] **G. Gustafson, U. Petterson**
Dipole formulation of QCD cascades
Nucl. Phys. B306 (1988) 746

B. Andersson, G. Gustafson, L. Lønnblad, U. Petterson
Coherence effects in deep inelastic scattering
Z. Phys. C43 (1989) 625

[37] **M. Bengtsson, T. Sjøstrand**
The Lund Monte Carlo for Jet Fragmentation and E^+e^- Physics
Comp. Phys. Comm. 43 (1986) 347

[38] **M. Bengtsson, T. Sjøstrand**
Parton showers in leptoproduction events
Z. Phys. C37 (1988) 465

[39] **B.R. Webber**
A QCD Model for Jet Fragmentation Including Soft Gluon Interference
Nucl. Phys. B238 (1984) 492

[40] **D. Amati, G. Veneziano**
Preconfinement as a property of perturbative QCD
Phys. Lett. B83 (1979) 87

[41] **G.A. Schuler, H. Spiesberger**
Proc. of the Workshop "Physics at HERA"
Eds. W. Buchmüller, G. Ingelmann, Vol. 3 (1991) 1419

[42] **A. Kwiatkowski, H. Spiesberger, H.J. Mohring**
HERACLES: an Event Generator for ep Interactions at HERA Energies Including Radiative processes: Version 1.0.
Comp. Phys. Comm. 69 (1992) 155

[43] **S. Catani, M.H. Seymour**
A General Algorithm for Calculating Jet Cross-Sections in NLO QCD
Nucl. Phys. B485 (1997) 291

[44] **B. Pötter**
JETVIP 1.1: Calculating one Jet and Two Jet Cross-Sections with virtual photons in NLO QCD
Comp. Phys. Comm. 119 (1999) 45

[45] **D. Graudenz**
DISASTER++, version 1.0.1
hep-ph/9710244

[46] **C. Duprel et al.**
Proc. of the Workshop "Monte Carlo Generators for HERA"
Eds. A.T. Doyle, G. Grindhammer, G. Inglemann, H. Jung, hep-ex/9912053

[47] **V. Antonelli, M. Dasgupta, G. Salam**
Resummation of Thrust Distributions in DIS
J. High Energy Phys. 02 (2000) 001

[48] **H1 Collaboration, C. Adloff et al.**
Observation of Events with an Isolated High Energy Lepton and Missing Transverse Momentum at HERA
Eur. Phys. J. C5 (1998) 575

[49] **H1 Collaboration, S. Aid et al.**
Measurement of the Q^2 dependence of the Charged and Neutral Current Cross Sections in ep Scattering at HERA
Phys. Lett. B379 (1996) 319

[50] **A. Blondel, F. Jacquet**
Proceedings "Study of an ep Facility for Europe", DESY 79-48 (1979) 391

[51] **H1 Collaboration, C. Adloff et al.**
Diffractive Dissociation in Photoproduction at HERA
Z. Phys. C74 (1997) 221

[52] **T. Sjøstrand**
High-Energy Physics Event Generation with PYTHIA 5.7 and JETSET 7.4
Comput. Phys. Commun 82 (1994) 74

[53] **E. Chabert et al.**
H1 internal report, H1-11/98-556 (1998)

[54] **A. Schöning**
Untersuchung von Prozessen mit virtuellen und reellen $W^{\pm}$-Bosonen am H1-Detektor bei HERA
Ph.D. Thesis, Hamburg (1996)

[55] **P. Bruel**
Ph.D. Thesis, Orsay (1998)

[56] **S. Catani et al.**
New Clustering Algorithm for Multi-jet Cross-Sections in e^+e^- Annihilation
Phys. Lett. B269 (1991) 432

[57] **H1 Collaboration, C. Adloff et al.**
Differential (2+1) Jet Event Rates and Determination of α_s
in Deep Inelastic Scattering
Eur. Phys. J. C5 (1998) 625

[58] **JADE Collaboration, W. Bartel et al.**
Experimental Studies on Multi-Jet Production in
e^+e^--Annihilation at PETRA energies
Z. Phys. C33 (1986) 23

[59] **V. Blobel**
Unfolding Methods in High Energy Physics Experiments
CERN 85-02 (1985)

[60] **N. Tobien**
Messung differentieller 2-Jet-Raten und Bestimmung der starken
Kopplung α_s in tiefunelastischer Streuung bei HERA
Ph.D. Thesis, Hamburg (1999)

[61] **Yu.L. Dokshitzer, B.R. Webber**
Calculation of Power Corrections to Hadronic Event Shapes
Phys. Lett. B352 (1995) 451

[62] **H1 Collaboration, C. Adloff et al.**
Measurement of $D^\star$ Meson Cross Sections at HERA and
Determination of the Gluon Density in the Proton
Nucl. Phys. B545 (1999) 21

[63] **CTEQ Collaboration, H.L. Lai et al.**
Global QCD Analysis of Parton Structure of the Nucleon:
CTEQ5 Parton Distributions
Eur.Phys.J. C12 (2000) 375

[64] **A.D. Martin, R.G. Roberts, W.J. Stirling, R.S. Thorne**
Parton Distributions: A New Global Analysis
Eur. Phys. J. C4 (1998) 463

[65] **A.D. Martin, R.G. Roberts, W.J. Stirling**
The α_s dependence of Parton Distributions
Phys. Lett. B356 (1995) 89

[66] **H1 Collaboration, C. Adloff et al.**
Observation of Events at Very High Q^2 in ep Collisions at HERA
Z. Phys. C74 (1997) 191